Study on acceleration of the method of moments for electromagnetic wave scattering problems with the characteristic basis function method and Calderón preconditioning

Tai Tanaka

Acknowledgement

I would like to express my sincere gratitude to my supervisor, Professor Naoshi Nishimura and Professor Kazuki Niino at Graduate School of Informatics, Kyoto University. They gave me a lot of invaluable advice. Without their guidance and encouragement, I would not have been able to complete my research.

I also wish to express my gratitude to Professor Yuusuke Iso, Professor Hitoshi Yoshikawa, and Professor Hiroshi Fujiwara for reviewing my doctoral dissertation. In particular, I would like to express my gratitude Professor Iso for being my supervisor in the examination of this dissertation.

I would also like to thank the members of Computational Mechanics Laboratory at Graduate School of Informatics, Kyoto University. They always gave me various inspirations.

My sincere appreciation also goes to all my colleagues in Antennas Technology Department of Information Technology R&D Center and Space Business Development Department at Mitsubishi Electric Corporation. Dr. Hiroaki Miyashita, Dr. Naofumi Yoneda, Dr. Yoshio Inasawa, Dr. Yasuhiro Nishioka, Dr. Michio Takikawa at Mitsubishi Electric Corporation, and Professor Yoshihiko Konishi at Hiroshima Institute of Technology gave me the opportunity to conduct research on the electromagnetic field. Mr. Toshihisa Matsue, Mr. Shigeru Uchida, Mr. Nobuyoshi Horie, Mr. Kazutaka Kumeno, and Mr. Masato Mizutani encouraged me to challenge the doctoral program while working. It was also thanks to Dr. Toru Takahashi that I decided to pursue a second doctorate.

Finally, I would like to thank my family and friends for their support and encouragement.

February 2023
Tai Tanaka

Contents

List of Figures

List of Tables

Acronyms

BC Buffa-Christiansen

CBF Characteristic Basis Function

CBFM Characteristic Basis Function Method

CFIE Combined Field Integral Equation

CMP Calderón Multiplicative Preconditioner

EFIE Electric Field Integral Equation

FMM Fast Multipole Method

GMRES Generalized Minimal RESidual

IPCBF Improved Primary CBF

KCP Krylov-Calderón Preconditioning

MFIE Magnetic Field Integral Equation

MoM Method of Moments

PMCHWT Poggio-Miller-Chang-Harrington-Wu-Tsai

RCS Radar Cross Section

RMSE Root Mean Square Error

RWG Rao-Wilton-Glisson

SVD Singular Value Decomposition

Chapter 1

Introduction

1.1 Background

The aim of this dissertation is to construct a fast and accurate method for obtaining the spatial characteristics of electromagnetic scattering fields. The objects for obtaining the scattering fields are the scatterers with sizes ranging from 0.5 to 50 wavelengths in the radio to optical bands.

Suitable electromagnetic field solvers differ depending on the assumed application and its frequency band. From the radio frequency to the optical bands used in communication and radar systems, numerical methods such as the method of moments (MoM) [1], the finite element method [2], and the finite-difference time-domain method [3] are often used as solvers. One of them, the MoM is commonly referred to as the boundary element method in fields other than electromagnetic field analysis. In the MoM one utilizes the Galerkin method [1] to discretize integral equations into a system of linear equations, which is solved with direct or iterative algorithms [4]. The computational cost of the MoM is in general governed by that of computing the impedance matrix in the discretized system, which is usually quite expensive since the impedance matrix is dense. For scatterers of the size mentioned above, the number of unknowns could be up to nearly one million. One of solutions to this problem is the use of fast methods such as fast multipole method (FMM), which accelerate the calculation of products of the impedance matrix with given vectors [5–7]. Hence iterative algorithms accelerated with the FMM are widely used for analyzing large-scale problems. This dissertation focuses on such iterative algorithms, although fast methods for direct solvers such as those based on the $\mathcal{H}$-matrix have been developed recently [8–10].

Analyses using iterative methods often suffer from poor convergence, which is usually solved by preconditioners. In recent years, the Calderón multiplicative pre-

conditioner (CMP) has been proposed in order to improve the convergence of the electric field integral equation (EFIE) [11]. This preconditioner is based on simple mathematical relations between products of integral operators. However, discretizing products of integral operators in Maxwell's equations is more complicated than is expected from the apparent mathematical simplicity. In the case of the electric field integral equation, for example, two types of mutually (almost) orthogonal basis functions for the same functional space are necessary for discretizing operators corresponding to the preconditioner and the impedance matrix. Indeed, it is known that a naive choice of standard basis functions such as the Rao-Wilton-Glisson (RWG) basis function [12] as shown in Fig. 1.1, denoted by $\boldsymbol{f}$, for discretizing both the impedance and preconditioning matrices does not work since the Gram matrix associated with this choice is singular, while its inverse appears in the formulation of the CMP. Using RWG for the impedance matrix and its 90 degree rotation, i.e. $\hat{\boldsymbol{n}} \times \boldsymbol{f}$, for the preconditioner does not make sense since $\hat{\boldsymbol{n}} \times \boldsymbol{f}$ does not belong to H_{div} where $\hat{\boldsymbol{n}}$ is the unit normal vector on the boundary. As a matter of fact, a widely used choice of basis functions for the CMP is the RWG basis function for the impedance matrix and the Buffa-Christiansen (BC) basis function [13] for the preconditioner. However the computational time of the preconditioner discretized with the BC function is much more than that of the impedance matrix with the RWG function since the BC function is defined on the barycentric refinement of the original mesh on which the RWG function is defined as shown in Fig. 1.2. The CMP has also been applied to integral equations for scattering problems with dielectrics such as the Poggio-Miller-Chang-Harrington-Wu-Tsai (PMCHWT) formulation [14, 15]. For the PMCHWT, another formulation of the Calderón preconditioner has been proposed [16–18], in which the surface electric and magnetic currents are expanded with the RWG and BC basis functions shown in Fig. 1.3, respectively. This formulation has a beautiful symmetry and is able to accelerate the convergence in problems for scatterers having smooth boundaries. Particularly noteworthy is the Calderón preconditioning proposed in [16] and [17] which utilizes the Calderón formulae and the Krylov subspace method. We call this approach the Krylov-Calderón preconditioning (KCP) in this dissertation in order to distinguish it from the standard CMP. As a preconditioner, KCP is equally (and often more) effective compared to the standard CMP while its implementation is simpler than that of CMP (See [16, 17] and 3.2.3). However, for a scatterer formed by multiple faces, the accuracy of the surface current spanned with the BC basis function is usually worse than that with the RWG function near sharp edges or corners [16]. This occurs even if the scatterer has a simple shape such as a cube.

As another class of numerical methods to speed up MoM apart from the preconditioned fast methods, one may mention domain decomposition methods [9, 19],

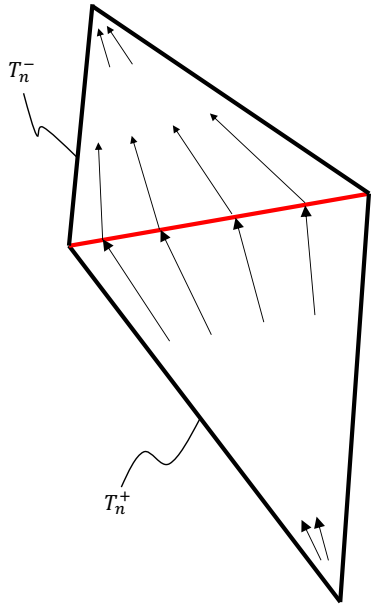

Figure 1.1: RWG basis function

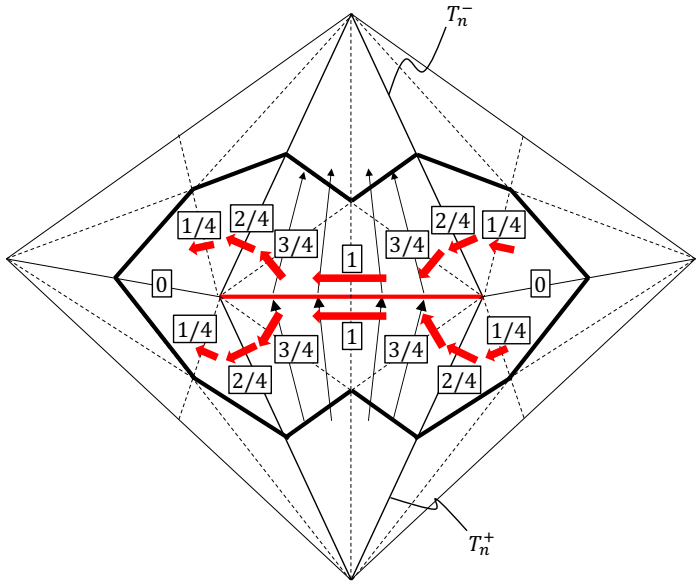

Figure 1.2: BC basis function by using barycentric refinement. The BC basis for the original mesh is constructed by a linear combination of the RWG function and its coefficients defined on the edges of the barycentric refinement mesh. The values enclosed in squares are the coefficients for each edge.

among which we are particularly interested in the characteristic basis function method (CBFM) [20–24]. The CBFM is known to be particularly suited for scattering problems by finite periodic scatterers such as radiation by array antennas,

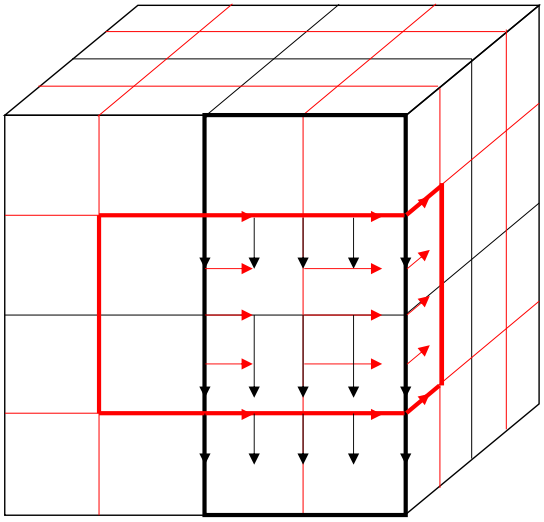

Figure 1.3: Dual basis function. The electric and magnetic currents are expanded by the bases that define their supports on the black and red line boxes, respectively. These bases have duality.

and is also known to be quite effective in calculating monostatic radar cross sections (RCS). In CBFM one typically decomposes domains into several pieces called cells (see [25, 26] for optimizing cell divisions), and solves problems (which may be called generating problems) in each cell with certain numbers of incident fields. After obtaining as many solutions as the number of the incident fields in each cell, one generates linearly independent basis functions from these solutions by applying a matrix orthogonalization method such as the Gram-Schmidt orthogonalization or the singular value decomposition (SVD) [27] to a matrix in which these solutions are arranged as column vectors. The basis functions obtained in this way are called the characteristic basis functions (CBFs) and the CBFM solves the original problem by using CBFs as the basis functions. The computational time of the CBFM is less than that of the ordinary MoM since the number of CBFs is much less than that of the standard basis functions. The accuracy of the CBFM depends significantly on the choice of CBFs, which is why various methods for generating CBFs have been proposed. For example, CBFs suitable for scattering and radiation problems have been proposed in [21] and in [28–31], respectively. The so-called CBFM-enhanced iterative methods use CBFs updated by considering iteration history [32]. The CBFM analysis is applicable not only to metals, but also to dielectrics as discussed in [29], [33–35]. We also have proposed a class of CBFs, called improved primary CBFs (IPCBFs), which are expected to approximate surface currents efficiently [36–38] with fewer unknowns than standard CBFM. The IPCBFs take into account the influence of higher-order CBFs to primary CBFs iteratively. The accu-

racy of IPCBFs can be controlled as one sets the residual norm of the iterative CBF generations appropriately.

In CBFM one often uses direct methods for solving linear systems since the CBFM considerably reduces the number of unknowns [22]. This is particularly true in multilevel versions of CBFM [39–41]. In larger problems, however, the number of unknowns is not always sufficiently small for using direct solvers. Indeed, CBFM based on iterative solvers [32, 42, 43] have been proposed. Use of iterative solvers is considered particularly important in large-scale dielectric problems because of the increased number of unknowns. Also the convergence of iterative algorithms in the CBFM can be as poor as that in the standard MoM since they are based on the same ill-conditioned integral equations such as the PMCHWT equation. It is therefore very important to reduce the number of iterations in the iterative CBFMs for dielectric problem.

1.2 Scope of dissertation

This dissertation presents novel two types of the CBFMs, one that produces the accurate results with a small number of unknowns, and the other that improves the convergence of iterative methods, respectively. Both methods combine the iterative method and the CBFM, and compensate for each other's disadvantages as shown in the previous section to accelerate the analysis while maintaining accuracy. Each method is presented in the next two chapters, as follows.

Chapter 2 shows the CBFM with the use of the IPCBFs based on Krylov subspace algorithm to calculate angular characteristics of the scattering for electromagnetic incident waves from multiple directions rapidly. In practical analysis, the scattering field is often calculated for multiple incident waves in a specific coordinate plane to obtain the scatterer's electromagnetic properties (Fig. 1.4). The methods described in the chapter 2 can efficiently obtain such properties. It can reduce the number of unknowns and makes the accuracy of the CBFM easy to control by residual norm of the iteration and number of sampling points of the incident plane waves in the computation of generating the CBFs. We also show the hybrid algorithm of the MoM and the CBFM with IPCBF as a further accuracy control. The algorithm uses the MoM to improve the accuracy based on the CBFM analysis results. We analyzed the RCS pattern of the two scatterers by using the proposed methods. The results indicate that the accuracy of the analysis can be controlled by the norm of IPCBF if the appropriate angular resolution is set. And the proposed CBFM is more than five times faster than the conventional method. The accuracy improvement can be achieved by the hybrid algorithm, which is still faster than the conventional MoM. The research in this chapter is based on [44].

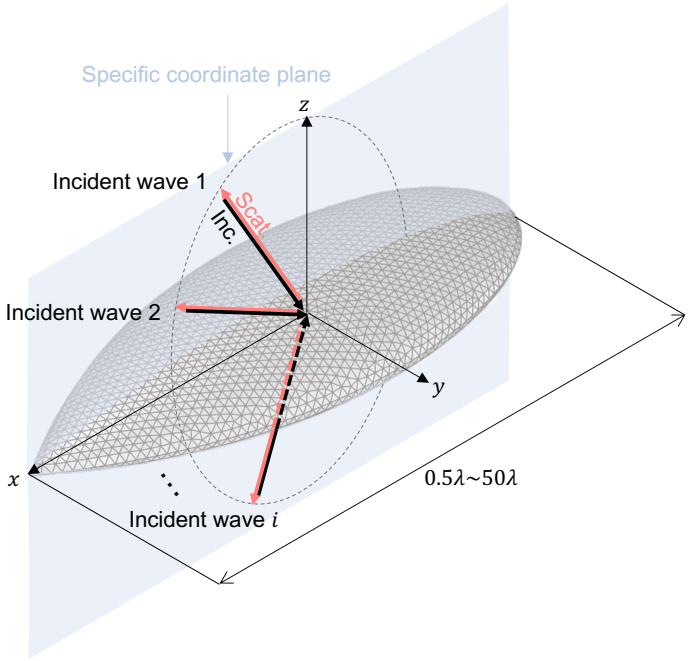

Figure 1.4: Scattering field in a specific coordinate plane

Chapter 3 shows the CBFM for analyzing the scattering by dielectric objects based on the Poggio-Miller-Chang-Harrington-Wu-Tsai formulation. In the proposed method, the bases for electric and magnetic currents are orthogonalized with the help of the singular value decomposition, and are used as dual basis functions in a way similar to the RWG and BC basis functions. We show that the use of the Calderón precondtioner based on the Krylov subspace method together with the proposed method can prevent from the poor convergence of the solution of the matrix equation in problems involving dielectrics. We considered different shapes of dielectric scatterers for the purpose of validation. The numerical results agreed well with those obtained by the conventional method of moments and the proposed method was faster than the conventional method. These results indicate that the proposed method is effective for scattering analysis of the dielectrics. We mainly discuss cases of disconnected scatterers in the chapter 3, but outline some preliminary studies on the use of the proposed CBFM together with IPCBFs in connected scatterer cases in the appendix A. The research in this chapter is based on [45].

Finally, chapter 4 gives concluding remarks and observations of the dissertation.

1.3 Definition of symbols

In this dissertation, we define following symbols. The bold and italicized symbols such as $\boldsymbol{A}$ represent vector quantities in three-dimensional fields. The uppercase and lowercase symbols $\mathbf{A}$, $\mathbf{a}$ written in bold and upright type represent matrices and vectors, respectively. The expression such as $\Big[\mathbf{A}\Big]_{ij}$ denotes an entry of a matrix and an element of a vector. A matrix or vector with a subscript such as $\mathbf{A}_{ij}$, $(\mathbf{A})_{ij}$ is a subset or a subvector, respectively. The matrix with the superscript H represents the adjoint matrix. Similarly, the matrix with the superscript T represents the transpose matrix. $\langle \mathbf{A}, \mathbf{B} \rangle$ is the inner product of $\mathbf{A}^H$ and $\mathbf{B}$. In addition, radar cross section (RCS) is often used to evaluate calculation methods in this dissertation. RCS pattern indicates monostatic radar cross section (RCS) pattern according to the definition in [46].

Chapter 2

Accuracy controllable characteristic basis function method by using Krylov subspace algorithm

2.1 Introduction

In this chapter, we propose a hybrid algorithm of the MoM and CBFM with the IPCBFs, which can rapidly and accurately calculate angular characteristics of scattered waves for electromagnetic incident waves from multiple directions. The proposed method roughly captures characteristics of a solution by CBFM, and the accuracy of the solution is further controlled with the help of the Krylov subspace method in the MoM. Also the number of sampling points of the incident plane waves in the computation of generating the CBFs is small. The proposed method is particularly suitable for analyzing the scattering characteristics of incident waves propagating in a specific coordinate plane. We analyzed the monostatic radar cross section pattern of two scatterers by using the proposed method. The accuracy improvement can be achieved by the hybrid algorithm, which is faster than the conventional MoM.

2.2 Integral equations and MoM

In this section, we present a preliminary description of the MoM. We assume that domain Ω is a perfect electric conductor, and $D = \mathbb{R}^3 \setminus \bar{\Omega}$ is the analysis space as

shown in Fig. 2.1. $\Gamma = \partial\Omega$ is the closed surface of the PEC. The unit normal vector $\hat{\boldsymbol{n}}$ points in the direction of D. The electric field $\boldsymbol{E}(\boldsymbol{r})$ and the magnetic field $\boldsymbol{H}(\boldsymbol{r})$ at the frequency ω satisfy the Maxwell's equations [47] as follows:

$$\nabla \times \boldsymbol{E}(\boldsymbol{r}) = -j\omega\mu\boldsymbol{H}(\boldsymbol{r}),$$
$$\nabla \times \boldsymbol{H}(\boldsymbol{r}) = j\omega\epsilon\boldsymbol{E}(\boldsymbol{r}),$$

where ϵ and μ are the permittivity and permeability, and j is imaginary unit, respectively. On the boundary Γ, $\boldsymbol{E}_1(\boldsymbol{r})$ and $\boldsymbol{H}_1(\boldsymbol{r})$, the limit values of $\boldsymbol{E}(\boldsymbol{r})$ and $\boldsymbol{H}(\boldsymbol{r})$ from D to Γ, satisfy the following boundary conditions:

$$\boldsymbol{E}_1(\boldsymbol{r}) \times \hat{\boldsymbol{n}} = 0,$$
$$\boldsymbol{J}(\boldsymbol{r}) \equiv \hat{\boldsymbol{n}} \times \boldsymbol{H}_1(\boldsymbol{r}),$$

where $\boldsymbol{J}(\boldsymbol{r})$ is the unknown surface current on the boundary Γ. We consider the electromagnetic wave scattering problem of finding $\boldsymbol{E}(\boldsymbol{r})$ and $\boldsymbol{H}(\boldsymbol{r})$ for which the scattered field $(\boldsymbol{E}^{\mathrm{scat}}, \boldsymbol{H}^{\mathrm{scat}}) = (\boldsymbol{E} - \boldsymbol{E}^{\mathrm{inc}}, \boldsymbol{H} - \boldsymbol{H}^{\mathrm{inc}})$ satisfy the radiation condition at $\boldsymbol{r} \to \infty$. $\boldsymbol{E}^{\mathrm{inc}}(\boldsymbol{r})$ and $\boldsymbol{H}^{\mathrm{inc}}(\boldsymbol{r})$ are the electric and magnetic incident fields, respectively. The electric field integral equation (EFIE) and magnetic field integral equation (MFIE) [48] for this problem are represented by

$$\hat{\boldsymbol{n}} \times \hat{\boldsymbol{n}} \times \boldsymbol{E}^{\mathrm{inc}}(\boldsymbol{r}) = -\eta\hat{\boldsymbol{n}} \times (\mathcal{T}\boldsymbol{J})(\boldsymbol{r}), \tag{2.1}$$

$$\hat{\boldsymbol{n}} \times \boldsymbol{H}^{\mathrm{inc}}(\boldsymbol{r}) = -(\mathcal{K}\boldsymbol{J})(\boldsymbol{r}) + \frac{1}{2}\boldsymbol{J}(\boldsymbol{r}). \tag{2.2}$$

The integral operators $\mathcal{T}$ and $\mathcal{K}$ are defined as

$$(\mathcal{T}\boldsymbol{J})(\boldsymbol{r}) = jk\hat{\boldsymbol{n}} \times F.P. \int_\Gamma \left(\mathcal{I} + \frac{1}{k^2}\nabla\nabla\right) G(\boldsymbol{r}, \boldsymbol{r}')\boldsymbol{J}(\boldsymbol{r}')d\boldsymbol{r}' \equiv \hat{\boldsymbol{n}} \times (\mathcal{T}'\boldsymbol{J})(\boldsymbol{r}) \tag{2.3}$$

$$(\mathcal{K}\boldsymbol{J})(\boldsymbol{r}) = \hat{\boldsymbol{n}} \times P.V. \int_\Gamma \boldsymbol{J}(\boldsymbol{r}') \times \nabla G(\boldsymbol{r}, \boldsymbol{r}')d\boldsymbol{r}' \tag{2.4}$$

Here, *F.P.*, *P.V.*, and $\mathcal{I}$ represent the finite part, the Cauchy principal value integral, and the identity operator, respectively. The wavenumber and the impedance of the free space are denoted by k and η, respectively. The function $G(\boldsymbol{r}, \boldsymbol{r}')$ is the fundamental solution of Helmholtz' equation in three-dimension space for the observation point $\boldsymbol{r}$ and the source point $\boldsymbol{r}'$:

$$G(\boldsymbol{r}, \boldsymbol{r}') = \frac{e^{-jk|\boldsymbol{r}-\boldsymbol{r}'|}}{4\pi|\boldsymbol{r} - \boldsymbol{r}'|} \tag{2.5}$$

We have the combined field integral equation (CFIE) in the following form:

$$\begin{aligned} &-\gamma\hat{\boldsymbol{n}} \times \hat{\boldsymbol{n}} \times \boldsymbol{E}^{\mathrm{inc}}(\boldsymbol{r}) + (1-\gamma)\eta\hat{\boldsymbol{n}} \times \boldsymbol{H}^{\mathrm{inc}}(\boldsymbol{r}) \\ &\quad = \gamma\eta\hat{\boldsymbol{n}} \times (\mathcal{T}\boldsymbol{J})(\boldsymbol{r}) - (1-\gamma)\eta(\mathcal{K}\boldsymbol{J})(\boldsymbol{r}) + \frac{1}{2}(1-\gamma)\eta\boldsymbol{J}(\boldsymbol{r}), \end{aligned} \tag{2.6}$$

where γ is coefficients of the combination of (2.1) and (2.2). We use the CFIE for analyzing the problem in this chapter.

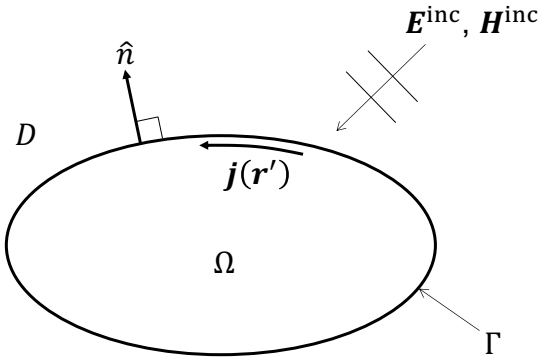

Figure 2.1: Definition of the domain

2.2.1 Discretization of integral equations

In this analysis, the scatterers are discretized with triangles and RWG basis function [12] $\boldsymbol{f}_n(\boldsymbol{r})$ defined on the triangular mesh. The unknown current $\boldsymbol{J}(\boldsymbol{r})$ is expanded with the RWG basis function:

$$\boldsymbol{J}(\boldsymbol{r}) \approx \sum_{n=1}^{N} \alpha_n \boldsymbol{f}_n(\boldsymbol{r}), \quad \alpha_n \in \mathbb{C}, \tag{2.7}$$

$$\boldsymbol{f}_n(\boldsymbol{r}) = \begin{cases} \frac{l_n}{2S_n^+}\left(\boldsymbol{r} - \boldsymbol{v}_n^+\right), & \boldsymbol{r} \text{ in } T_n^+ \\ -\frac{l_n}{2S_n^-}\left(\boldsymbol{r} - \boldsymbol{v}_n^-\right), & \boldsymbol{r} \text{ in } T_n^- \\ 0, & \text{otherwise} \end{cases},$$

where $\boldsymbol{v}_n^{\pm}$, l_n, and $S_n^{\pm}$ are the vertexes that do not form the edge n of shared by the two triangles $T_n^{\pm}$, length of the edge n, and the area of the two triangles $T_n^{\pm}$, respectively (Fig. 2.2). Taking the inner product of RWG basis and the integral equation in (2.6), we obtain the matrix equation [1]

$$\mathbf{Zj} = \mathbf{v} \tag{2.8}$$

where $\mathbf{Z} \in \mathbb{C}^{N\times N}$ and $\mathbf{v} \in \mathbb{C}^N$ are respectively the impedance matrix and incident field vector, which are defined by

$$\left[\mathbf{Z}\right]_{mn} = \int_\Gamma \boldsymbol{f}_m(\boldsymbol{r}) \cdot \left(\gamma\eta\hat{\boldsymbol{n}} \times \left(\mathcal{T}\boldsymbol{f}_n\right)(\boldsymbol{r}) - (1-\gamma)\eta\left(\mathcal{K}\boldsymbol{f}_n\right)(\boldsymbol{r}) + \frac{1}{2}(1-\gamma)\eta\boldsymbol{f}_n(\boldsymbol{r})\right)d\boldsymbol{r}, \tag{2.9}$$

$$\left[\mathbf{v}\right]_m = \int_\Gamma \boldsymbol{f}_m(\boldsymbol{r}) \cdot \left(-\gamma\hat{n} \times \hat{n} \times \boldsymbol{E}^{\text{inc}}(\boldsymbol{r}) + (1-\gamma)\eta\hat{n} \times \boldsymbol{H}^{\text{inc}}(\boldsymbol{r})\right)d\boldsymbol{r}. \tag{2.10}$$

In the conventional MoM, we solve equation (2.8) with an iterative method or a direct method to obtain the solution as the expansion coefficient vector $\mathbf{j} = \begin{bmatrix}\alpha_1 & \alpha_2 & \cdots & \alpha_N\end{bmatrix}^T$.

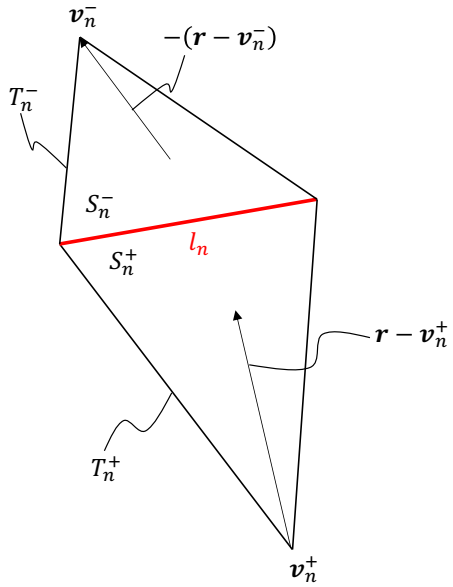

Figure 2.2: RWG basis function

The convergence of (2.8) is usually good because the discretized MFIE included in the CFIE has a small condition number. Since the condition number of the EFIE is large, the convergence of (2.8) becomes worse as the coefficient γ of the CFIE is set to larger values. On the other hand, the accuracy of the analysis improves [6].

2.3 Formulation of proposed method

2.3.1 Overview of CBFM

The CBFM is a numerical method to accelerate the MoM by discretizing integral equations with the CBF, which in general has smaller degree of freedoms than the RWG functions. For generating the CBF, the boundary of a scatterer is divided into N^{Cell} cells. The nth CBF in cell m, denoted by $\mathbf{c}_{mn}$, is represented as the linear combination of the RWG function:

$$\mathbf{c}_{mn}(\boldsymbol{r}) = \sum_{i=1}^{N_m} c_{mni} \boldsymbol{f}_{\Lambda_{mi}}(\boldsymbol{r}) \quad (n = 1, \cdots L_m), \tag{2.11}$$

where N_m and Λ_{mi} are the total number and index of the RWG function in cell m, and c_{mni} are complex coefficients. The complex matrix $\mathbf{C}_m \in \mathbb{C}^{N_m \times N_m^{\mathrm{CBF}}}$ consisting of the coefficients c_{mni}:

$$\left[\mathbf{C}_m\right]_{in} = c_{mni}. \tag{2.12}$$

is also referred to as the CBF in cell m in this chapter.

One of widely used methods to generate the CBF is as follows. Considering scattering problems whose scatterer is a part of the original one included in cell m, one computes the solution of the problem with multiple incident plane waves from s directions as wave sources. We define the solution in cell m with the ith incident wave as $\mathbf{j}_{m,i}$ and $\mathbf{J}_m$ by

$$\mathbf{J}_m = \begin{bmatrix} \mathbf{j}_{m,1} & \mathbf{j}_{m,2} & \cdots & \mathbf{j}_{m,s} \end{bmatrix}. \tag{2.13}$$

Once the coefficient matrix $\mathbf{J}_m$ is calculated, the conventional CBFM computes the CBF $\mathbf{C}_m$ by algebraically orthogonalizing $\mathbf{J}_m$ with the SVD:

$$\begin{aligned} \mathbf{J}_m &= \mathbf{U}\mathbf{\Sigma}\mathbf{V}^H \\ &= \begin{bmatrix} \mathbf{U}_\mathrm{L} & \mathbf{U}_\mathrm{S} \end{bmatrix} \begin{bmatrix} \mathbf{\Sigma}_\mathrm{L} & \\ & \mathbf{\Sigma}_\mathrm{S} \end{bmatrix} \begin{bmatrix} \mathbf{V}_\mathrm{L}^H \\ \mathbf{V}_\mathrm{S}^H \end{bmatrix} \\ &\simeq \mathbf{U}_\mathrm{L}\mathbf{\Sigma}_\mathrm{L}\mathbf{V}_\mathrm{L}^H, \end{aligned} \tag{2.14}$$

where $\mathbf{U} \in \mathbb{C}^{N_m \times r}$ and $\mathbf{V} \in \mathbb{C}^{s \times r}$ are unitary matrices and $\mathbf{\Sigma} \in \mathbb{C}^{r \times r}$ is the diagonal matrix having r singular values in its diagonal components. Here, Σ is split into two matrices Σ_L and Σ_S with the use of a threshold δ_{SVD}, namely Σ_L is the diagonal matrix with the singular values of $\mathbf{J}_m$ larger than $\sigma_1\delta_{\mathrm{SVD}}$ while Σ_S is the one with smaller singular values, where σ_1 is the largest singular value of $\mathbf{J}_m$. The submatrix of $\mathbf{U}$ corresponding to $\mathbf{\Sigma}_\mathrm{L}$, denoted by $\mathbf{U}_\mathrm{L} \in \mathbb{C}^{N_m \times N_m^{\mathrm{CBF}}}$, is used as the CBF $\mathbf{C}_m$. The CBF $\mathbf{C}_m$ obviously satisfies $\mathbf{C}_m^H\mathbf{C}_m = I$, which means that the coefficient vectors of the CBFs in each cell are algebraically orthogonalized.

2.3.2 Proposed algorithm

The CBFs are created from the excitation current of each cell. One of the simplest methods to generate CBF is to compute $\mathbf{j}_{m,i}$ as solutions of scattering problems in cell m without taking into account the mutual couplings between cells, namely

$$\mathbf{j}_{m,i} = \mathbf{Z}_{mm}^{-1} \left(\mathbf{v}_i\right)_m, \tag{2.15}$$

where $\mathbf{Z}_{mm} \in \mathbb{C}^{N_m \times N_m}$ is submatrix of the impedance matrix $\mathbf{Z}$ formed by N_m RWG functions in cell m and $\left(\mathbf{v}_i\right)_m \in \mathbb{C}^{N_m}$ is the subvector of the ith incident field vector $\mathbf{v}_i$ for cell m [20]. For $\mathbf{v}_i$, the plane waves propagating in the directions sampled at an appropriate interval from the three-dimensional unit sphere are used (Fig. 2.3). The CBF generated from $\mathbf{j}_{m,i}$ in (3.24) is called the primary CBF [21] as shown in Fig. 2.4.

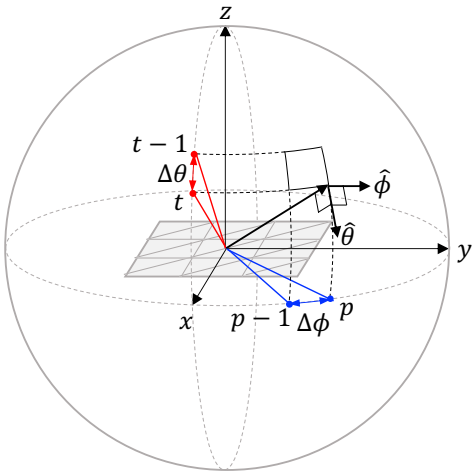

Figure 2.3: The propagating direction of the plane waves

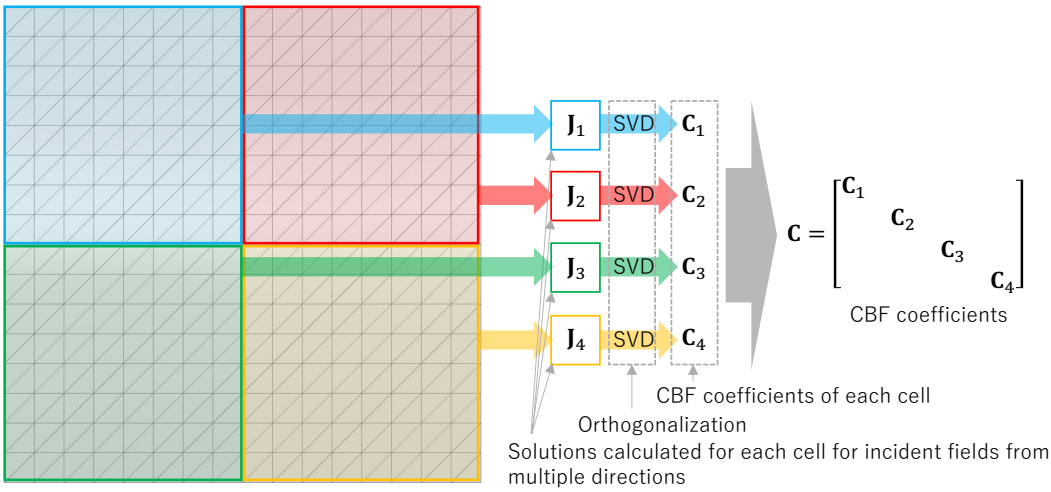

Figure 2.4: Diagram of the primary CBF generation when the flat plate is divided into four cells

In addition to the primary CBFs, several types of CBFs exist, such as secondary CBFs generated from the current of other cells [20] and higher-order CBFs [30]. In Tanaka et al. [36,37], we have proposed IPCBFs, which iteratively include the effect of the higher-order CBFs into the primary CBF without increasing the number of basis functions. The expansion coefficient vector $\mathbf{j}_{m,i}^{(p)}$ with p iterations for the IPCBF is obtained by

$$\mathbf{j}_{m,i}^{(p)} = \mathbf{Z}_{mm}^{-1} \left((\mathbf{v}_i)_m - \sum_{\substack{n=1 \\ n \neq m}}^{N^{\mathrm{Cell}}} \mathbf{Z}_{mn} \mathbf{j}_{n,i}^{(p-1)} \right). \tag{2.16}$$

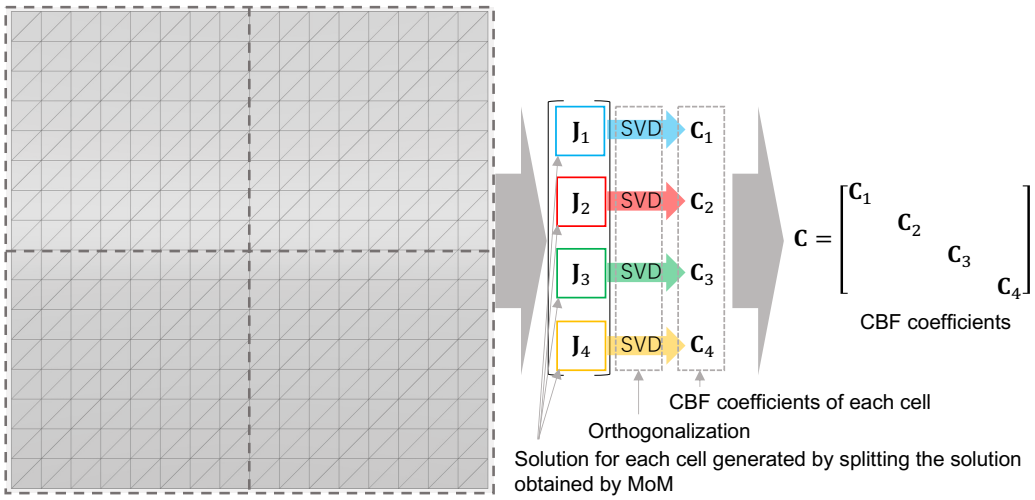

Figure 2.5: Diagram of the IPCBF generation for four cells

This method not only prevents the number of CBFs from increasing, but also efficiently add the effects of the higher-order CBFs to the primary CBFs. Note that equation (2.16) can be interpreted as the solution of the MoM with p iterations of the block Jacobi method (Fig. 2.5). According to this idea, we have further developed a numerical method to obtain IPCBF with the rough use of the Krylov subspace algorithm to (2.8) instead of (2.16) [38]. In our previous study [38], we have used the block BiCGStab [49, 50] for generating the IPCBF. In fact the block BiCGStab seems appropriate for this purpose since it can simultaneously solve linear systems with multiple incident waves by generating the Krylov subspace from the initial residuals based on the incident plane waves with s directions. However the block-type Krylov subspace method is not as effective as was expected since the initial residuals calculated from plane waves with multiple directions are in general almost linearly dependent and thus the dimension of the Krylov subspace is less than the number of the basis functions. By this reason, we utilize the standard generalized minimal residual (GMRES) method [4] as the Krylov subspace algorithm in this chapter. Hence $\mathbf{j}_{m,i}^{(p)}$ is computed one by one for each right hand side (RHS) $\mathbf{v}_i$.

One of issues of the IPCBF is a trade-off between accuracy and computational cost. When the interval of the incident waves for calculating the IPCBF is too wide, we cannot calculate RCS patterns accurately even if the IPCBFs are generated from sufficiently converged iterative solutions obtained with GMRES. On the other hand, it is desirable to use smaller numbers of incident wave sources in order to reduce the computational cost of IPCBF. We therefore propose a hybrid algorithm of using CBFM and the original matrix equation in (2.8) together as a way to obtain a solution with better accuracy while using these IPCBFs. This algorithm utilizes

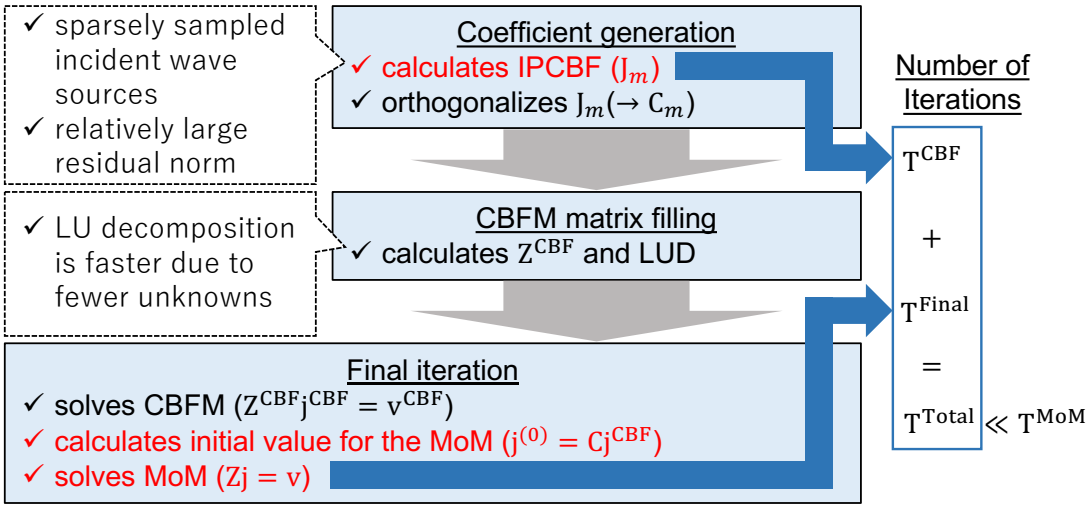

Figure 2.6: Diagram of the proposed algorithm

the feature that one may roughly capture the characteristics of RCS using these IPCBFs.

In this algorithm as shown in Fig. 2.6, the IPCBF is first computed with sparsely sampled incident wave sources and relatively large residual norm. The IPCBF is then used to calculate the unknown current, denoted by $\mathbf{j}^{(0)}$, with CBFM. The current $\mathbf{j}^{(0)}$ is used as the initial value for the iteration in the MoM since $\mathbf{j}^{(0)}$ is expected to broadly capture the characteristics of the correct current $\mathbf{j}$. From a different point of view, one may say that this algorithm tries to reduce the number of iterations of the conventional MoM by improving the initial value with the help of CBFM.

Algorithm 1 shows the proposed hybrid algorithm which consists of three procedures. The first procedure is for the generation of $\mathbf{C}_m$ for the IPCBFs. The loop for $i = 1$ to s is the calculation scheme for the IPCBF $\mathbf{J}_m$. In the next loop for $m = 1$ to N^{Cell}, $\mathbf{J}_m$ is algebraically orthogonalized and compressed by the SVD. The second procedure is for preparing a matrix for the CBFM with the LU decomposition, which is more effective for this procedure than iterative methods since the LU decomposition can efficiently obtain solutions for linear equations with a small coefficient matrix and multiple sources. The third procedure is the final iteration scheme for obtaining the current $\boldsymbol{J}(\boldsymbol{r})$. We first calculate $\mathbf{j}^{\mathrm{CBF}}$, which is the solution of the discretized CFIE:

$$\mathbf{Z}^{\mathrm{CBF}}\mathbf{j}^{\mathrm{CBF}} = \mathbf{v}^{\mathrm{CBF}} \tag{2.17}$$

with the IPCBF, where

$$\mathbf{Z}^{\mathrm{CBF}} = \mathbf{C}^H\mathbf{Z}\mathbf{C}, \tag{2.18}$$

$$\mathbf{v}^{\mathrm{CBF}} = \mathbf{C}^H\mathbf{v}, \tag{2.19}$$

$$\mathbf{C} \equiv \begin{bmatrix} \mathbf{C}_1 & & \\ & \ddots & \\ & & \mathbf{C}_{N^{\mathrm{Cell}}} \end{bmatrix}. \tag{2.20}$$

Then we apply the GMRES to the CFIE discretized with the RWG functions with $\mathbf{Cj}^{\mathrm{CBF}}$ as the initial guess.

The advantage of the proposed method is that it can always converge to within an arbitrary accuracy, even if the solution of CBFM with IPCBF is not accurate. If the accuracy of IPCBF is sufficient, the final iteration scheme is not performed and the solution is obtained. In other words, the proposed method can seamlessly select cases where the accuracy of CBFM is sufficient, and can control the analysis accuracy. In addition, IPCBFs do not require extended regions which are used in the conventional CBFM in order to avoid unnatural behavior of the solution near the boundaries of cells [20]. Furthermore, for the Krylov subspace algorithm, the computation can be made more efficient with the help of FMM [6, 7], which would further speed up the IPCBF generation.

An advantage of the proposed method from the viewpoint of program implementation is that it can use the matrix solving procedure in the conventional MoM code for calculating $\mathbf{C}_m$ and for the final iteration in the hybrid algorithm. There is obviously no complication in the process caused by the extended region. In addition, the advantage of the CBFM implementation that the matrix equation of the CBFM is generated simply by taking the inner product of the coefficient $\mathbf{C}_m$ and $(\mathbf{Z}, \mathbf{v})$ remains unchanged. Therefore, one can easily implement the proposed method using any existing in-house MoM program.

2.4 Numerical results

In this section, we show numerical examples with two types of perfect electric conductor scatterers, a plate and an almond. Hereafter the CBFM using the IPCBFs will be referred to as "IPCBFM" in order to distinguish it from the proposed hybrid algorithm. The residual norms of (2.8) solved in the procedure of the coefficient generation and the final iteration in Algorithm 1 are denoted by δ_{r} and δ_{R}, respectively. The GMRES method [4] and FMM [6, 7] are used in the above procedure. The calculation by the standard MoM is also performed for the comparison with these methods. We use the RCS, denoted by σ, as the evaluation index of the spatial distribution of scattering in the far field. The RCS σ for the current excited by the

Algorithm 1 Hybrid Algorithm using CBFM and MoM

procedure COEFFICIENT GENERATION
  for $i = 1, \cdots, s$ **do**
    Set $\mathbf{v}$ for direction i from (2.10)
    Solve Solve $\mathbf{Z}\mathbf{j}_i = \mathbf{v}$ in (2.8) for $\mathbf{j}_i$ with a tolerance δ_{r}
    for $m = 1, \cdots, N^{\mathrm{Cell}}$ **do**
      Divide $\mathbf{j}_i$ into elements per cell $\mathbf{j}_{m,i}$
    end for
  end for
  for $m = 1, \cdots, N^{\mathrm{Cell}}$ **do**
    Orthogonalize $\mathbf{J}_m \simeq \mathbf{U}_{\mathrm{L}}\mathbf{\Sigma}_{\mathrm{L}}\mathbf{V}_{\mathrm{L}}^H$ by (2.14)
    Assign $\mathbf{U}_{\mathrm{L}}$ to $\mathbf{C}_m$
  end for
end procedure

procedure CBFM MATRIX FILLING
  Compute $\mathbf{Z}^{\mathrm{CBF}}$ in (2.18)
  Decompose $\mathbf{Z}^{\mathrm{CBF}}$ by using LU decomposition
end procedure

procedure FINAL ITERATION
  for $i = 1, \cdots, S$ **do**
    Set $\mathbf{v}^{\mathrm{CBF}}$ for direction i from (2.19)
    Solve $\mathbf{Z}^{\mathrm{CBF}}\mathbf{j}^{\mathrm{CBF}} = \mathbf{v}^{\mathrm{CBF}}$ in (2.17) for $\mathbf{j}^{\mathrm{CBF}}$
    Compute $\mathbf{j}^{(0)}$ and set it as initial value
    Solve $\mathbf{Z}\mathbf{j} = \mathbf{v}$ in (2.8) for $\mathbf{j}$ with a tolerance δ_{R}
    Compute current $\boldsymbol{J}(\boldsymbol{r})$ from (2.7)
  end for
end procedure

incident plane wave $\boldsymbol{E}^{\mathrm{inc}}(\boldsymbol{r})$ is expressed as follows:

$$\sigma = \lim_{r\to\infty} 4\pi r^2 \frac{\left|\boldsymbol{E}^{\mathrm{scat}}(\boldsymbol{r})\right|^2}{\left|\boldsymbol{E}^{\mathrm{inc}}(\boldsymbol{r})\right|^2}, \tag{2.21}$$

where $\boldsymbol{E}^{\mathrm{scat}}(\boldsymbol{r}) = \eta(\mathcal{T}'\boldsymbol{J})(\boldsymbol{r})$ is the scattered field.

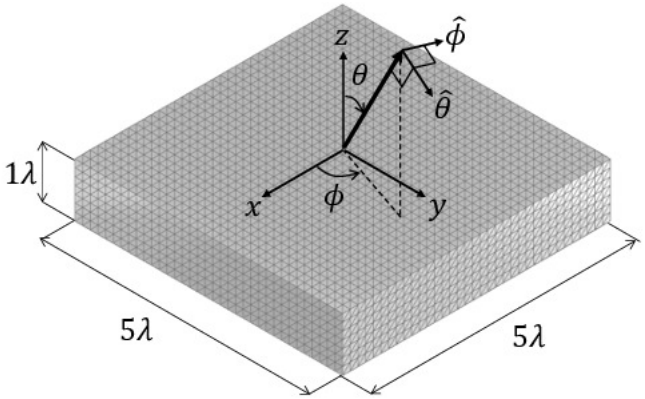

Figure 2.7: Plate

2.4.1 Plate

We calculate the RCS pattern of the plate shown in the Fig. 2.7 and evaluate its analysis accuracy and convergence. The number of the unknowns N in the MoM is 22050. Analysis coordinate plane (the coordinate plane on which σ is calculated) is $z-x$ plane ($\phi = 0^\circ$ plane). We calculate the RCS pattern of $0^\circ \leq \theta \leq 90^\circ$, $\Delta\theta = 1^\circ$ of $\hat{\theta}$ polarization; therefore, the number of the incidence S is equal to 91. The scatterer is divided into 4, 4, and 2 cells in the x, y, and z directions, respectively. The longest side length of the cell l^{Cell} is 1.25λ and the total number of cells N^{Cell} is 32. We set the coefficient γ of CFIE in (2.6) as 2.0×10^{-1}. The typical threshold value δ_{SVD} is usually around 10^{-3} [21]. If the threshold is too large, one may lose necessary CBFs, which makes it difficult to evaluate the characteristics of IPCBFM. To prevent this, we use a smaller value 10^{-7} for δ_{SVD} in this analysis. In this analysis, we set the tolerance of the residual norm δ_{R} to be 10^{-4} at the final iteration in the hybrid algorithm and the MoM.

TABLE 2.1 shows the calculation parameters for generating the CBFs. For conditions 1 to 4, the CBFs are generated by sampling the incident plane wave from the coordinate plane and range in which the RCS is finally computed, and the angular intervals and the residual norms δ_{r} are varied. The polarization of condition 1–4, 6, 7 is $\hat{\theta}$ and that of condition 5 is $\hat{\phi}$. The conditions 6 and 7 have the same number of the incident waves s as in condition 1, but the coordinate planes to be sampled are different from in other conditions. We analyze the effects of the residual norm δ_{r}, the angle interval $\Delta\theta$, the polarization, and the coordinate plane selection on CBF generation and analysis accuracy through these analyses.

Fig. 2.8 shows the number of the CBFs N^{CBF}, the total number of the iterations for the CBF generations T^{CBF} and that for the final iterations T^{Final}. In the hybrid algorithm, if N^{CBF} is small enough, the computational complexity of the SVD

Table 2.1: Parameters for the CBF generations

Condition	$\theta_{\rm s}$	$\phi_{\rm s}$	$\Delta\theta$	$\Delta\phi$	N_θ	N_ϕ	$N_{\rm p}$(Pol.)	$\delta_{\rm r}$
1	0°	0°	10°	0°	10	1	1 ($\hat{\theta}$)	10^{-4}
2	0°	0°	10°	0°	10	1	1 ($\hat{\theta}$)	10^{-2}
3	0°	0°	30°	0°	4	1	1 ($\hat{\theta}$)	10^{-4}
4	0°	0°	30°	0°	4	1	1 ($\hat{\theta}$)	10^{-2}
5	0°	0°	10°	0°	10	1	1 ($\hat{\phi}$)	10^{-4}
6	0°	90°	10°	0°	10	1	1 ($\hat{\theta}$)	10^{-4}
7	90°	0°	0°	10°	1	10	1 ($\hat{\theta}$)	10^{-4}

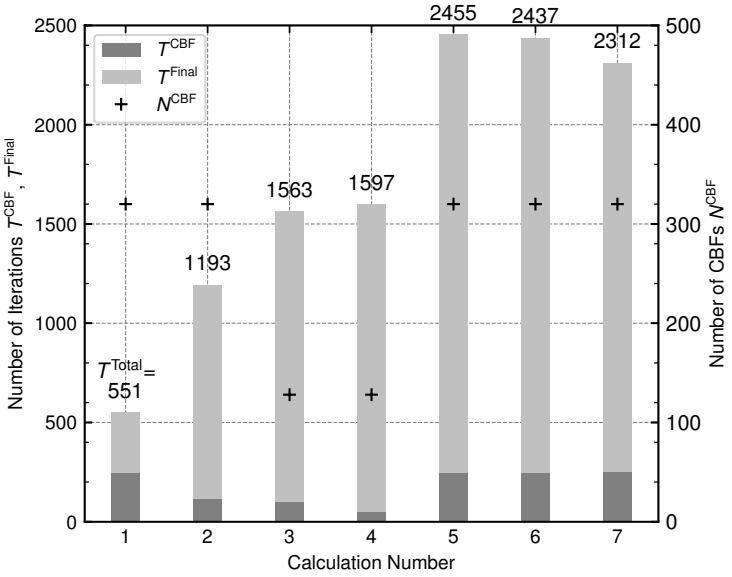

Figure 2.8: Iteration results for the plate

$(O\left(s^2 N_m\right))$ and the LU decomposition $(O\left(\left(N^{\rm CBF}\right)^3\right))$ become much smaller than that of the IPCBF generation and the final iterations. Therefore, the overall computational complexity of the hybrid algorithm will be approximately proportional to the number of these iterations. We thus define the total number of iterations in an analysis as $T^{\rm Total}(= T^{\rm CBF} + T^{\rm Final})$. We note that the number of the iterations for the MoM $T^{\rm MoM}$ is 2122. We also note that $N^{\rm CBF}$ is small enough that the matrix equation shown in (2.17) can be calculated by LU decomposition.

Fig. 2.9 shows the root mean square error (RMSE) for each of conditions in TABLE 2.1. The RMSE of the CBFM relative to the MoM is defined by

$$\mathrm{RMSE} = 10\log 10\left(\frac{\sqrt{\frac{1}{N_\theta}\sum_{i=1}^{N_\theta}\left(\sigma_i^{\rm c}-\sigma_i^{\rm m}\right)^2}}{\max_i\{\sigma_i^{\rm m}\}-\min_i\{\sigma_i^{\rm m}\}}\right)\quad \mathrm{dB}, \tag{2.22}$$

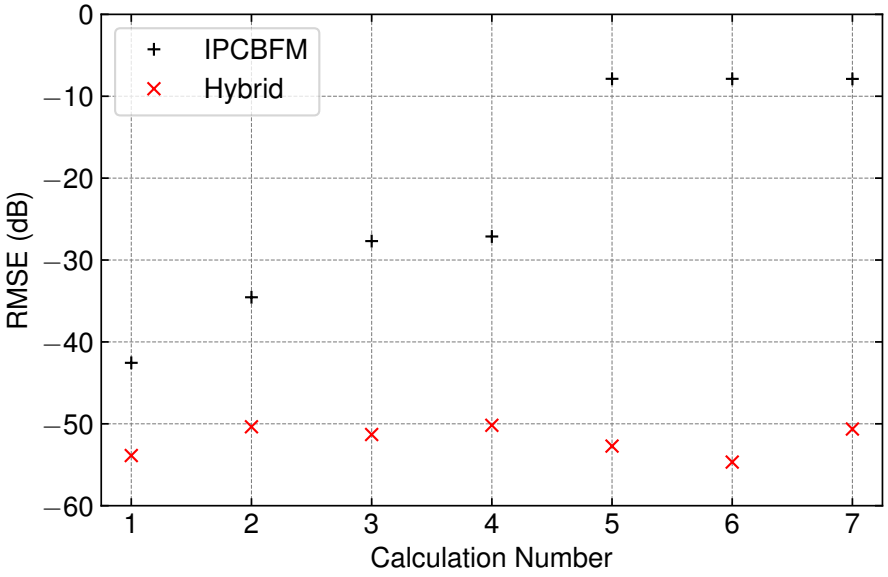

Figure 2.9: RMSE of the plate

where σ_i^{m} (σ_i^{c}) stands for σ computed with MoM (CBFM) for the ith incident wave. In Fig. 2.9, the RMSE for the result of the IPCBFM under the condition 1 in TABLE 2.1 is better than that under the condition 2. It indicates that using a current distribution close to the correct solution for the CBF generation improves the accuracy of the CBFM analysis. As can be seen from the RMSEs for the IPCBFM results under the condition 3 and 4, this will not be the case if the number of CBFs is not sufficient to represent the distribution of induced currents for each direction of the RCS pattern. When the CBFs are generated from the incident plane waves with the orthogonal polarization ($\hat{\phi}$ polarization) in calculation number 5, the RMSE of the IPCBFM becomes over -10 dB. This is also the case when the plane wave is sampled from the coordinate planes ($y-z$ and the $x-y$) different from the plane where the RCS pattern is to be obtained ($z-x$) (i.e., conditions 6 and 7).

One can simply conclude from these results that more incident wave samples are needed to further improve the accuracy of the analysis. On the other hand, as the number of samples is increased, the acceleration effect of the CBFM to the ordinary MoM decreases. The number of sampling points is also largely dependent on the scatterer. As shown in Fig. 2.9, the hybrid algorithm solves this problem. In the present analysis, the hybrid algorithm yields a solution with RMSE below -50 dB, which agrees very well with the MoM results. The total number of iterations for the calculation number 5 to 7 in the hybrid algorithm exceeds that of MoM. It means that the hybrid algorithm is not effective unless the initial values are reasonable. On the other hand, if good initial values are chosen, the hybrid algorithm can speed

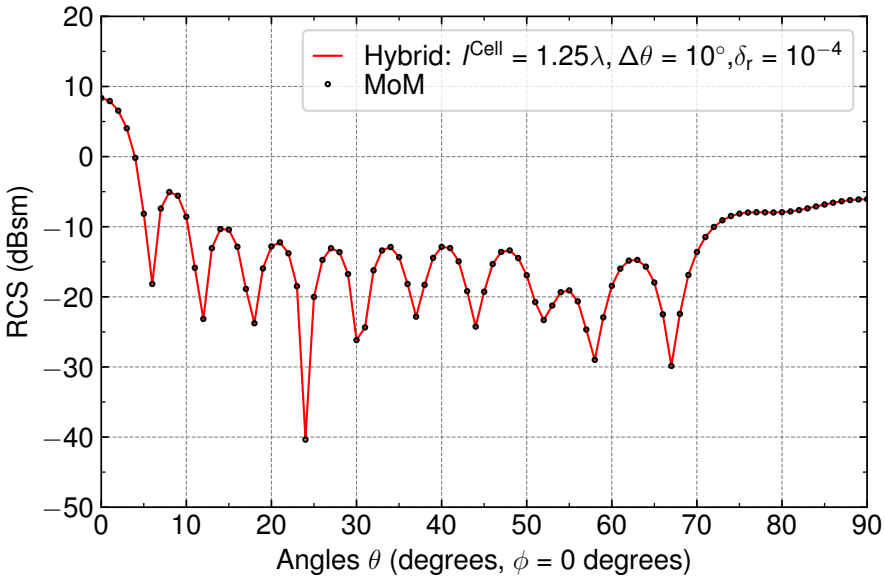

Figure 2.10: RCS of the plate

up the process. In the case of calculation number 1, which meets this condition, the total number of iterations is reduced by a factor of about 1/4.

The RCS patterns of calculation number 1 for the hybrid method, which showed particularly high efficiency in this analysis, are shown in Fig. 2.10. The analysis results agree well with the results of the MoM.

2.4.2 Almond

In this section, we investigate the parameter dependency of the proposed method by analyzing the almond-shaped scatterer [51] in Fig. 2.11 whose longest length is 10λ. The number of the unknowns N is 8244. We calculate the RCS pattern of $-90° \leq \theta \leq 90°$, $\Delta\theta = 0.5°$ of θ polarization ($S = 361$). TABLE 2.2 shows the parameters for the IPCBF generation. In this calculation, we use two types of the CBFs, the IPCBFs and the primary CBFs, and compare the differences between them. We consider two types of the cells: $l^{\mathrm{Cell}} = 1.25\lambda$ and 2.5λ per side. The scatterer is divided into $8 \times 4 \times 2$ cells for $l^{\mathrm{Cell}} = 1.25\lambda$ and $4 \times 2 \times 2$ cells for $l^{\mathrm{Cell}} = 2.5\lambda$ for the x, y, z directions; hence the number of the cells containing the RWGs excluding empty cells are $N^{\mathrm{Cell}} = 60$ and 16, respectively. Then, three intervals of incident angles $\Delta\theta = 2.5°$, $5°$, and $10°$ are considered. The angular range, the polarization, and the sampling coordinate plane are the same as those for the RCS pattern in the final solutions. The residual norm δ_{r} for the IPCBF generation is set as 10^{-4} or 10^{-2}. The currents to generate the primary CBFs is

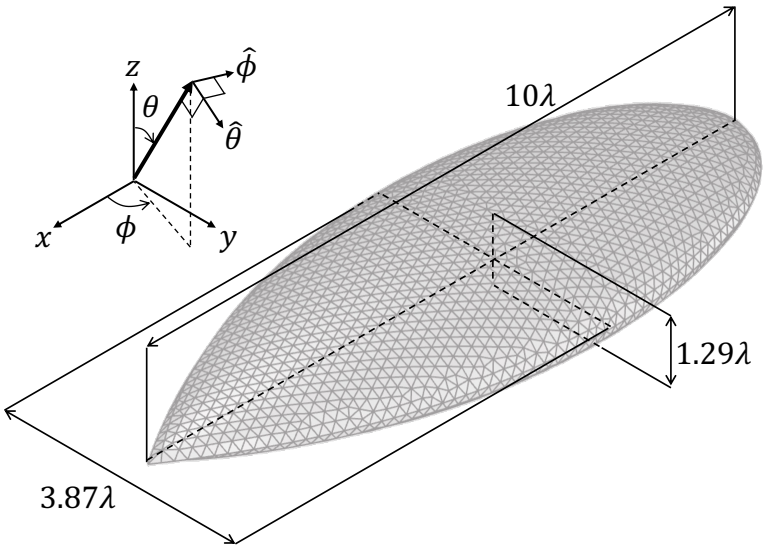

Figure 2.11: Almond

calculated in each cell with the LU decomposition. We consider all combinations of these parameters. The residual norm δ_{R} for final iteration and the MoM is set to 10^{-6}.

Table 2.2: Parameters for the IPCBF generations

Parameter	Value
Cell Size l^{Cell} (N^{Cell})	1.25λ (60), 2.5λ (16)
Interval $\Delta\theta$ ($N_\theta = s$)	10° (19), 5° (37), 2.5° (73)
Polarization	$\hat{\theta}$
Residual Norm δ_{r}	10^{-4}, 10^{-2}
SVD Threshold δ_{SVD}	10^{-7}

The numbers of the CBFs N^{CBF} are shown in Fig. 2.12. Note that N^{CBF}/N is less than one half. Smaller values of the sampling points tend to have fewer N^{CBF} for the IPCBFs. On the other hand, N^{CBF} for the primary CBFs remained almost unchanged even though the number of the sampling points increases. It depends only on the cell size in the case of primary CBFs. This is because the primary CBFs are made from the current of only one cell. In the generation of primary CBFs, there is no significant difference in the current excited in one small cell even if the incident angle is changed slightly in the same coordinate plane. This means that increasing the number of incident wave samples does not lead to an increase in information. When the incident coordinate plane is not limited to that for calculating the RCS, the primary CBF could be sufficiently rich to represent the complex current [21]. However, this results in creating many extra CBFs even

though we only want to obtain the RCS for a specific coordinate plane. On the other hand, the IPCBFs are also CBFs generated for each cell, but their original currents are obtained from calculations for the entire region. Hence the IPCBFs are subject to the effect of currents that vary in a complicated way depending on the direction of the incident wave in a specific coordinate plane. Therefore the IPCBFs can generate many independent CBFs with incident waves on a specific coordinate plane. Also it can be seen in Fig. 2.12 that δ_{r} has almost no effect on the number of CBFs for the same cell size.

Fig. 2.13 to 2.15 shows the the RMSE for the IPCBFM and hybrid method, and ratio of T^{Total} to $T^{\mathrm{MoM}}(= 11110)$ for the hybrid method. In Fig. 2.13, it can be seen that accuracy of the IPCBFM highly depends on the number of the sampling points. On the other hand, no matter what the initial value is, the RMSE will eventually be less than -60 dB in the hybrid method as shown in Fig. 2.14. In other words, the hybrid method allows IPCBFM analysis results to be controlled to any desired level of accuracy. This is also valid when primary CBF is used as CBF. However, since the primary CBF does not give a good initial value, the number of iterations when the hybrid method is used is only 0.9 times the number of iterations when it is not used as shown in Fig. 2.15. On the other hand, when combined with IPCBF, the computation becomes up to 5 times faster. These results indicate that the hybrid method is particularly effective when combined with IPCBF. Fig. 2.16 shows the RCS pattern of the MoM and the hybrid method under the condition of $l^{\mathrm{Cell}} = 1.25\lambda$ and $\delta_{\mathrm{r}} = 10^{-4}$. The results obtained by the proposed method agree well with the MoM results overall. From these results, it can be said that the proposed method is a fast method to obtain RCS patterns in a specific coordinate plane with arbitrary accuracy.

2.5 Conclusion

For reducing the number of iterations and unknowns in the MoM, we proposed a hybrid algorithm combining the CBFM and the MoM by using IPCBFs. The proposed methods are formulated, and verified numerically as we analyze the RCS of two scatterers. By using proposed methods, we could obtain solutions with good accuracy and faster than with conventional method.

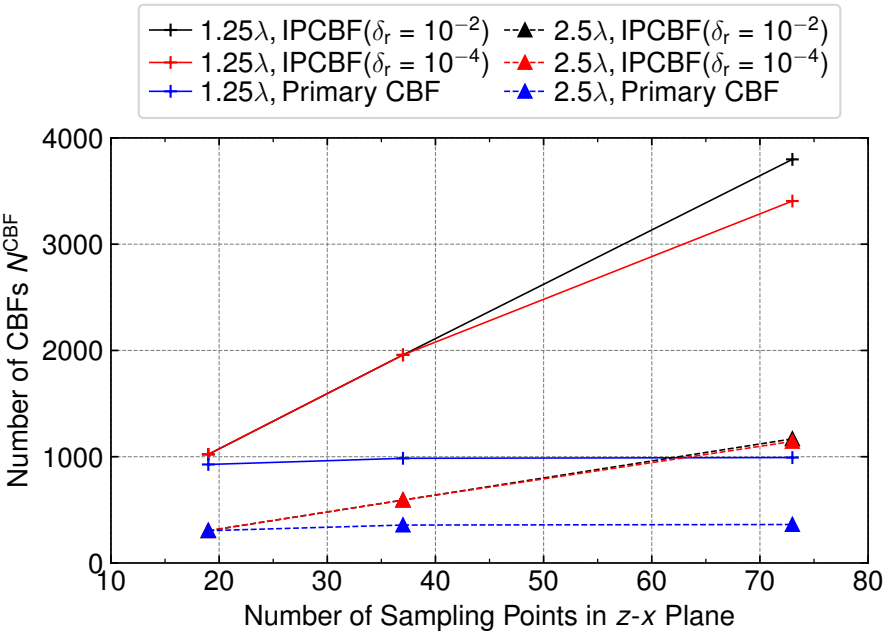

Figure 2.12: Number of CBFs N^{CBF}

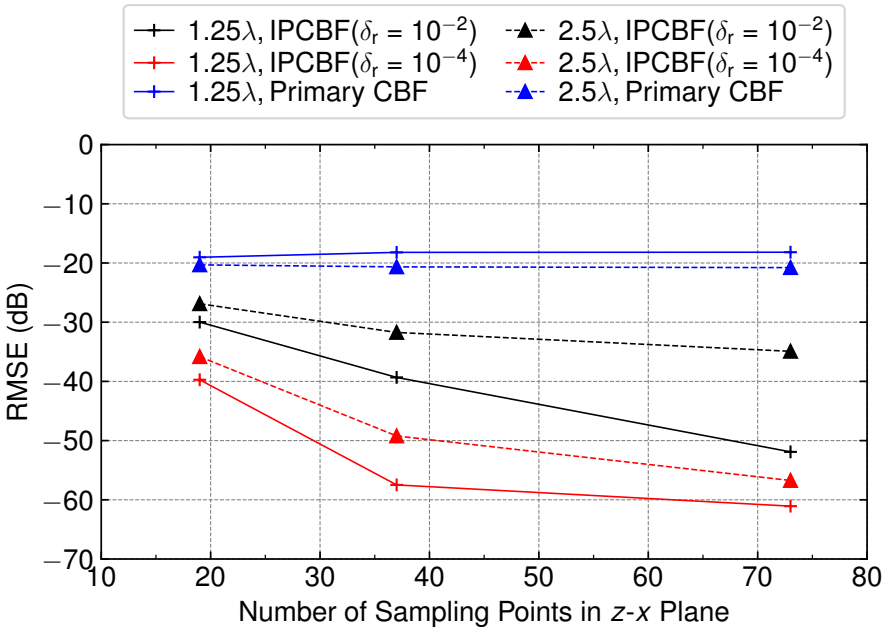

Figure 2.13: RMSE (IPCBFM)

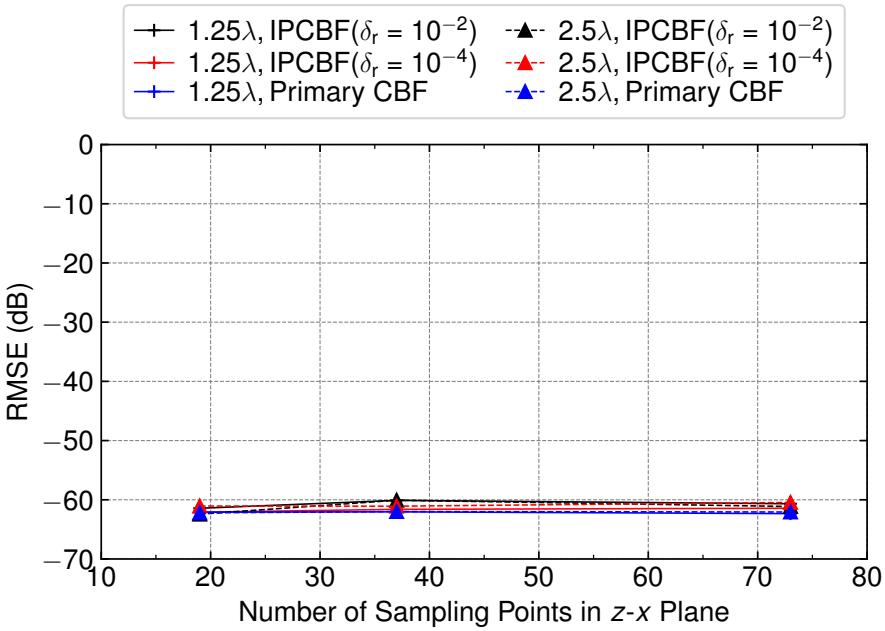

Figure 2.14: RMSE (hybrid method)

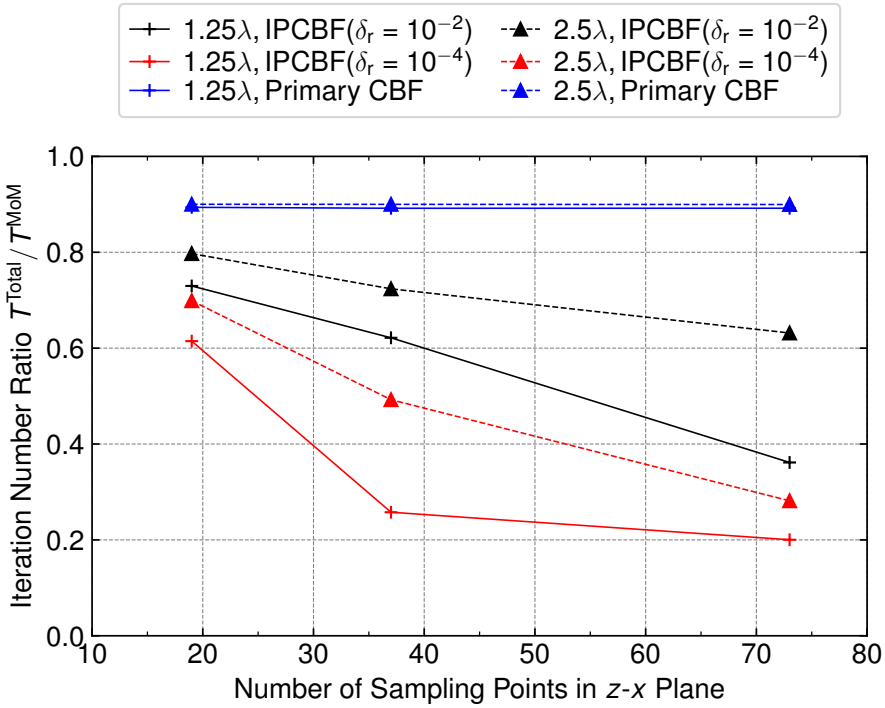

Figure 2.15: Iteration number ratio of $T^{\text{Total}}/T^{\text{MoM}}$

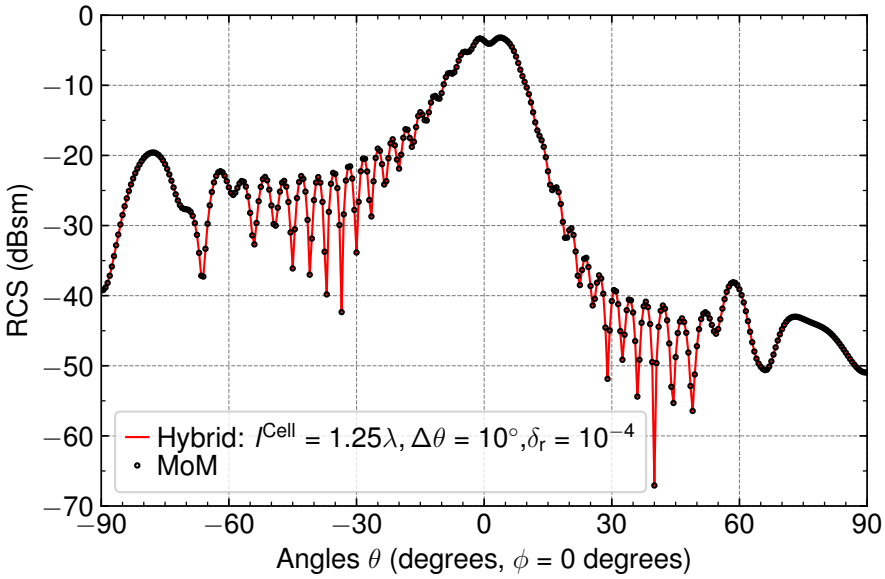

Figure 2.16: RCS pattern of the almond

Chapter 3

Characteristic basis function method combined with Calderón preconditioner for PMCHWT formulation

3.1 Introduction

The goal of research in this chapter is to propose a Calderón preconditioner in the CBFM. We numerically construct two types of mutually-orthogonal basis functions required in the Calderón preconditioner by applying the SVD to the Gram matrix of basis functions obtained in the process of the CBFM. We will show that the basis functions obtained in this way enable the use of the KCP [16, 17] with the PMCHWT formulation, in which these two types of basis functions, respectively, expand the surface electric and magnetic currents, without suffering from bad accuracy due to sharp edges or corners on the boundary observed in [16]. Also this formulation seems to be more natural from the aspect of the CBFM since CBFs in this method are bi-orthogonal as vector fields while the conventional CBFs are orthogonalized as algebraic vectors. The proposed method can be applied to the analyses of both connected and disconnected dielectrics, but is particularly effective for the disconnected cases. Therefore the proposed method is most effective for analyzing structures that are composed of many separate dielectrics such as metamaterials in the optical frequencies. This is why we mainly discuss cases of disconnected scatterers in this chapter.

The rest of this chapter consists of the following four sections. In the next section, we give a preliminary description of the integral equations and the MoM used in

this chapter. Section 3.3 describes the proposed CBFM. In section 3.4 we validate the formulation by analyzing two types of disconnected scatterers. Finally we give some concluding remarks in section 3.5. This is followed by an appendix where we outline some preliminary studies on the use of the proposed method together with IPCBFs in connected scatterer cases in the appendix A.

3.2 PMCHWT formulation

In this section, we formulate the electromagnetic scattering problem for homogeneous dielectric objects and MoM as a method for solving it.

3.2.1 PMCHWT formulation

We consider an electromagnetic wave scattering problem with a homogeneous dielectric object shown in Fig. 3.1. For simplicity we assume that we have a single scatterer in this section. Extension to multiple scatterers is straightforward and indeed we will show some numerical examples with multiple scatterers in section 3.4. The domains outside and inside of the scatterer are denoted by Ω_1 and $\Omega_2 = \mathbb{R}^3 \setminus \overline{\Omega_1}$, respectively. The boundary $\Gamma = \partial\Omega_2$ is a closed surface and the unit normal vector $\hat{\boldsymbol{n}}$ points outward. In the domain Ω_i, the electric field $\boldsymbol{E}(\boldsymbol{r})$ and the magnetic field $\boldsymbol{H}(\boldsymbol{r})$ at the frequency ω satisfy the Maxwell's equations [47] as follows:

$$\begin{aligned} \nabla \times \boldsymbol{E}(\boldsymbol{r}) &= -j\omega\mu_i \boldsymbol{H}(\boldsymbol{r}) \\ \nabla \times \boldsymbol{H}(\boldsymbol{r}) &= j\omega\epsilon_i \boldsymbol{E}(\boldsymbol{r}), \end{aligned}$$

where ϵ_i, μ_i are the permittivity, permeability in Ω_i, and j is imaginary unit, respectively. On the boundary Γ, $\boldsymbol{E}_i(\boldsymbol{r})$ and $\boldsymbol{H}_i(\boldsymbol{r})$, the limit values of $\boldsymbol{E}(\boldsymbol{r})$ and $\boldsymbol{H}(\boldsymbol{r})$ from Ω_i to Γ, satisfy the following boundary conditions:

$$\begin{aligned} \boldsymbol{M}(\boldsymbol{r}) &\equiv \boldsymbol{E}_1(\boldsymbol{r}) \times \hat{\boldsymbol{n}} = \boldsymbol{E}_2(\boldsymbol{r}) \times \hat{\boldsymbol{n}}, \\ \boldsymbol{J}(\boldsymbol{r}) &\equiv \hat{\boldsymbol{n}} \times \boldsymbol{H}_1(\boldsymbol{r}) = \hat{\boldsymbol{n}} \times \boldsymbol{H}_2(\boldsymbol{r}), \end{aligned}$$

where $\boldsymbol{J}(\boldsymbol{r})$ and $\boldsymbol{M}(\boldsymbol{r})$ are the induced electromagnetic currents on the dielectric boundary Γ, respectively. We consider the electromagnetic wave scattering problem of finding $\boldsymbol{E}(\boldsymbol{r})$ and $\boldsymbol{H}(\boldsymbol{r})$ for which the scattered field $(\boldsymbol{E}^{\mathrm{scat}}, \boldsymbol{H}^{\mathrm{scat}}) = (\boldsymbol{E} - \boldsymbol{E}^{\mathrm{inc}}, \boldsymbol{H} - \boldsymbol{H}^{\mathrm{inc}})$ satisfy the radiation condition at $\boldsymbol{r} \to \infty$. $\boldsymbol{E}^{\mathrm{inc}}(\boldsymbol{r})$ and $\boldsymbol{H}^{\mathrm{inc}}(\boldsymbol{r})$ are the electric and magnetic incident fields, respectively. For this wave scattering problem the integral equations based on the PMCHWT formulation [5,6]

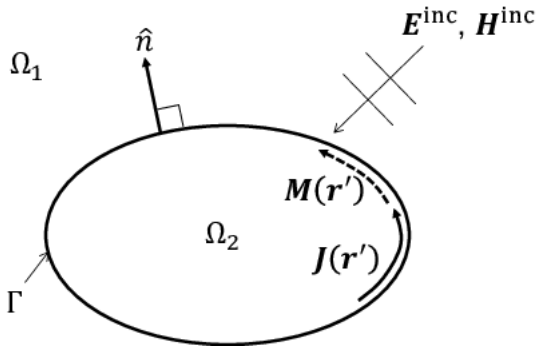

Figure 3.1: Definition of the domain

are written as follows:

$$\sum_{i=1}^{2} \left\{ \left(\mathcal{K}_i \boldsymbol{M}\right)(\boldsymbol{r}) - \eta_i \left(\mathcal{T}_i \boldsymbol{J}\right)(\boldsymbol{r}) \right\} = \hat{\boldsymbol{n}} \times \boldsymbol{E}^{\text{inc}}(\boldsymbol{r}) \tag{3.1}$$

$$\sum_{i=1}^{2} \left\{ \frac{1}{\eta_i} \left(\mathcal{T}_i \boldsymbol{M}\right)(\boldsymbol{r}) + \left(\mathcal{K}_i \boldsymbol{J}\right)(\boldsymbol{r}) \right\} = -\hat{\boldsymbol{n}} \times \boldsymbol{H}^{\text{inc}}(\boldsymbol{r}), \tag{3.2}$$

where $\eta_i = \sqrt{\mu_i/\epsilon_i}$ is wave impedance in Ω_i. The integral operators $\mathcal{K}_i$ and $\mathcal{T}_i$ are defined by

$$\left(\mathcal{K}_i \boldsymbol{X}\right)(\boldsymbol{r}) = \hat{\boldsymbol{n}} \times P.V. \int_{\Gamma} \nabla G_i(\boldsymbol{r}, \boldsymbol{r}') \times \boldsymbol{X}(\boldsymbol{r}')\, d\boldsymbol{r}' \tag{3.3}$$

$$\left(\mathcal{T}_i \boldsymbol{X}\right)(\boldsymbol{r}) = jk_i \hat{\boldsymbol{n}} \times F.P. \int_{\Gamma} \left(\mathcal{I} + \frac{\nabla\nabla}{k_i^2}\right) G_i(\boldsymbol{r}, \boldsymbol{r}') \boldsymbol{X}(\boldsymbol{r}')\, d\boldsymbol{r}' \tag{3.4}$$

where $G_i(\boldsymbol{r}, \boldsymbol{r}')$ is Green's function of the Helmholtz' equation for the observation point $\boldsymbol{r}$ and the source point $\boldsymbol{r}'$ in three dimension represented by

$$G_i(\boldsymbol{r}, \boldsymbol{r}') = \frac{e^{-jk_i|\boldsymbol{r}-\boldsymbol{r}'|}}{4\pi|\boldsymbol{r}-\boldsymbol{r}'|}. \tag{3.5}$$

In (3.3) and (3.4), *P.V.*, *F.P.* and $\mathcal{I}$ stand for the Cauchy principal value integral, finite part and the identity operator, respectively. The parameter k_i is the wave number in Ω_i defined as $k_i = 2\pi/\lambda_i$ with the wavelength λ_i. Omitting the notation "$(\boldsymbol{r})$" for simplicity, we can express the integral equations in (3.1) and (3.2) by

$$\begin{bmatrix} \sum_{i=1}^{2} \mathcal{K}_i & -\sum_{i=1}^{2} \eta_i \mathcal{T}_i \\ \sum_{i=1}^{2} \frac{1}{\eta_i} \mathcal{T}_i & \sum_{i=1}^{2} \mathcal{K}_i \end{bmatrix} \begin{bmatrix} \boldsymbol{M} \\ \boldsymbol{J} \end{bmatrix} = \begin{bmatrix} \hat{\boldsymbol{n}} \times \boldsymbol{E}^{\text{inc}} \\ -\hat{\boldsymbol{n}} \times \boldsymbol{H}^{\text{inc}} \end{bmatrix}. \tag{3.6}$$

3.2.2 Discretization of the integral equation

The PMCHWT formulation in (3.6) is discretized with the Galerkin method [1] in this thesis. The electromagnetic currents are approximated by linear combinations of the basis functions $\boldsymbol{b}_n^{\mathrm{J,M}}(\boldsymbol{r})$ with the expansion coefficients $\alpha_n^{\mathrm{J,M}}$ as follows:

$$\boldsymbol{J}(\boldsymbol{r}) \approx \sum_{n=1}^{N^{\mathrm{J}}} \alpha_n^{\mathrm{J}} \boldsymbol{b}_n^{\mathrm{J}}(\boldsymbol{r}) \tag{3.7}$$

$$\boldsymbol{M}(\boldsymbol{r}) \approx \sum_{n=1}^{N^{\mathrm{M}}} \alpha_n^{\mathrm{M}} \boldsymbol{b}_n^{\mathrm{M}}(\boldsymbol{r}) \tag{3.8}$$

where N^{J} and N^{M} are the total numbers of the basis functions for the electric and magnetic currents, denoted by $\boldsymbol{b}_n^{\mathrm{J}}$ and $\boldsymbol{b}_n^{\mathrm{M}}$, respectively. Hence the total number of the unknowns N for our problems is $N^{\mathrm{J}} + N^{\mathrm{M}}$. Since the scatterer defined in this thesis does not contain perfect electric conductors, N^{J} is equal to N^{M}. The discretized operators $[\mathbf{K}_i]_{m,n}$, $[\mathbf{T}_i]_{m,n}$ for elements m and n are described as

$$\left[\mathbf{K}_i^{tb}\right]_{m,n} = \int_{\boldsymbol{t}_m} \hat{\boldsymbol{n}} \times \boldsymbol{t}_m(\boldsymbol{r}) \cdot \left(\hat{\boldsymbol{n}} \times P.V. \int_{\boldsymbol{b}_n} \nabla G_i(\boldsymbol{r}, \boldsymbol{r}') \times \boldsymbol{b}_n(\boldsymbol{r}')\, d\boldsymbol{r}'\right) d\boldsymbol{r}, \tag{3.9}$$

$$\left[\mathbf{T}_i^{tb}\right]_{m,n} = jk_i \int_{\boldsymbol{t}_m} \hat{\boldsymbol{n}} \times \boldsymbol{t}_m(\boldsymbol{r}) \cdot \left(\hat{\boldsymbol{n}} \times F.P. \int_{\boldsymbol{b}_n} \left(\mathcal{I} + \frac{\nabla\nabla}{k_i^2}\right) G_i(\boldsymbol{r}, \boldsymbol{r}') \cdot \boldsymbol{b}_n(\boldsymbol{r}')\, d\boldsymbol{r}'\right) d\boldsymbol{r} \tag{3.10}$$

where $\boldsymbol{t}_n$ is a test function and $\int_{\boldsymbol{t}_n}$ stands for an integral over the support of $\boldsymbol{t}_n$. The superscripts t and b in $\mathbf{K}_i^{tb}$ and $\mathbf{T}_i^{tb}$ represent the types of test and trial (basis) functions. The discretized incident electric field $\left[\mathbf{v}_t^{\mathrm{E}}\right]_m$ and magnetic field $\left[\mathbf{v}_t^{\mathrm{H}}\right]_m$ corresponding to element m are expressed by

$$\left[\mathbf{v}_t^{\mathrm{E}}\right]_m = \int_{\boldsymbol{t}_m} \hat{\boldsymbol{n}} \times \boldsymbol{t}_m(\boldsymbol{r}) \cdot \left(\hat{\boldsymbol{n}} \times \boldsymbol{E}^{\mathrm{inc}}(\boldsymbol{r})\right) d\boldsymbol{r},$$

$$\left[\mathbf{v}_t^{\mathrm{H}}\right]_m = -\int_{\boldsymbol{t}_m} \hat{\boldsymbol{n}} \times \boldsymbol{t}_m(\boldsymbol{r}) \cdot \left(\hat{\boldsymbol{n}} \times \boldsymbol{H}^{\mathrm{inc}}(\boldsymbol{r})\right) d\boldsymbol{r}.$$

With these notations, the discretized matrix equation can be written as follows.

$$\mathbf{Z}_{t^J t^M b^M b^J} \mathbf{j} = \mathbf{v}_{t^J t^M}, \tag{3.11}$$

$$\mathbf{Z}_{t^J t^M b^M b^J} = \sum_{i=1}^{2} \begin{bmatrix} \mathbf{K}_i^{t^J b^M} & -\eta_i \mathbf{T}_i^{t^J b^J} \\ \frac{1}{\eta_i} \mathbf{T}_i^{t^M b^M} & \mathbf{K}_i^{t^M b^J} \end{bmatrix} \in \mathbb{C}^{N \times N}, \tag{3.12}$$

$$\mathbf{v}_{t^J t^M} = \begin{bmatrix} \mathbf{v}_{t^J}^{\mathrm{E}} \\ \mathbf{v}_{t^M}^{\mathrm{H}} \end{bmatrix} \in \mathbb{C}^N, \tag{3.13}$$

and the expansion coefficient vector $\mathbf{j} \in \mathbb{C}^N$ is written as

$$\mathbf{j} = \left[\begin{bmatrix} \alpha_1^{\mathrm{M}} & \cdots & \alpha_{N^{\mathrm{M}}}^{\mathrm{M}} \end{bmatrix} \begin{bmatrix} \alpha_1^{\mathrm{J}} & \cdots & \alpha_{N^{\mathrm{J}}}^{\mathrm{J}} \end{bmatrix}\right]^T. \tag{3.14}$$

The 1st and 2nd subscripts of $\mathbf{Z}_{t^J t^M b^M b^J}$ respectively correspond to the types of test functions for the 1st and 2nd row of (3.12) while the 3rd and 4th subscripts to the types of trial functions for the surface magnetic and electric currents. Also the 1st and 2nd subscripts of $\mathbf{v}_{t^J t^M}$ represent the types of test functions for the 1st and 2nd rows of (3.13), respectively. Note that we will eventually use different basis functions for the test functions of the 1st and 2nd rows in (3.12) and (3.13) as well as for the trial functions of the magnetic and electric currents. This is crucial in the use of the Calderón preconditioner as will be shown in the next section.

3.2.3 Calderón preconditioning

The Calderón preconditioning is one of numerical methods to accelerate the convergence of iterative linear solvers for integral equations. This method constructs a preconditioner based on the Calderón formulae given by

$$\begin{bmatrix} \mathcal{K}_i & -\eta_i \mathcal{T}_i \\ \frac{1}{\eta_i}\mathcal{T}_i & \mathcal{K}_i \end{bmatrix} \begin{bmatrix} \mathcal{K}_i & -\eta_i \mathcal{T}_i \\ \frac{1}{\eta_i}\mathcal{T}_i & \mathcal{K}_i \end{bmatrix} = \frac{\mathcal{I}}{4}.$$

From this equation we expect that the square of the operator in (3.6) is well-conditioned. Indeed it is true in a sense that the operator satisfies

$$\begin{bmatrix} \sum_{i=1}^2 \mathcal{K}_i & -\sum_{i=1}^2 \eta_i \mathcal{T}_i \\ \sum_{i=1}^2 \frac{1}{\eta_i}\mathcal{T}_i & \sum_{i=1}^2 \mathcal{K}_i \end{bmatrix} \cdot \begin{bmatrix} \sum_{i=1}^2 \mathcal{K}_i & -\sum_{i=1}^2 \eta_i \mathcal{T}_i \\ \sum_{i=1}^2 \frac{1}{\eta_i}\mathcal{T}_i & \sum_{i=1}^2 \mathcal{K}_i \end{bmatrix} = \mathcal{S} + \mathcal{K}$$

where $\mathcal{S}$ is a bounded operator with a bounded inverse and $\mathcal{K}$ is a compact operator. Hence we can construct a right preconditioner by discretizing the integral equation

$$\begin{bmatrix} \sum_{i=1}^2 \mathcal{K}_i & -\sum_{i=1}^2 \eta_i \mathcal{T}_i \\ \sum_{i=1}^2 \frac{1}{\eta_i}\mathcal{T}_i & \sum_{i=1}^2 \mathcal{K}_i \end{bmatrix} \cdot \begin{bmatrix} \sum_{i=1}^2 \mathcal{K}_i & -\sum_{i=1}^2 \eta_i \mathcal{T}_i \\ \sum_{i=1}^2 \frac{1}{\eta_i}\mathcal{T}_i & \sum_{i=1}^2 \mathcal{K}_i \end{bmatrix} \begin{bmatrix} \boldsymbol{M}' \\ \boldsymbol{J}' \end{bmatrix} = \begin{bmatrix} \hat{\boldsymbol{n}} \times \boldsymbol{E}^{\text{inc}} \\ -\hat{\boldsymbol{n}} \times \boldsymbol{H}^{\text{inc}} \end{bmatrix}, \quad (3.15)$$

where

$$\begin{bmatrix} \boldsymbol{M} \\ \boldsymbol{J} \end{bmatrix} = \begin{bmatrix} \sum_{i=1}^2 \mathcal{K}_i & -\sum_{i=1}^2 \eta_i \mathcal{T}_i \\ \sum_{i=1}^2 \frac{1}{\eta_i}\mathcal{T}_i & \sum_{i=1}^2 \mathcal{K}_i \end{bmatrix} \begin{bmatrix} \boldsymbol{M}' \\ \boldsymbol{J}' \end{bmatrix}. \quad (3.16)$$

It is known that a naive discretization of equation (3.15) which uses only the RWG basis functions $\boldsymbol{f}$ for both test and trial functions (for both $\mathbf{J}$ and $\mathbf{M}$)

$$\begin{aligned} \mathbf{Z}_{ffff}\mathbf{G}_{ffff}^{-1}\mathbf{Z}_{ffff}\mathbf{G}_{ffff}^{-1}\tilde{\mathbf{j}} &= \mathbf{v}_{ff}, \\ \mathbf{j} &= \mathbf{G}_{ffff}^{-1}\mathbf{Z}_{ffff}\mathbf{G}_{ffff}^{-1}\tilde{\mathbf{j}}, \end{aligned}$$

does not make sense since the Gram matrix of the RWG basis function $\mathbf{j}$ defined by

$$\mathbf{G}_{ffff} = \begin{bmatrix} \int_\Gamma (\hat{\boldsymbol{n}} \times \boldsymbol{f}_i(\mathbf{r})) \cdot \boldsymbol{f}_j(\mathbf{r}) d\boldsymbol{r} & 0 \\ 0 & \int_\Gamma (\hat{\boldsymbol{n}} \times \boldsymbol{f}_i(\mathbf{r})) \cdot \boldsymbol{f}_j(\mathbf{r}) d\boldsymbol{r} \end{bmatrix}$$

is a singular matrix, where $\mathbf{Z}_{ffff}$ is the matrix defined in (3.12) with the RWG basis functions for all the trial and test functions. One of feasible discretization methods for (3.15) to avoid this problem is to use the BC basis functions $\boldsymbol{g}$ for the preconditioner, namely to discretize (3.15) into

$$\begin{aligned}\mathbf{Z}_{ffff}\mathbf{G}_{ggff}^{-1}\mathbf{Z}_{gggg}\mathbf{G}_{ffgg}^{-1}\tilde{\mathbf{j}} &= \mathbf{v}_{ff},\\ \mathbf{j} &= \mathbf{G}_{ggff}^{-1}\mathbf{Z}_{gggg}\mathbf{G}_{ffgg}^{-1}\tilde{\mathbf{j}},\end{aligned}$$

where $\mathbf{G}_{ggff}$ and $\mathbf{G}_{ffgg}$ are the Gram matrices defined as follows:

$$\mathbf{G}_{ggff} = -\mathbf{G}_{ffgg} = \begin{bmatrix} \int_\Gamma (\hat{\boldsymbol{n}} \times \boldsymbol{g}_i(\boldsymbol{r})) \cdot \boldsymbol{f}_j(\boldsymbol{r})\, d\boldsymbol{r} & 0 \\ 0 & \int_\Gamma (\hat{\boldsymbol{n}} \times \boldsymbol{g}_i(\boldsymbol{r})) \cdot \boldsymbol{f}_j(\boldsymbol{r})\, d\boldsymbol{r} \end{bmatrix},$$

and $\mathbf{Z}_{gggg}$ has the same definition as $\mathbf{Z}_{ffff}$, except that it uses the BC basis functions.

Another alternative is to expand the electric and magnetic currents with the RWG and BC basis functions, respectively, with appropriately chosen test functions [16, 18], i.e.:

$$\mathbf{Z}_{gffg}\mathbf{G}_{gffg}^{-1}\mathbf{Z}_{gffg}\mathbf{G}_{gffg}^{-1}\tilde{\mathbf{j}} = \mathbf{v}_{gf}, \tag{3.17}$$

$$\mathbf{j} = \mathbf{G}_{gffg}^{-1}\mathbf{Z}_{gffg}\mathbf{G}_{gffg}^{-1}\tilde{\mathbf{j}}, \tag{3.18}$$

where

$$\begin{aligned}\mathbf{Z}_{gffg} &= \sum_{i=1}^{2} \begin{bmatrix} \mathbf{K}_i^{gf} & -\eta_i \mathbf{T}_i^{gg} \\ \frac{1}{\eta_i}\mathbf{T}_i^{ff} & \mathbf{K}_i^{fg} \end{bmatrix},\\ \mathbf{G}_{gffg} &= \begin{bmatrix} \int_\Gamma (\hat{\boldsymbol{n}} \times \boldsymbol{g}_i(\boldsymbol{r})) \cdot \boldsymbol{f}_j(\boldsymbol{r})\, d\boldsymbol{r} & 0 \\ 0 & \int_\Gamma (\hat{\boldsymbol{n}} \times \boldsymbol{f}_i(\boldsymbol{r})) \cdot \boldsymbol{g}_j(\boldsymbol{r})\, d\boldsymbol{r} \end{bmatrix}.\end{aligned}$$

One may implement a CMP using equations (3.17) and (3.18). Note that the GMRES method [4] applied to the right preconditioned equations in (3.17) and (3.18) finds a minimizer of the residual in the following affine space after n iterations of the scheme:

$$\mathbf{j}_0 + \mathbf{G}_{gffg}^{-1}\left\{\tilde{\mathbf{Z}}_{gffg}\mathbf{r}_0, \tilde{\mathbf{Z}}_{gffg}^3\mathbf{r}_0, \tilde{\mathbf{Z}}_{gffg}^5\mathbf{r}_0, \cdots, \tilde{\mathbf{Z}}_{gffg}^{2n-1}\mathbf{r}_0\right\}, \tag{3.19}$$

where $\tilde{\mathbf{Z}}_{gffg} = \mathbf{Z}_{gffg}\mathbf{G}_{gffg}^{-1}$, $\mathbf{j}_0$ is the initial guess of $\mathbf{j}$, and $\mathbf{r}_0$ is the initial residual.

Similarly, $2n$ GMRES iterations applied to the following discretized integral equation

$$\mathbf{Z}_{gffg}\mathbf{G}_{gffg}^{-1}\tilde{\mathbf{j}} = \mathbf{v}_{gf}, \tag{3.20}$$

$$\mathbf{j} = \mathbf{G}_{gffg}^{-1}\tilde{\mathbf{j}}, \tag{3.21}$$

find a minimizer of the residual in the affine space given by

$$\mathbf{j}_0 + \mathbf{G}_{gffg}^{-1}\left\{\mathbf{r}_0, \tilde{\mathbf{Z}}_{gffg}\mathbf{r}_0, \tilde{\mathbf{Z}}_{gffg}^2\mathbf{r}_0, \cdots, \tilde{\mathbf{Z}}_{gffg}^{2n-1}\mathbf{r}_0\right\}, \tag{3.22}$$

which includes (3.19) as a proper subset. Hence, the GMRES for (3.20) gives a smaller residual than that for (3.17) after $2n-1$ multiplications of $\tilde{\mathbf{Z}}_{gffg}$, i.e. after almost the same amount of computational time. As mentioned in the chapter 1, we call the preconditioning based on (3.20) and (3.21) as KCP. KCP is a simplified implementation of the Calderón preconditioning which is possible only if the original matrix ($\tilde{\mathbf{Z}}_{gffg}$ in the present case) and the preconditioner are identical. Obviously, KCP enjoys both fast convergence guaranteed by the Calderón formula and the simplicity of the formulation thanks to the use of GMRES. See [16, 17] for more details on the KCP.

3.3 CBFM with Calderón preconditioning

In this section we formulate the CBFM and its acceleration with the Calderón preconditioning.

3.3.1 CBF generation

In the CBFM [20]– [23], the scatterer is divided into N^{Cell} cells and CBFs are generated for each cell. Fig. 3.2 shows an example of cell division of a scatterer. Dotted black lines in the figure represent the cell boundaries for $N^{\text{Cell}} = 4$. The region containing the support of all RWGs in cell m, indicated by the gray region, is defined as Γ_m. Note that an edge always belongs to one and only one cell.

The CBFs defined in cell m are represented by linear combinations of the RWGs contained in that cell. The nth CBF $\boldsymbol{c}_{mn}(\boldsymbol{r})$ in cell m is expressed by

$$\boldsymbol{c}_{mn}(\boldsymbol{r}) = \sum_{i=1}^{N_m} c_{mni}\boldsymbol{f}_{\Lambda_{mi}}(\boldsymbol{r}) \quad (n = 1, \cdots L_m), \tag{3.23}$$

where N_m and Λ_{mi} are the total number and index of the RWG functions in cell m, L_m is the total number of CBFs, and c_{mni} is the coefficient of the RWG for the CBF $\boldsymbol{c}_{mn}(\boldsymbol{r})$, respectively. The matrix of the coefficients c_{mni} in cell m is denoted by $\mathbf{C}_m \in \mathbb{C}^{N_m \times L_m}$;

$$\left[\mathbf{C}_m\right]_{in} = c_{mni}.$$

In this thesis, the coefficient $\mathbf{C}_m$ is also referred to as "CBF" unless it leads to confusion.

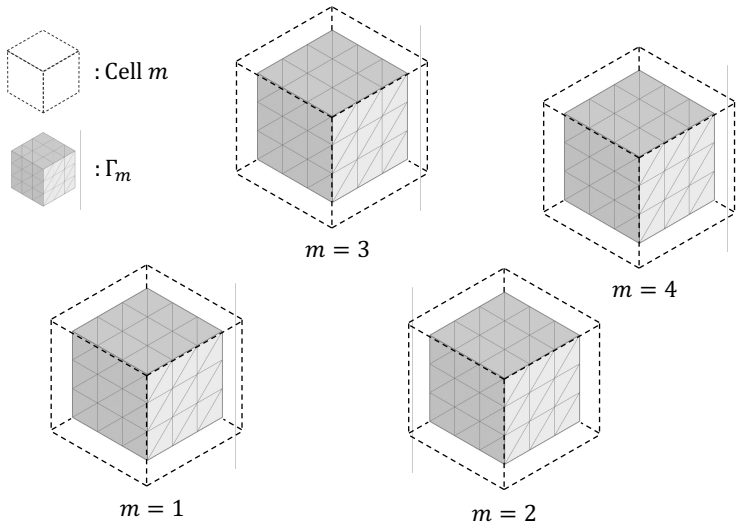

Figure 3.2: Division of scatterers into cells.

One can obtain CBFs by solving scattering problems with multiple incident fields. In this thesis, plane waves propagating in s directions sampled at an appropriate interval on the unit sphere are used as incident fields. For instance, if N_θ (N_ϕ) samples are used in the θ (ϕ) direction and $N_\mathrm{p}(= 1, 2)$ orthogonal polarization samples are considered, we have $s = N_\theta N_\phi N_\mathrm{p}$. From the s plane waves, we compute the sets of coefficients $\mathbf{J}_m^\mathrm{J}$ and $\mathbf{J}_m^\mathrm{M} \in \mathbb{C}^{N_m \times s}$, which correspond to solutions of scattering problems with the electric and magnetic incident fields illuminating the cell m. We then obtain the CBFs $\mathbf{C}_m^{\mathrm{J,M}}$ by orthogonalizing $\mathbf{J}_m^{\mathrm{J,M}}$. In the rest of this subsection we discuss how to determine $\mathbf{J}_m^{\mathrm{J,M}}$. The orthogonalization process to obtain $\mathbf{C}_m^{\mathrm{J,M}}$ from $\mathbf{J}_m^{\mathrm{J,M}}$ is described in section 3.3.2.

There are several options for generating $\mathbf{J}_m^{\mathrm{J,M}}$, depending on whether or not mutual couplings between cells is considered. The primary CBFs are the macro basis functions generated without taking into account the mutual couplings between cells. The expansion coefficients $\mathbf{J}_m^\mathrm{M}$ and $\mathbf{J}_m^\mathrm{J}$ for the primary CBF can be calculated from the following equation [21]:

$$
\begin{aligned}
\mathbf{Z}_{mm}\mathbf{J}_m &= \mathbf{V}_m \qquad (3.24)\\
\mathbf{Z}_{mm} &= \sum_{i=1}^{2} \begin{bmatrix} \left(\mathbf{K}_i^{ff}\right)_{mm} & -\eta_i \left(\mathbf{T}_i^{ff}\right)_{mm} \\ \frac{1}{\eta_i}\left(\mathbf{T}_i^{ff}\right)_{mm} & \left(\mathbf{K}_i^{ff}\right)_{mm} \end{bmatrix} \\
\mathbf{J}_m &= \begin{bmatrix} \mathbf{J}_m^\mathrm{M} \\ \mathbf{J}_m^\mathrm{J} \end{bmatrix} \\
\mathbf{V}_m &= \begin{bmatrix} \mathbf{V}_m^\mathrm{E} \\ \mathbf{V}_m^\mathrm{H} \end{bmatrix}
\end{aligned}
$$

where $\left(\mathbf{K}_i^{ff}\right)_{mm} \in \mathbb{C}^{N_m \times N_m}$ denotes the submatrix of $\mathbf{K}_i^{ff}$ formed by N_m RWGs in cell m, etc., and $\mathbf{V}_m^{\mathrm{E,H}} \in \mathbb{C}^{N_m \times s}$ is the matrix of incident plane waves $\mathbf{v}$ for cell m. The primary CBFs are particularly useful for analyzing scatterers with periodic or quasi-periodic structures, such as array antennas or frequency selective surfaces whose components are separated from each other. In such cases, it is convenient to configure each cell to contain one or several scatterers. In the examples presented in the main body of this chapter, we will restrict our attention to primary CBFs using this type of cell arrangement. See appendix A for another choice.

3.3.2 CBF orthogonalization considering the property of the electromagnetic currents

The coefficient sets $\mathbf{J}_m^{\mathrm{J,M}}$ obtained in the last subsection cannot be directly used as basis functions since they can be linearly-dependent. Hence we orthogonalize CBFs in cell m using the SVD [21–23]. In the conventional CBFMs, the SVD is usually applied to the set $\mathbf{J}_m^{\mathrm{J}}$ and $\mathbf{J}_m^{\mathrm{M}}$ separately. The orthogonalized set for the electric current in cell m, for example, is obtained with the SVD as follows:

$$\mathbf{J}_m^{\mathrm{J}} = \begin{bmatrix} \tilde{\mathbf{U}}_1 & \tilde{\mathbf{U}}_2 \end{bmatrix} \begin{bmatrix} \tilde{\mathbf{\Sigma}}_1 & \\ & \tilde{\mathbf{\Sigma}}_2 \end{bmatrix} \begin{bmatrix} \tilde{\mathbf{V}}_1^H \\ \tilde{\mathbf{V}}_2^H \end{bmatrix}, \tag{3.25}$$

where $\tilde{\mathbf{U}}_i$ and $\tilde{\mathbf{V}}_i$ $(i = 1, 2)$ are matrices having the singular vectors as their columns. Also, $\tilde{\Sigma}_i$ is a diagonal matrix with singular values as its diagonal components in descending order. $\tilde{\Sigma}_1$ contains all the singular values exceeding the pre-defined threshold while singular values in $\tilde{\Sigma}_2$ are less than the threshold. We now take columns of $\tilde{\mathbf{U}}_1$ as linearly independent CBFs $\mathbf{C}_m^{\mathrm{J}}$ for representing the electric currents in the cell m. The CBFs $\mathbf{C}_m^{\mathrm{M}}$ for representing the magnetic currents in the cell m is calculated similarly by applying (3.25) to $\mathbf{J}_m^{\mathrm{M}}$. We note that CBFs for electric and magnetic currents thus obtained are not related. However, it is natural to ask if these basis functions can have a duality structure as do the RWG and BC basis functions, for example. If this is possible, one may establish a method of analysis that combines the advantages of CBFM and KCP, with fewer unknowns and faster convergence than the conventional method.

We now start with the definition of the duality. The CBFs $\boldsymbol{c}_{mi}^{\mathrm{M}}$ $(i = 1, \cdots, L_m^{\mathrm{M}})$ and $\boldsymbol{c}_{mj}^{\mathrm{J}}$ $(j = 1, \cdots, L_m^{\mathrm{J}})$ for magnetic and electric currents within a cell m are said to be dual if $L_m^{\mathrm{M}} = L_m^{\mathrm{J}}$, and the matrix

$$\int_{\Gamma_m} \left(\hat{\boldsymbol{n}} \times \boldsymbol{c}_{mi}^{\mathrm{M}}(\boldsymbol{r})\right) \cdot \boldsymbol{c}_{mj}^{\mathrm{J}}(\boldsymbol{r}) d\boldsymbol{r} \tag{3.26}$$

is diagonal with positive diagonals. To determine CBFs satisfying this duality, we

compute the Gram matrix $\mathbf{G}'_m$ defined by

$$\mathbf{G}'_m = \left(\mathbf{J}^{\mathrm{M}}_m\right)^H \mathbf{G}_m \mathbf{J}^{\mathrm{J}}_m \in \mathbb{C}^{s\times s}, \tag{3.27}$$

where $\mathbf{G}_m \in \mathbb{C}^{N_m \times N_m}$ is the Gram matrix of the RWG functions $\boldsymbol{f}_i$ contained in cell m:

$$\left[\mathbf{G}_m\right]_{ij} = \int_{\Gamma_m} \left(\hat{\boldsymbol{n}} \times \boldsymbol{f}_{\Lambda_{mi}}(\boldsymbol{r})\right) \cdot \boldsymbol{f}_{\Lambda_{mj}}(\boldsymbol{r})\, d\boldsymbol{r}. \tag{3.28}$$

We orthogonalize CBFs by applying the SVD to the Gram matrix $\mathbf{G}'_m$ and cutting off singular vectors associated with small singular values as follows:

$$\begin{aligned}
\mathbf{G}'_m &= \left(\mathbf{J}^{\mathrm{M}}_m\right)^H \mathbf{G}_m \mathbf{J}^{\mathrm{J}}_m \\
&= \begin{bmatrix}\mathbf{U}_{\mathrm{L}} & \mathbf{U}_{\mathrm{S}}\end{bmatrix} \begin{bmatrix}\boldsymbol{\Sigma}_{\mathrm{L}} & \\ & \boldsymbol{\Sigma}_{\mathrm{S}}\end{bmatrix} \begin{bmatrix}\mathbf{V}^H_{\mathrm{L}} \\ \mathbf{V}^H_{\mathrm{S}}\end{bmatrix} \\
&= \mathbf{U}_{\mathrm{L}}\boldsymbol{\Sigma}_{\mathrm{L}}\mathbf{V}^H_{\mathrm{L}} + \mathbf{U}_{\mathrm{S}}\boldsymbol{\Sigma}_{\mathrm{S}}\mathbf{V}^H_{\mathrm{S}} \\
&\simeq \mathbf{U}_{\mathrm{L}}\boldsymbol{\Sigma}_{\mathrm{L}}\mathbf{V}^H_{\mathrm{L}} \in \mathbb{C}^{s\times s} \left(\boldsymbol{\Sigma}_{\mathrm{L}} \in \mathbb{C}^{L_m \times L_m}\right),
\end{aligned} \tag{3.29}$$

where L_m is the number of singular values whose ratio to the largest singular value is greater than or equal to the threshold value δ_{SVD}. The size of both of the matrices $\mathbf{U}_{\mathrm{L}}$ and $\mathbf{V}_{\mathrm{L}}$ is thus $s \times L_m$. The CBFs $\mathbf{C}^{\mathrm{M}}_m$ and $\mathbf{C}^{\mathrm{J}}_m$ corresponding to the electric and magnetic currents are now obtained by

$$\mathbf{C}^{\mathrm{M}}_m = \mathbf{J}^{\mathrm{M}}_m \mathbf{U}_{\mathrm{L}} \in \mathbb{C}^{N^{\mathrm{M}}_m \times L_m} \tag{3.30}$$

$$\mathbf{C}^{\mathrm{J}}_m = \mathbf{J}^{\mathrm{J}}_m \mathbf{V}_{\mathrm{L}} \in \mathbb{C}^{N^{\mathrm{J}}_m \times L_m}. \tag{3.31}$$

It is easy to see that the CBFs thus obtained satisfy the duality in (3.26). Indeed, the matrix in (3.26) is computed as

$$\begin{aligned}
\left(\mathbf{C}^{\mathrm{M}}_m\right)^H \mathbf{G}_m \mathbf{C}^{\mathrm{J}}_m &= \left(\mathbf{J}^{\mathrm{M}}_m \mathbf{U}_{\mathrm{L}}\right)^H \mathbf{G}_m \mathbf{J}^{\mathrm{J}}_m \mathbf{V}_{\mathrm{L}} \\
&= \left(\mathbf{U}_{\mathrm{L}}\right)^H \left(\mathbf{J}^{\mathrm{M}}_m\right)^H \mathbf{G}_m \mathbf{J}^{\mathrm{J}}_m \mathbf{V}_{\mathrm{L}} \\
&= \boldsymbol{\Sigma}_{\mathrm{L}}
\end{aligned} \tag{3.32}$$

which is diagonal and with positive diagonals.

The number of CBFs in the cell m, denoted by N^{CBF}_m, is $L^{\mathrm{M}}_m + L^{\mathrm{J}}_m = 2L_m$; therefore, the total number of CBFs, denoted by N^{CBF}, is $2\sum_{m=1}^{N^{\mathrm{Cell}}} L_m$. In this way we obtain CBFs with the use of coefficient sets $\mathbf{C}^{\mathrm{M}}_m$ and $\mathbf{C}^{\mathrm{J}}_m$, which are mutually dual.

3.3.3 Matrix equation for the CBFM

With the dual CBFs obtained in the last section, we apply the KCP introduced in (3.20). For simplicity of explanation, we assume that elements associated with the RWG functions of smaller indices are in cells with smaller indices in order. This condition does not have to be satisfied in the actual implementation, though. We consider two sparse matrices $\mathbf{C}^{\mathrm{JM}} \in \mathbb{C}^{N \times N^{\mathrm{CBF}}}$ and $\mathbf{C}^{\mathrm{MJ}} \in \mathbb{C}^{N \times N^{\mathrm{CBF}}}$ defined as follows:

$$\mathbf{C}^{\mathrm{JM}} \equiv \begin{bmatrix} \mathbf{C}_1^{\mathrm{J}} & & & & & \\ & \ddots & & & & \\ & & \mathbf{C}_{N^{\mathrm{Cell}}}^{\mathrm{J}} & & & \\ & & & \mathbf{C}_1^{\mathrm{M}} & & \\ & & & & \ddots & \\ & & & & & \mathbf{C}_{N^{\mathrm{Cell}}}^{\mathrm{M}} \end{bmatrix}, \tag{3.33}$$

$$\mathbf{C}^{\mathrm{MJ}} \equiv \begin{bmatrix} \mathbf{C}_1^{\mathrm{M}} & & & & & \\ & \ddots & & & & \\ & & \mathbf{C}_{N^{\mathrm{Cell}}}^{\mathrm{M}} & & & \\ & & & \mathbf{C}_1^{\mathrm{J}} & & \\ & & & & \ddots & \\ & & & & & \mathbf{C}_{N^{\mathrm{Cell}}}^{\mathrm{J}} \end{bmatrix}. \tag{3.34}$$

By using (3.33) and (3.34) we obtain the right preconditioner $\mathbf{G}^{\mathrm{CBF}}$, which corresponds to the preconditioner $\mathbf{G}_{gffg}$ in (3.20) with the RWG and BC functions replaced with the dual CBFs, given by

$$\mathbf{G}^{\mathrm{CBF}} = \left(\mathbf{C}^{\mathrm{JM}}\right)^H \mathbf{G}_{ffff} \mathbf{C}^{\mathrm{MJ}} \in \mathbb{C}^{N^{\mathrm{CBF}} \times N^{\mathrm{CBF}}}. \tag{3.35}$$

Note that the matrix $\mathbf{G}^{\mathrm{CBF}}$ is diagonal if no connected boundary is divided into multiple cells in the CBFM. This is because the Gram matrix $\mathbf{G}^{\mathrm{CBF}}$ is block diagonal and each block corresponds to the Gram matrix in (3.28). Similarly, the CBF counterpart of the impedance matrix $\mathbf{Z}_{gffg}$ in (3.20) is given by $\left(\mathbf{C}^{\mathrm{JM}}\right)^H \mathbf{Z}_{ffff} \mathbf{C}^{\mathrm{MJ}}$. Using above equations and the dual CBF, we can write (3.20) and (3.21) as

$$\left[\left(\mathbf{C}^{\mathrm{JM}}\right)^H \mathbf{Z}_{ffff} \mathbf{C}^{\mathrm{MJ}}\right] \left(\mathbf{G}^{\mathrm{CBF}}\right)^{-1} \mathbf{y}^{\mathrm{CBF}} = \left(\mathbf{C}^{\mathrm{JM}}\right)^H \mathbf{v}_{ff}, \tag{3.36}$$

$$\mathbf{G}^{\mathrm{CBF}} \mathbf{j}^{\mathrm{CBF}} = \mathbf{y}^{\mathrm{CBF}}. \tag{3.37}$$

Finally, the expansion coefficient vector $\mathbf{j}$ in (3.14) is obtained from the solution $\mathbf{j}^{\mathrm{CBF}}$ as follows:

$$\mathbf{j} = \mathbf{C}^{\mathrm{MJ}} \mathbf{j}^{\mathrm{CBF}}, \tag{3.38}$$

and the electric and magnetic currents can be calculated with (3.7) and (3.8). Note that the matrix products in (3.36) and (3.37) can be computed efficiently since $\mathbf{C}^{\mathrm{MJ}}$, $\mathbf{C}^{\mathrm{JM}}$ are sparse, $\mathbf{G}^{\mathrm{CBF}}$ is (almost) diagonal and the matrix-vector product with $\mathbf{Z}_{ffff}$ can be accelerated by fast methods such as the FMM [5]- [7]. (See 3.3.4 for an estimate of the computational complexity). Consequently the proposed method is expected to have good properties in terms of both convergence and computational cost.

From another perspective, the proposed method has an advantage that one can easily implement it by adding a few components to an existing in-house MoM program. Indeed, the proposed method only needs to calculate $\mathbf{C}^{\mathrm{MJ}}$, $\mathbf{C}^{\mathrm{JM}}$ and $\mathbf{G}^{\mathrm{CBF}}$ anew and put them into the conventional iterative method as preconditioners, as is evident in (3.36) and (3.37).

3.3.4 Computational complexity

Finally, we discuss the computational complexity of the proposed method which uses primary CBFs. In the following calculations, we assume that s, N_m and N_m^{CBF} are $O(1)$ for simplicity. We first estimate the cost of constructing primary CBFs. In one cell, the costs of generating (3.24), the LU decomposition and solving this equation for s incident waves are $O\left(N_m^2\right)$, $O\left(N_m^3\right)$ and $O\left(sN_m^2\right)$, respectively. In addition, the generation of primary CBFs requires the computation of $\mathbf{G}_m$, $\mathbf{G}'_m$, SVD, and $\mathbf{C}_m^{\mathrm{M,J}}$ per cell, which are calculated with $O\left(N_m\right)$, $O\left(s^2N_m\right)$, $O\left(s^3\right)$, and $O\left(s^2N_m\right)$ operations, respectively. Since all these per-cell calculations are $O(1)$ operations, we estimate the computational complexity of precomputing for the calculation of (3.36) to be $O\left(N\right)$ since the number of cells is $O\left(N/N_m\right) = O(N)$.

We next estimate the complexity for one matrix-vector product in the left hand side (LHS) of (3.36), which is required in solving (3.36) using the Krylov subspace methods. To this end, we assume that the inversion in the LHS of (3.36) is carried out with less than a fixed number of GMRES iterations. This is a reasonable assumption because $\mathbf{G}^{\mathrm{CBF}}$ is regular and is even diagonal if no connected boundary is divided into multiple cells in the CBFM, as we have noted earlier. Since the complexity of computing the LHS of (3.37) is obviously $O(N)$, we conclude from the above assumption that the complexity for evaluating $\left(\mathbf{G}^{\mathrm{CBF}}\right)^{-1}\mathbf{y}^{\mathrm{CBF}}$ is $O(N)$. One readily shows that the multiplication of $\mathbf{C}^{\mathrm{JM}}$ and $\mathbf{C}^{\mathrm{MJ}}$ can also be carried out with $O(N)$ operations. Since the multiplication of $\mathbf{Z}_{ffff}$ can be carried out with $O\left(N\log N\right)$ operations with the FMM [5–7], we conclude that the largest complexity for one matrix-vector product operation in (3.36) is $O\left(N\log N\right)$. Since the number of GMRES iterations in solving (3.36) is small by the effect of using KCP, it can be regarded as a constant. Also the number of GMRES iterations in solving (3.37)

is less than a constant by assumption. We thus conclude that the complexity for solving the system in (3.36) and (3.37) is $O(N \log N)$.

The numerical results in the next section show that the computational overhead that the preconditioner comprises is surpassed by a reduction in the computational time achieved by the decreased number of iterations, although there might be a chance that the result is different for an intricate geometry.

3.4 Numerical results

In this section, we evaluate the validity of the proposed method by analyzing several scattering problems and comparing the results with those obtained with MoM. For a fair comparison with the proposed method, we use the PMCHWT formulation with the following commonly used operator arrangement to obtain reference MoM solutions:

$$\begin{aligned} \mathbf{Z}_{\mathrm{t}}\mathbf{D}^{-1}\tilde{\mathbf{j}}_{\mathrm{t}} &= \mathbf{v}, \\ \mathbf{j}_{\mathrm{t}} &= \mathbf{D}^{-1}\tilde{\mathbf{j}}_{\mathrm{t}}, \\ \mathbf{Z}_{\mathrm{t}} &= \sum_{i=1}^{2} \begin{bmatrix} -\eta_i \mathbf{T}_i^{ff} & \mathbf{K}_i^{ff} \\ \mathbf{K}_i^{ff} & \frac{1}{\eta_i}\mathbf{T}_i^{ff} \end{bmatrix}, \\ \mathbf{j}_{\mathrm{t}} &= \begin{bmatrix} \begin{bmatrix} \alpha_1^{\mathrm{J}} & \cdots & \alpha_{N^{\mathrm{J}}}^{\mathrm{J}} \end{bmatrix} & \begin{bmatrix} \alpha_1^{\mathrm{M}} & \cdots & \alpha_{N^{\mathrm{M}}}^{\mathrm{M}} \end{bmatrix} \end{bmatrix}^T, \end{aligned} \tag{3.39}$$

where $\mathbf{D}$ is the diagonal preconditioner. This arrangement of the operators appears to be more natural than the proposed method in (3.12) since the matrix $\mathbf{T}_i$ has large diagonal elements while $\mathbf{K}_i$ corresponds to a discretized compact operator which has smaller diagonal elements. The numerical results referred to as "MoM" corresponds to solutions obtained with (3.39). We use the FMM for the multiplication of the impedance matrix and the GMRES without restart [4] for solving linear equations. The initial guess for the GMRES is set to $\mathbf{0}$. The error tolerance δ_{R} for the residual norm, which determines the convergence of the outer iterations, is specified in each problem. We use the LU decomposition for solving (3.24) to obtain the primary CBFs because the number of unknowns in a single cell is small and because it can deal with multiple incident fields easily. The condition numbers shown in the rest of this thesis are with respect to the 2-norm. This value is defined as the ratio of the maximum singular value to the minimum singular value obtained by the SVD of the impedance matrix under consideration. All the computations were carried out using "Laurel2" supercomputer system at Kyoto university with 2.1GHz Intel Xeon CPU E5-2695 v4 processor.

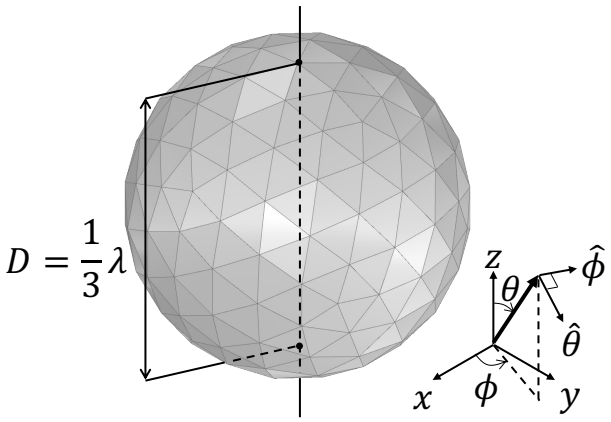

Figure 3.3: Sphere

Table 3.1: Parameters for calculating CBFs for sphere array

θ_s	$\Delta\theta$	N_θ	ϕ_s	$\Delta\phi$	N_ϕ	Pol.	Cell (λ)
0°	30°	12	0°	30°	6	$\hat{\theta}, \hat{\phi}$	1/2

3.4.1 Sphere array

Single sphere

The first example is a sphere of diameter $\lambda/3$ as shown in Fig. 3.3, whose relative permittivity ϵ_r is varied from 1.0 to 6.0. The number of unknowns N is 960. When $\theta = \phi = 0°$, the $\hat{\theta}$–polarization is defined to be in the x direction and the $\hat{\phi}$–polarization in the y direction. In subsequent analyses, we often consider the incident fields of $\hat{\theta}$–polarized waves propagating toward the $-z$ direction. The angle in this direction is $\theta = 180°$, $\phi = 0°$, and the direction of the $\hat{\theta}$–polarized wave corresponds to the $-x$ direction. TABLE 3.1 shows parameters for the incident fields used for calculating CBFs. We generate CBFs by solving (3.24) with the incident plane waves propagating in the directions given by the spherical coordinates

$$(\theta, \phi) = (\theta_s + n_\theta \Delta\theta, \phi_s + n_\phi \Delta\phi), \quad \text{for} \quad n_\theta = 0, \ldots, N_\theta \quad n_\phi = 0, \ldots, N_\phi. \tag{3.40}$$

The directions of polarization are defined accordingly, taking $\phi = 0$ for $\theta = 0$ and π. In this analysis, we consider one single cell which includes the entire sphere, thus not dividing the scatterer into cells. An analysis of this type may not be of much practical interest, but helps us to understand the characteristics of the CBFM, as we will see.

Fig. 3.4 shows the distribution of singular values in (3.29). In this figure, the horizontal axis shows the number of singular values assigned in descending order of

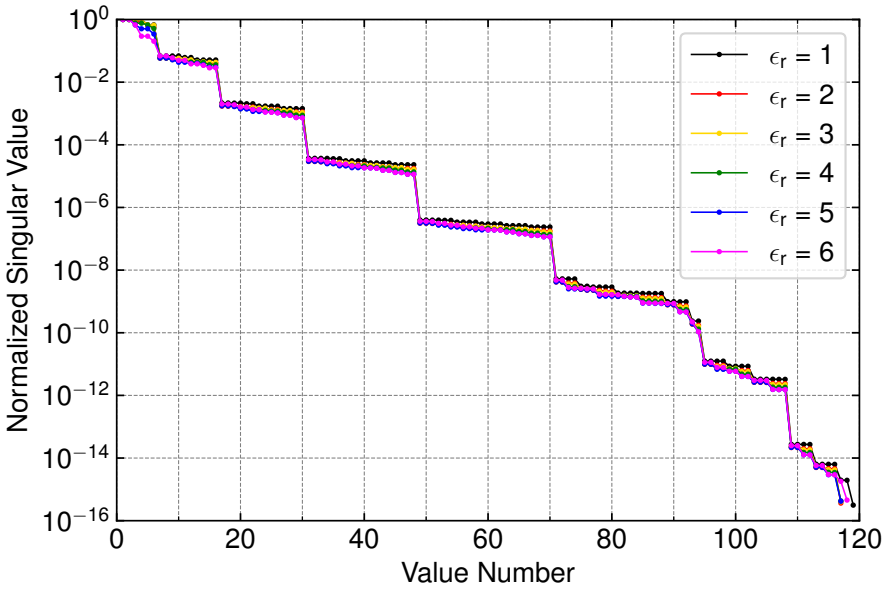

Figure 3.4: Normalized singular value of the sphere

the magnitudes, and the vertical axis shows the magnitude of each singular value normalized by their maximum value. We see that these singular values are divided into several groups regardless of the dielectric constant. Numbering these groups from left to right as $l(=1,2,\cdots)$, we see that the number of singular values belonging to the lth group is $2(2l+1)$ which is the dimension of the vector spherical harmonics of the lth-order. Motivated by this observation, we first consider up to 70 singular values belonging to the group of $l=1,\cdots,5$. Since 70 CBFs are defined for both electric and magnetic currents, we have $N^{\mathrm{CBF}}=140$. The proposed method is intended to orthogonalize the electric and magnetic CBFs as described in section 3.3.2. To check this, we compute CBFs at the barycentric coordinate of each triangle in a cell represented by (3.23). Fig. 3.5 shows the real and imaginary parts of CBFs for electric and magnetic currents. Fig. 3.5a (Fig. 3.5c) gives the CBF distributions corresponding to the largest (smallest) singular value for $\epsilon_{\mathrm{r}}=1$. It is seen, indeed, that the electric and the corresponding magnetic CBFs are mutually orthogonal even up to the 70th ones.

Fig. 3.6 shows the convergence, accuracy, and the condition number for the incident field propagating in $-z$ direction. In Fig. 3.6 and in other figures as well, "w/ KCP" shows the results where KCP (i.e. a preconditioner with $\mathbf{G}^{\mathrm{CBF}}$) is applied to CBFM according to (3.36) and (3.37). The legend "w/o KCP" indicates results obtained with the following equation:

$$\left(\mathbf{C}^{\mathrm{JM}}\right)^{H}\mathbf{Z}_{ffff}\mathbf{C}^{\mathrm{MJ}}\mathbf{j}^{\mathrm{CBF}}=\left(\mathbf{C}^{\mathrm{JM}}\right)^{H}\mathbf{v}_{ff}, \tag{3.41}$$

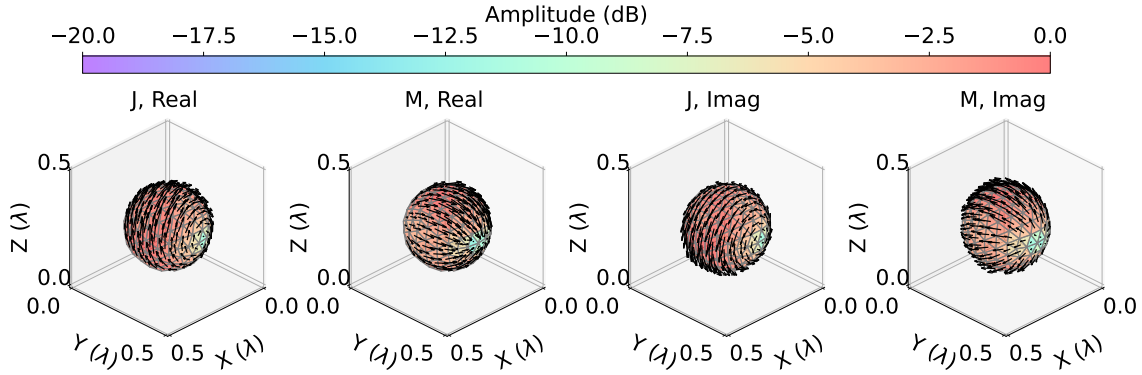

(a) CBF for singular value #1

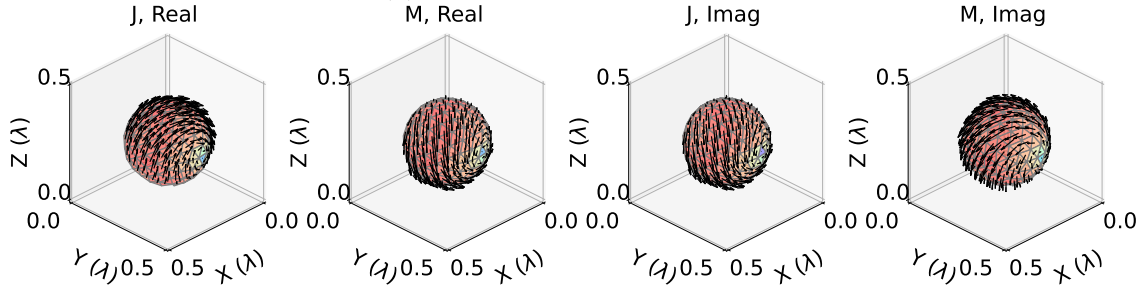

(b) CBF for singular value #2

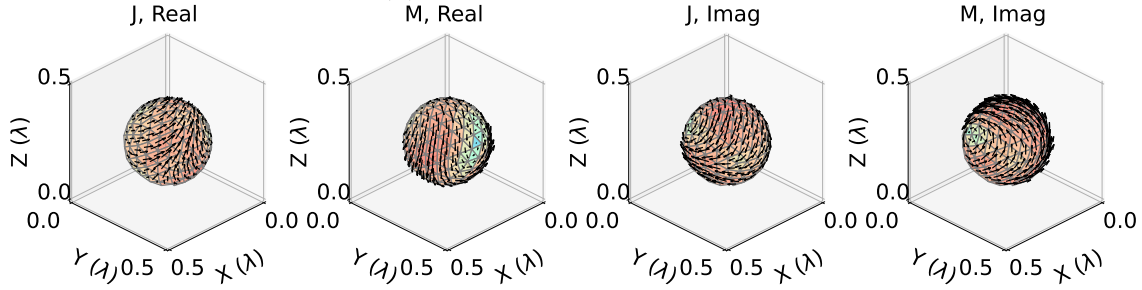

(c) CBF for singular value #70

Figure 3.5: CBF distributions on a sphere for $\epsilon_r = 1$. Black arrows in each figure represent current directions at the center of each mesh. $\#i$ corresponds to the singular value number. The two figures on the left show the real parts of the CBFs for the electric and magnetic currents, and the two right figures show their imaginary parts.

which is a formulation without KCP in (3.36). Also, the numbers enclosed in brackets in the legends represent equation numbers. Fig. 3.6a clearly shows that the convergence of the proposed method is much improved compared to the MoM results. In Fig. 3.6b, we evaluate the accuracy of the analysis using the following

indicators

$$\frac{\left(\sum_{i=1}^{P}\left(|\boldsymbol{J}^{\mathrm{m}}(\boldsymbol{r}_i)-\boldsymbol{J}^{\mathrm{c}}(\boldsymbol{r}_i)|^2+|\boldsymbol{M}^{\mathrm{m}}(\boldsymbol{r}_i)-\boldsymbol{M}^{\mathrm{c}}(\boldsymbol{r}_i)|^2\right)\right)^{1/2}}{\left(\sum_{i=1}^{P}\left(|\boldsymbol{J}^{\mathrm{m}}(\boldsymbol{r}_i)|^2+|\boldsymbol{M}^{\mathrm{m}}(\boldsymbol{r}_i)|^2\right)\right)^{1/2}},$$

where $\boldsymbol{r}_i$ is the center coordinate of mesh i, P is the number of meshes for the scatterer, and the superscripts "m" (MoM) and "c" (CBFM) denote the method of analysis used to obtain $\boldsymbol{J}$ and $\boldsymbol{M}$. This figure shows that the accuracy of the CBFM remains the same with or without KCP. Fig. 3.6b also shows that the use of KCP makes the condition number smaller. These results indicate that the proposed KCP can improve convergence without changing the accuracy of the solution compared to the method without KCP.

Next we consider the relationship between mesh size of the scatterer and accuracy. We calculate the currents by using the proposed method with KCP, without KCP and the conventional MoM with four different mesh sizes having 240, 960, 3840, and 15360 unknowns. The diameter of the sphere is $\lambda/3$, and the incident field propagates in $-z$ direction. The relative permittivity ϵ_{r} is set to 3. The residual norm δ_{R} in each analysis is set to 10^{-10} in order to clarify the relationship between the accuracy of the CBFs and the group number l with which the number of CBFs is determined. The values of l between 3 and 6 are considered. To be consistent with the small value of δ_{R}, we refined the angular spacings $\Delta\theta$ and $\Delta\phi$ to be $10°(N_\theta = 36, N_\phi = 18)$ instead of 30° used for the CBF generation in Fig. 3.4 (see TABLE 3.1). This is in order to prevent from possible inaccuracy caused by insufficient numbers of incident waves since the variation of the singular values for $l = 6$ (71st to 96th singular values) in Fig. 3.4 appears to be larger than those for smaller ls. The other parameters are the same as those in TABLE 3.1. Fig. 3.7 shows the number of iterations vs the average mesh size h. As h decreases, the number of iterations of the MoM increases. With the CBFMs, N^{CBF} remains constant as long as the group number l is unchanged, even if the scatterers are densely discretized. Although there appears to be a slight increase in iteration numbers when the mesh size is taken to be the smallest, the increment is just 2 which is possible but insignificant considering the very small residual norm and is negligible compared to the results without KCP. Therefore, we conclude that the number of iterations for the proposed method without KCP is independent of the mesh size h for the same l, and increases with l. When the KCP is applied to the proposed method, the number of iterations is almost constant regardless of l unless the mesh size is large. This means that the KCP resolves the dense discretization breakdown; one may make the mesh size small for higher accuracy without worrying about the increased number of iterations.

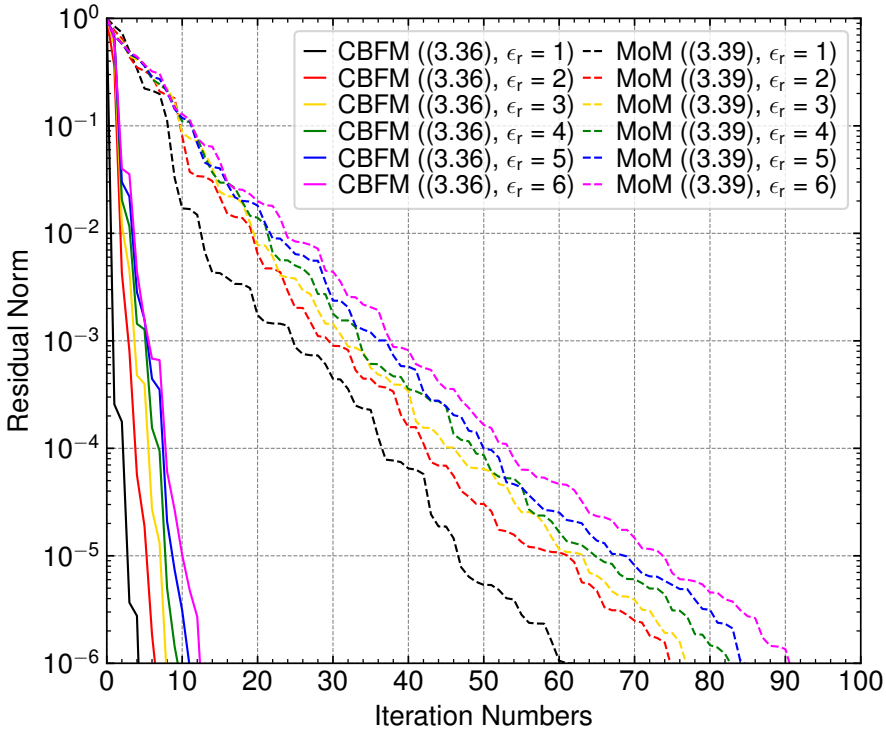

(a) Convergence

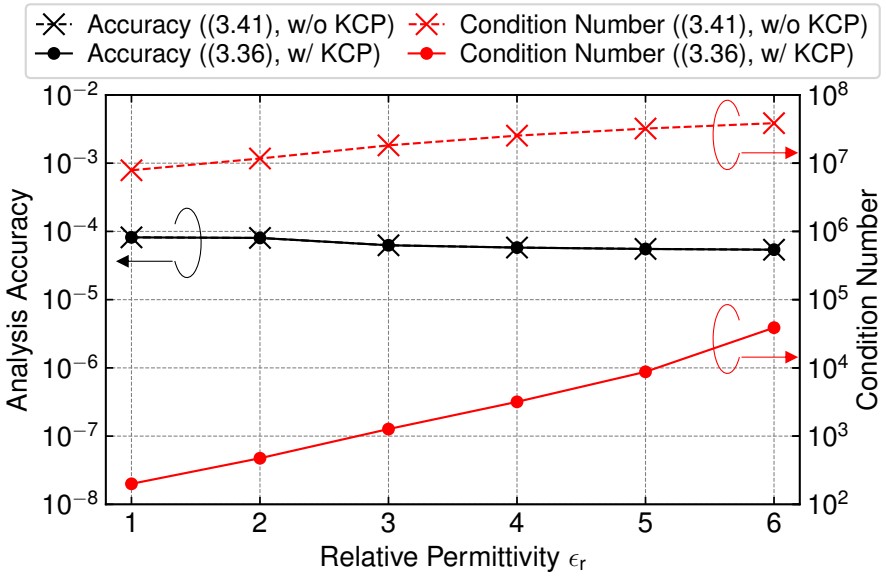

(b) Accuracy and condition number

Figure 3.6: Convergence and accuracy for a sphere. The incident field propagates in $-z$ direction

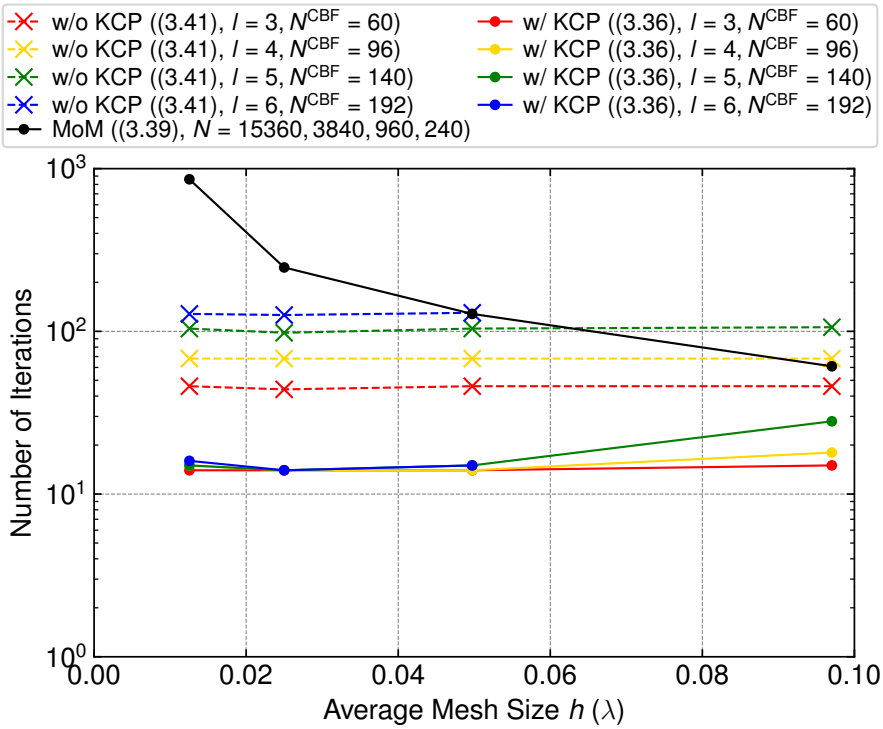

Figure 3.7: Relationship between mesh size. For the largest average mesh size h, the calculation is limited to $l = 5$ because the rank order of the Gram matrix $\mathbf{G}_m$ is smaller than the number of singular values up to $l = 6$.

Sphere array

Next, we analyze an array-shaped scatterer composed of spheres of the above mentioned shape aligned $4 \times 4 \times 2$ in the x, y, and z directions as shown in Fig. 3.8. The number of the unknowns N is 30720. The conditions of the incident field and the number of singular values considered for the generation of CBFs are the same as those in the case of a single sphere. In the previous analysis for a single sphere, the number of CBFs per cell was 140; therefore N^{CBF} is 4480 in this analysis. The number of unknowns will be reduced by a factor of about 6.9 compared to the MoM.

We first compare the convergence of the outer GMRES for three methods, i.e., the proposed method in (3.36), the proposed CBFM without using $\mathbf{G}^{\mathrm{CBF}}$, and the CBFM with the matrix arranged as in (3.39), i.e.

$$\left[\left(\mathbf{C}^{\mathrm{JM}}\right)^H \mathbf{Z}_{\mathrm{t}} \mathbf{C}^{\mathrm{JM}}\right] \mathbf{j}_{\mathrm{t}}^{\mathrm{CBF}} = \left(\mathbf{C}^{\mathrm{JM}}\right)^H \mathbf{v} \qquad (3.42)$$
$$\mathbf{j}_{\mathrm{t}} = \mathbf{C}^{\mathrm{JM}} \mathbf{j}_{\mathrm{t}}^{\mathrm{CBF}}.$$

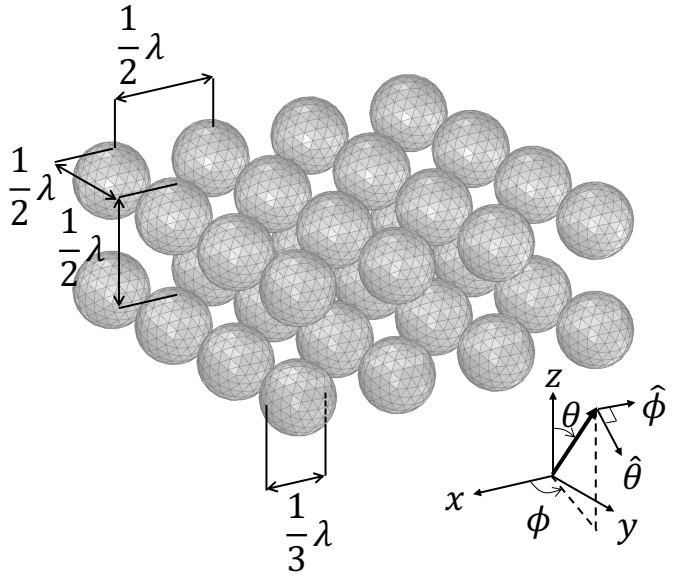

Figure 3.8: $4 \times 4 \times 2$ sphere array

For solving (3.42), we do not use the right preconditioner $\mathbf{G}^{\mathrm{CBF}}$ in (3.36) since this preconditioner is effective only when the $\mathbf{K}_i$-components are arranged diagonally as shown in (3.20).

Fig. 3.9 shows the convergence of each method under the conditions that the incident plane wave propagates in $-z$ direction with $\hat{\theta}$-polarization and $\epsilon_{\mathrm{r}} = 3$. In Fig. 3.9, "w/o KCP, $\mathcal{T}$", "w/o KCP, $\mathcal{K}$" and "w/ KCP, $\mathcal{K}$" indicate the results of the analyses using (3.42) and (3.36) with and without the preconditioner matrix $\mathbf{G}^{\mathrm{CBF}}$, respectively. In the analyses without the KCP, the residual norm δ_{R} did not reach 10^{-6} even after 1000 iterations. On the other hand, the proposed method with $\mathbf{G}^{\mathrm{CBF}}$ clearly improved the convergence since δ_{R} reached 10^{-6} in less than 40 iterations.

Fig. 3.10 compares the RCS patterns obtained with the proposed method and MoM, respectively, for $\epsilon_{\mathrm{r}} = 3$. The RMSE of the CBFM relative to the MoM defined by

$$\mathrm{RMSE} = 10 \log_{10} \left(\frac{\sqrt{\frac{1}{N_\theta} \sum_{i=1}^{N_\theta} \left(\sigma_i^{\mathrm{c}} - \sigma_i^{\mathrm{m}}\right)^2}}{\max\limits_i \{\sigma_i^{\mathrm{m}}\} - \min\limits_i \{\sigma_i^{\mathrm{m}}\}} \right) \quad \mathrm{dB}$$

is -39.98 dB, where σ_i^{c} and σ_i^{m} indicate the RCSs obtained with the CBFM and MoM in the i–th calculation, respectively. These results agree quite well.

Next, we check the convergence in the same scattering problem for variable relative permittivity ϵ_{r}. The threshold of δ_{R} is set to be 10^{-4}, which the two methods without KCP could reach in Fig. 3.9. Fig. 3.11 shows the convergence properties and condition numbers vs ϵ_{r}. The $\mathbf{K}$-diagonal CBFM with KCP could reduce the number

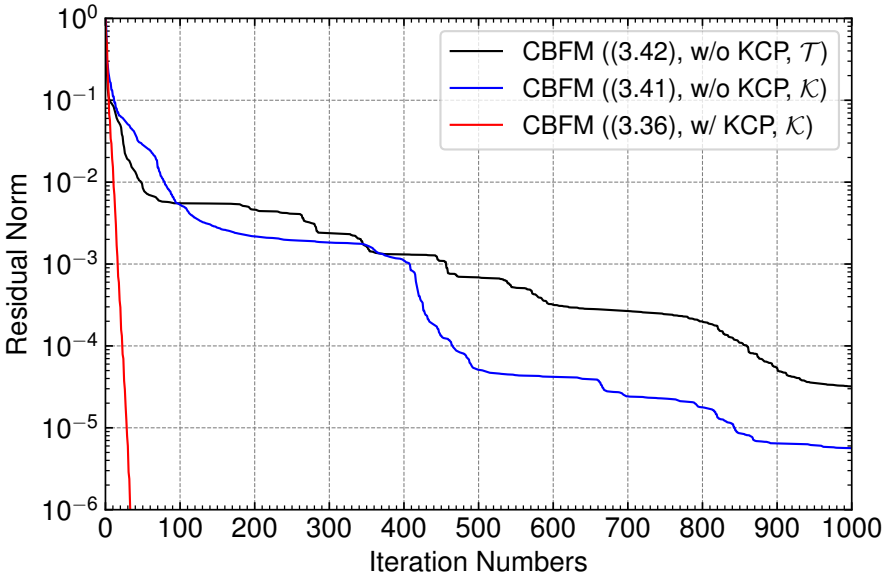

Figure 3.9: Convergence of the sphere array analysis for the incident field with $\hat{\theta}$–polarization and $-z$ propagation direction.

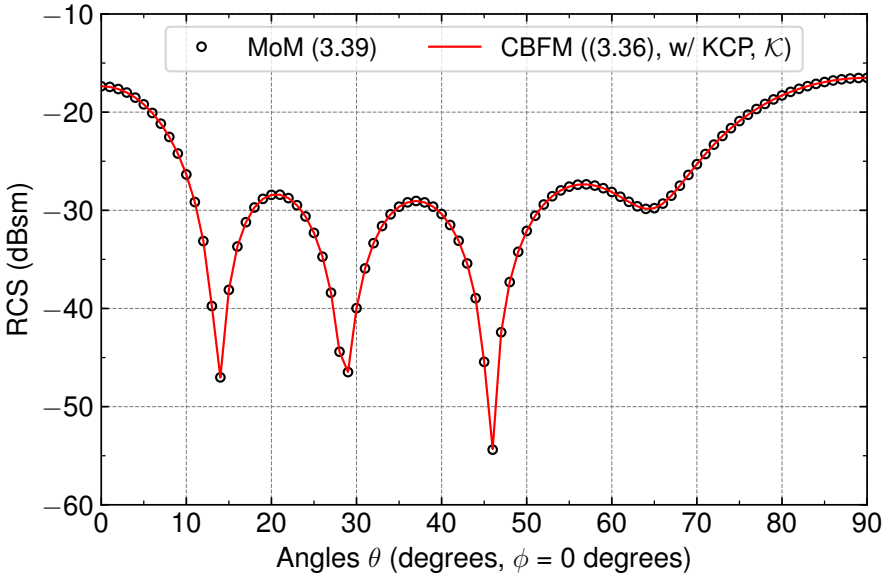

Figure 3.10: RCS of the sphere array $(4 \times 4 \times 2)$ at $\epsilon_{\mathrm{r}} = 3$

of iterations to $1/70 \sim 1/5$ compared to the corresponding **K**-diagonal one without KCP. The number of iterations differs between the **K**- and **T**-diagonal versions without KCP. On the other hand, their condition numbers are obviously identical because these impedance matrices are obtained from each other by interchanging columns.

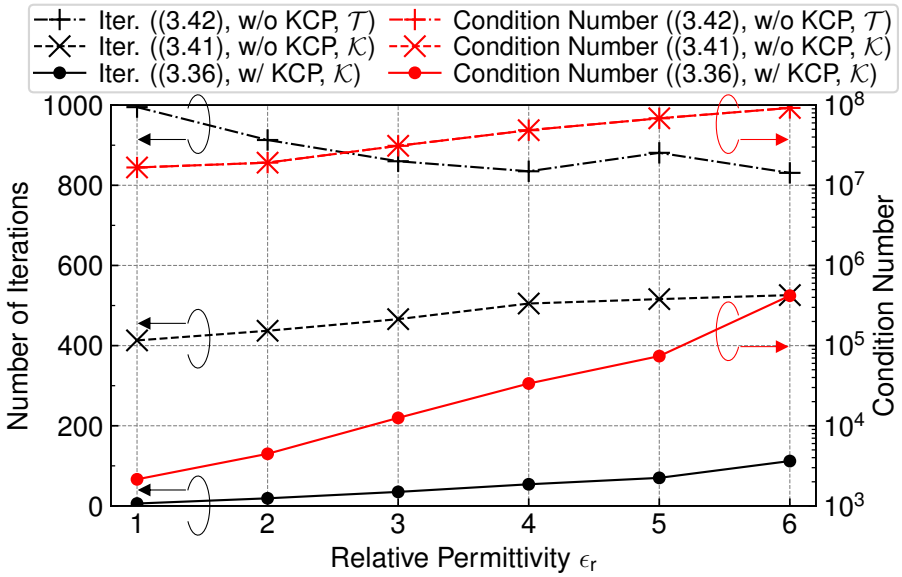

Figure 3.11: Relationship between the relative permittivity and the convergence of the scatterer

The difference of the convergence property among these three numerical methods can be better explained with eigenvalue distributions. Fig. 3.12 shows the distributions of eigenvalues of the impedance matrices for **T**-diagonal, **K**-diagonal without KCP and **K**-diagonal with KCP cases, i.e., $\left(\mathbf{C}^{\mathrm{JM}}\right)^{H}\mathbf{Z}_{\mathrm{t}}\mathbf{C}^{\mathrm{JM}}$, $\left(\mathbf{C}^{\mathrm{JM}}\right)^{H}\mathbf{Z}_{ffff}\mathbf{C}^{\mathrm{MJ}}$, and $\left(\mathbf{C}^{\mathrm{JM}}\right)^{H}\mathbf{Z}_{ffff}\mathbf{C}^{\mathrm{MJ}}\left(\mathbf{G}^{\mathrm{CBF}}\right)^{-1}$, respectively. In the former two cases, the magnitudes of eigenvalues are about as large as the area of the mesh element due to the effect of the CBF containing a Gram matrix as in (3.35). The distributions of these two cases are similar in that there exist large number of eigenvalues near zero, which explains the poor convergence. In the proposed KCP, however, the inverse of $\mathbf{G}^{\mathrm{CBF}}$ eliminates the near-zero eigenvalues and the entire eigenvalues are distributed around ± 1. This indicates that the condition number remains sufficiently small even if ϵ_{r} changes.

Finally, we consider a model of optical metamaterials composed of gold nanoparticles as an application of the proposed method. The configuration of the scatterer is the same as in Fig. 3.8, and the wavelength λ is 550 nm. The relative permittivity ϵ_{r} of gold at $\lambda = 550$ nm is $-5.8421 - j2.1113$ [52]. The threshold of δ_{R} is set to be 10^{-4}. Fig. 3.13 compares the RCS patterns obtained with the **K**-diagonal CBFM with KCP and the MoM. The RMSE of the patterns is -38.23 dB, which indicates that the proposed method can be used in practical problems.

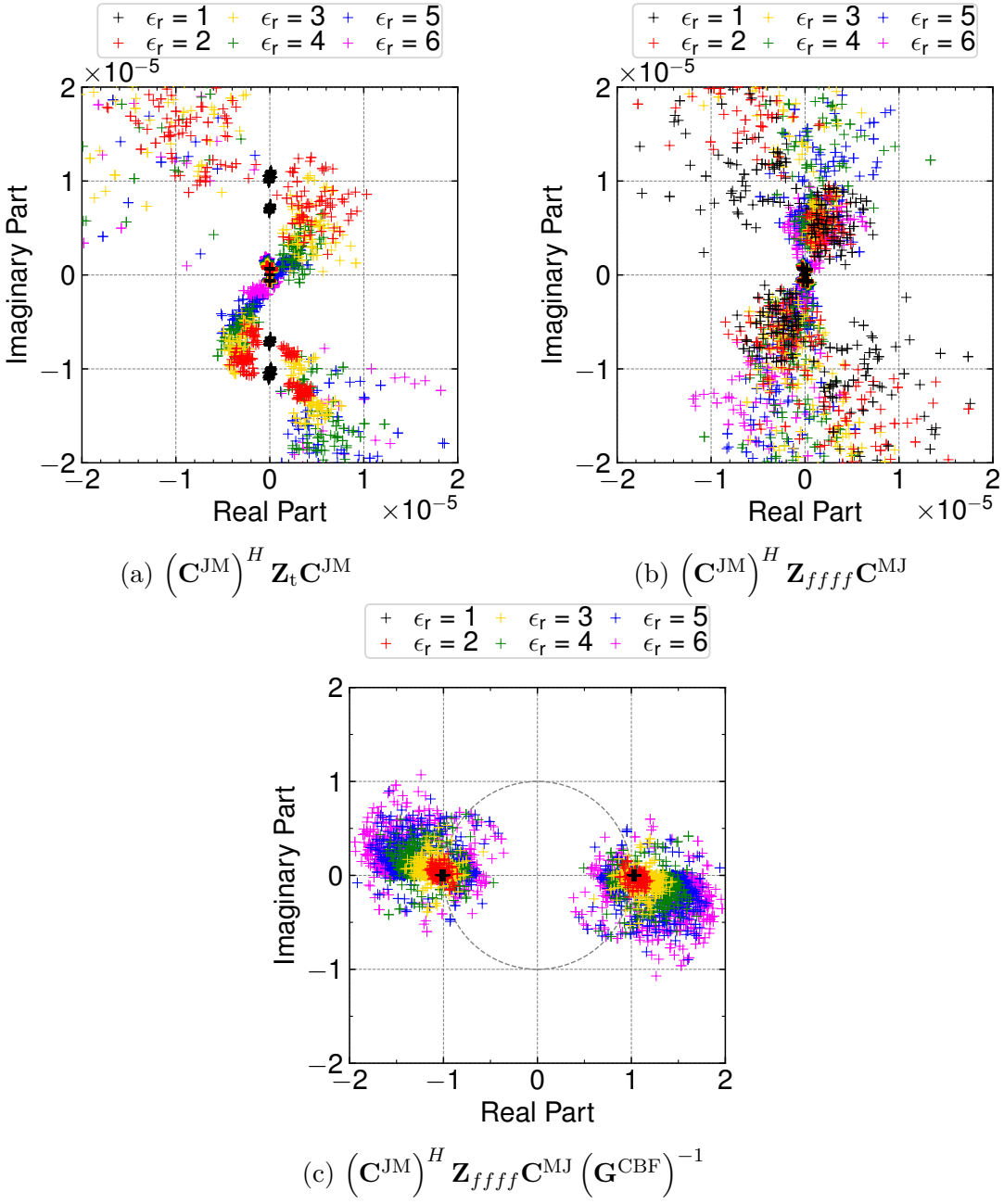

(a) $\left(\mathbf{C}^{\mathrm{JM}}\right)^{H} \mathbf{Z}_{\mathrm{t}} \mathbf{C}^{\mathrm{JM}}$

(b) $\left(\mathbf{C}^{\mathrm{JM}}\right)^{H} \mathbf{Z}_{ffff} \mathbf{C}^{\mathrm{MJ}}$

(c) $\left(\mathbf{C}^{\mathrm{JM}}\right)^{H} \mathbf{Z}_{ffff} \mathbf{C}^{\mathrm{MJ}} \left(\mathbf{G}^{\mathrm{CBF}}\right)^{-1}$

Figure 3.12: Eigenvalue distribution of sphere array

Large sphere array

As an example of a large-scale scattering analysis, we consider a sphere array consisting of 256 spheres ($8 \times 16 \times 2$ in the x, y, and z directions). The number of unknowns N is $960 \times 256 = 245760$. In this analysis, we use the same conditions and the relative permittivity ($\epsilon_{\mathrm{r}} = 3$) as in the $4 \times 4 \times 2$ array case, hence we have

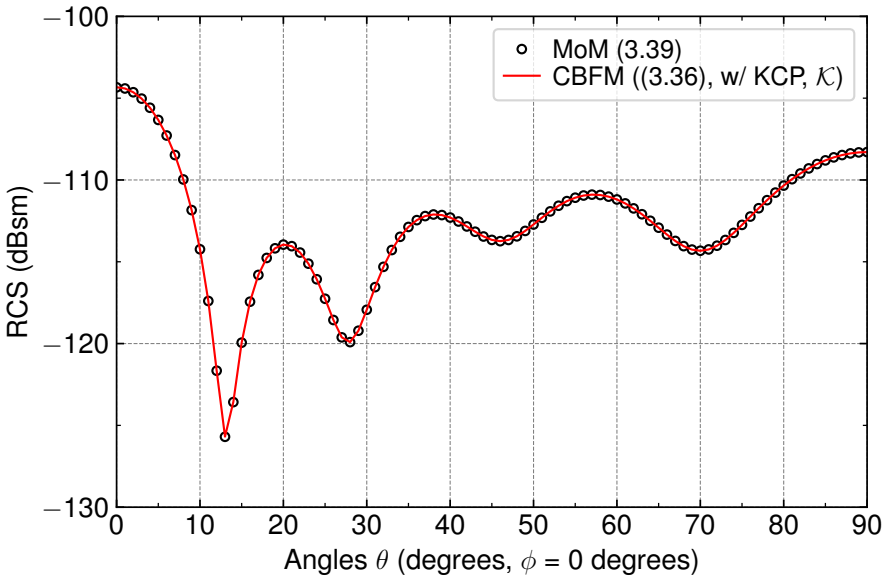

Figure 3.13: RCS of the gold sphere array

$N^{\mathrm{CBF}} = 35840$.

Fig. 3.14 shows the δ_{R} (residual norm) vs the number of iterations curves for the proposed method and MoM when the incident field is with the θ-polarization and propagates in $-z$ direction. In the proposed method, the number of iterations is 143 when the residual norm δ_{R} is 10^{-6}, while it is about 634 in the case of the MoM, which is about 4.4 times that of the proposed method.

Fig. 3.15 shows the RCS pattern obtained using $\delta_{\mathrm{R}} < 10^{-4}$ as the criterion of the convergence. The angle range and polarization to calculate the RCS pattern are $0^\circ \leq \theta \leq 90^\circ$, $\Delta\theta = 1^\circ$, $\phi = 0^\circ$ and $\hat{\theta}$. The RMSE is -35.65dB; hence the RCS obtained with the proposed CBFM is in good agreement with the MoM result. The computational times for generating the primary CBFs and final iteration, relative to the total computational time for the MoM for 91 directions, are less than 0.02 and approximately 0.21, respectively. Hence the proposed method is more than four times faster than the conventional method in this analysis. For reference, the total computational time for 91 directions using the MoM is approximately 358.6 hours. These results show that the proposed method is effective particularly for large scale scatterers.

3.4.2 Cube array

The next analysis object is a cube array as shown in Fig. 3.16. The cubes are aligned $8 \times 2 \times 2$ in the x, y, and z directions, respectively. The number of the unknowns

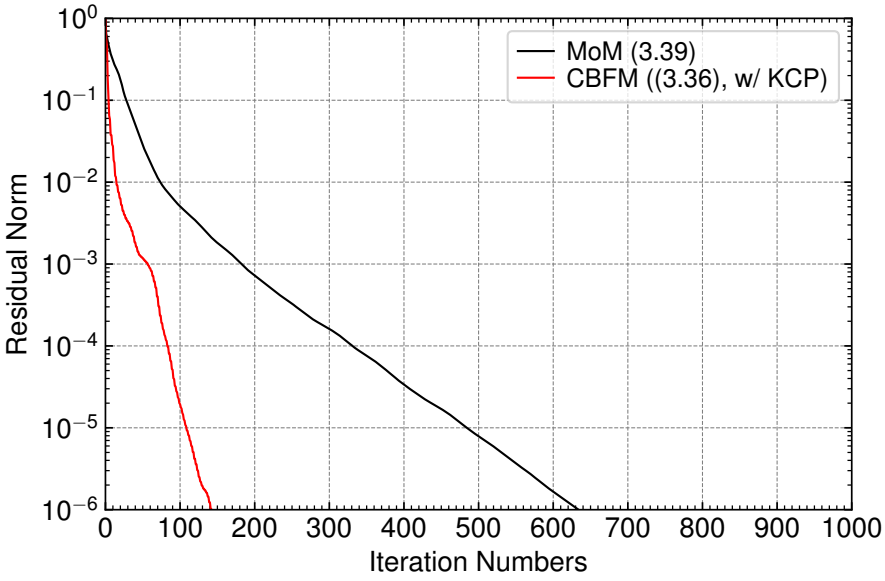

Figure 3.14: Convergence of the large sphere array analysis.

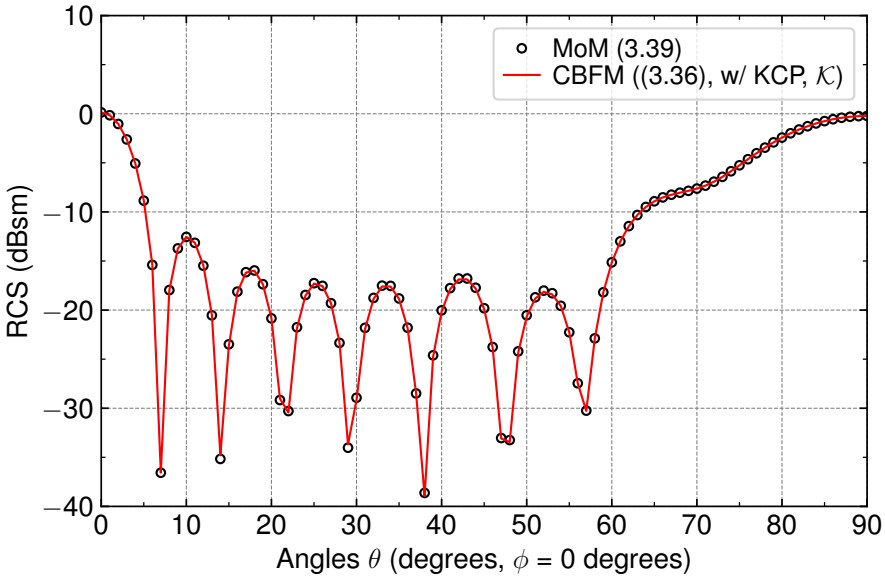

Figure 3.15: RCS of the large sphere array.

N is 41472 and the relative permittivity is assumed to be 3. The cell is set up as in the previous analysis, i.e., a cubic cell with a side length of $\lambda/2$ containing a cubic scatterer ($M = 32$). The number of singular values to be considered is determined from the group number l as mentioned in the previous section. In this analysis, we also consider the impacts of the angular intervals of the generating incident fields

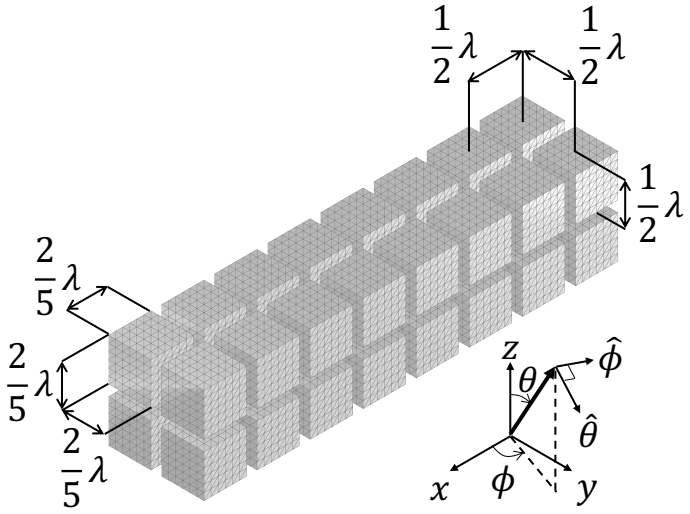

Figure 3.16: Cube array ($8 \times 2 \times 2$)

Table 3.2: Condition of CBFs for cube array

No.	θ_s	$\Delta\theta$	N_θ	ϕ_s	$\Delta\phi$	N_ϕ	Pol.	Group number l
3.2-1	0°	30°	12	0°	30°	6	$\hat{\theta}, \hat{\phi}$	4
3.2-2	0°	30°	12	0°	30°	6	$\hat{\theta}, \hat{\phi}$	5
3.2-3	0°	30°	12	0°	30°	6	$\hat{\theta}, \hat{\phi}$	6
3.2-4	0°	10°	36	0°	10°	18	$\hat{\theta}, \hat{\phi}$	4
3.2-5	0°	10°	36	0°	10°	18	$\hat{\theta}, \hat{\phi}$	5
3.2-6	0°	10°	36	0°	10°	18	$\hat{\theta}, \hat{\phi}$	6

and the threshold of the singular value on the accuracy and convergence of CBFM. The KCP in (3.36) is used for all analyses. The primary CBFs are generated with plane waves, which propagate in the directions given by the spherical coordinates in (3.40) with the parameters in TABLE 3.2.

Fig. 3.17 shows the distribution of singular values in (3.29) for a single cube. In Fig. 3.17 "No.3.2-i" corresponds to the number of conditions in TABLE 3.2. (We use similar notations in the appendix A.) Note that these singular values are the same for all cells because the incident fields on each cell are identical except for the phase factor. In this figure we can identify a few groups of singular values, although not as clearly as in the case of the sphere. We see that the numbers of singular values in groups with small ls are the same as those in the corresponding sphere case (See Fig. 3.4). Also, the singular values of groups with larger l can be calculated more accurately with smaller incident angle intervals. Fig. 3.18 shows the real and imaginary parts of CBFs represented by (3.23) at the barycentric coordinate of each

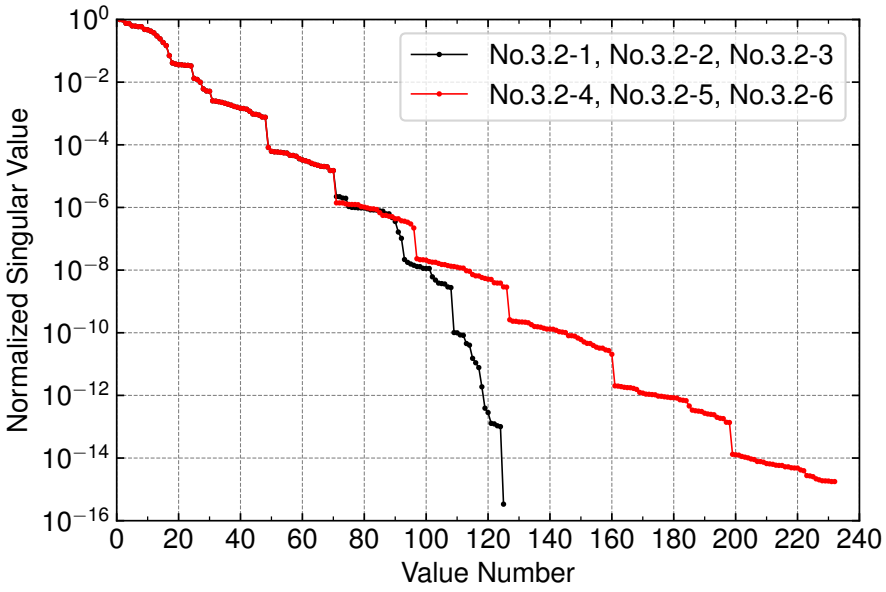

Figure 3.17: Normalized singular value of the cube.

triangle in a cell for the cube array under condition 3.2-6 ($l = 6$) in TABLE 3.2. The orthogonality between electric and magnetic CBFs is visible even with the CBF No. 96, which is the maximum number of CBFs to be considered with $l = 6$.

The relationship between the choice of CBF parameters, accuracy, and convergence can be interpreted as follows. First, we consider the relationship between the angular interval of the incident fields and accuracy. In this problem, the electric length corresponding to the circumference of the circumscribing sphere for a cube is $2\pi r\sqrt{\epsilon_r} \simeq 3.8\lambda$, where $r = \sqrt{3}\lambda/5$. Therefore, approximately 3.8 cycles of electromagnetic currents could be generated on the surface of the fictitious circumscribing sphere, which tells that one may need at least $l \approx 4$ for an accurate resolution of the solution. On the other hand, the spacing of the incident field may roughly correspond to the sampling interval of the electromagnetic current generated on the surface. This indicates that only 3 points are sampled per cycle for the $l = 4$ variation when the incident field interval is set to 30°. When the incident field interval is set to 10°, however, the number of sampling points per cycle for $l = 4$ is raised to 9 which is more reasonable. Next, we consider the relationship between the convergence of CBFM and the appropriate group number l to be considered for CBFs. It is expected that the current distribution on a cube will be more complicated than that on a sphere due to corners and edges. This indicates that more CBFs are needed to represent complex currents on a cube than those determined by $l = 4$. From this consideration, we conclude that taking CBFs corresponding to l greater than 5 or 6 will be desired in this problem. The validity of this consideration is demonstrated

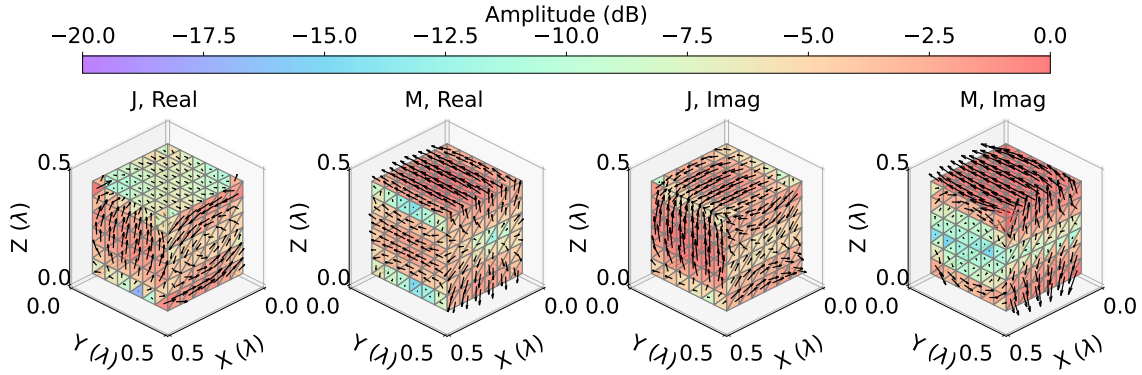

(a) CBF for singular value #1

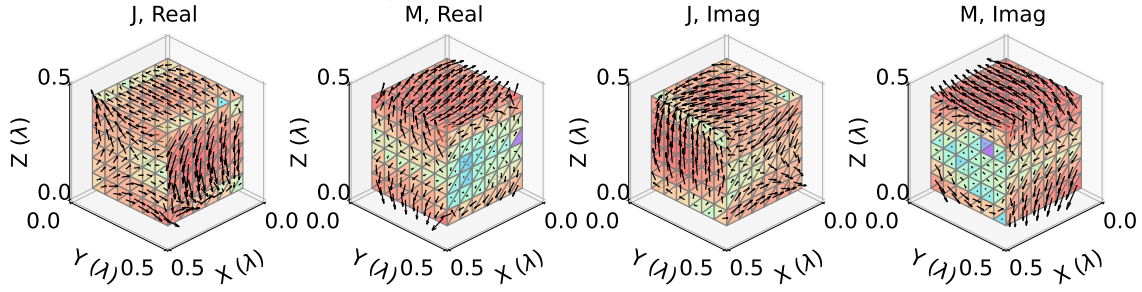

(b) CBF for singular value #2

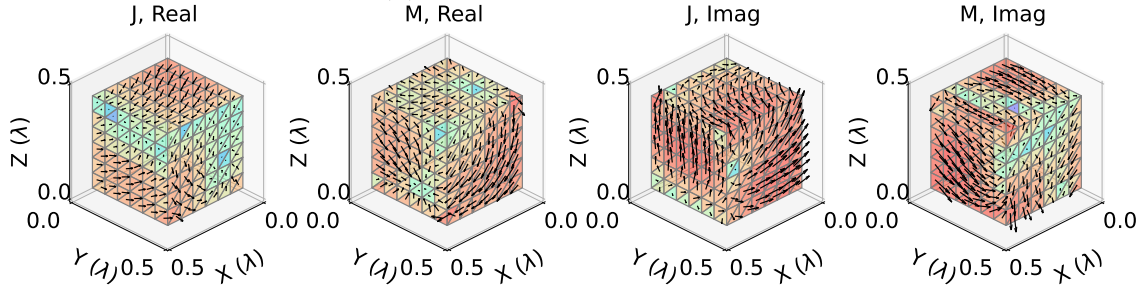

(c) CBF for singular value #96

Figure 3.18: CBF distributions for cell 1 of the cube array.

in Fig. 3.19 which shows the convergence of the outer GMRES when the incident field propagates in $-z$ direction. In this study, we use the conventional CBFM in addition to the MoM as a comparison to the proposed method. In the conventional CBFM, the CBFs are generated under condition 3.2-6, and $\tilde{\mathbf{U}}_1$s in (3.25) calculated for the electric and magnetic currents in each cell are used as $\mathbf{C}_m^{\mathrm{J}}$ and $\mathbf{C}_m^{\mathrm{M}}$. The impedance matrix in the conventional CBFM is set to $\mathcal{T}$-diagonal, and a diagonal preconditioner is applied. In Fig. 3.19, the residual norm of the MoM and the conventional CBFM did not reach 10^{-6} even after 1000 iterations. In the proposed CBFMs, on the other hand, this threshold is reached in less than 300 iterations. We see that the convergence of the proposed CBFM is further improved when l is

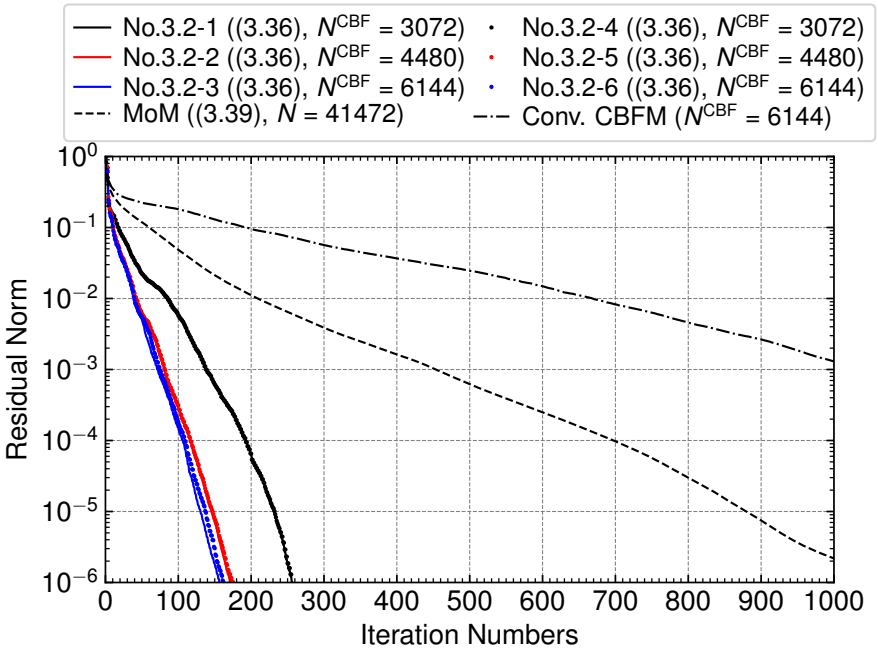

Figure 3.19: Convergence of the outer GMRES when the incident field propagates in $-z$ direction.

set to 5 or 6 (conditions 3.2-2, 3.2-3, 3.2-5 and 3.2-6), which is consistent with our consideration on the choice of CBFs based on the distribution of singular values in (3.29).

Fig. 3.20 shows the RCS patterns obtained with MoM, and the proposed method with conditions 3.2-2, 3.2-3, 3.2-5, and 3.2-6, where the criterion of the convergence is set as $\delta_{\mathrm{R}} < 10^{-4}$. The angle range, the angle resolution, and the polarization of the RCS pattern are the same as those for the sphere array analysis in Fig. 3.15. The numbers in the brackets in the legend in Fig. 3.20 represent the RMSE. We see that setting small values to angular intervals $\Delta\theta$ and $\Delta\phi$ slightly improves the accuracy of the analysis as mentioned in the previous discussion. All these results show that the proposed method enables one to obtain accurate solutions with a small number of iterations as one considers singular values belonging up to $l = 5$ or 6 groups.

The computational times for generating the primary CBFs and the final iteration for the condition 3.2-6, relative to the total time taken to compute RCS pattern for 91 directions ($0° \leq \theta \leq 90°$, $\Delta\theta = 1°$) with MoM, are less than 0.01 and 0.21, respectively. We thus see that the proposed method can compute the solution approximately five times faster than the conventional method in this example.

Finally, we show that the proposed method can accurately calculate currents even when the scatter has corners. We use the proposed method under the condition

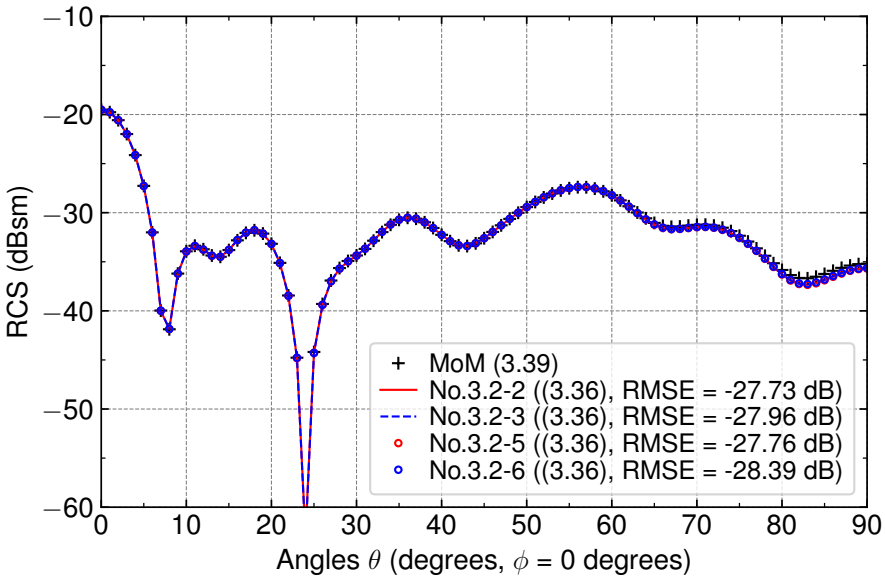

Figure 3.20: RCS of the cube array ($8 \times 2 \times 2$).

3.2-6 in TABLE 3.2 to compute the currents and compare the results with the reference solutions obtained with (3.20) [16] and RWG/BC bases constructed on the barycentric refinement of the original mesh [11]. Fig. 3.21 shows the electric currents on a cube having the side length of 0.5λ and $\epsilon_{\mathrm{r}} = 1$ ($N = 1296$) with the plane wave incident wave traveling along the z-axis. In this case the solution coincides with the incident wave and the electric current on the right side of the cube in Fig. 3.21 is exactly 0. In Fig. 3.21a, however, we see that the electric current calculated with the BC basis is not zero on the side around edges and corners due to the influence of the shape of the BC basis. This problem does not occur in the proposed method as shown in Fig. 3.21b because the CBFs are based on the correct electromagnetic current distribution. The number of iterations to reach the residual norm of $\delta_R = 10^{-6}$ is only 7 in the proposed method. These results show that the proposed method can accurately calculate the currents of a scatterer having corners with a small number of iterations.

3.5 Conclusion

We proposed a CBFM and a KCP which use the duality of electromagnetic currents. These techniques provide an efficient method to analyze scattering problems for homogeneous dielectric materials. The numerical results for various scatterers confirm the effectiveness of the proposed method. Furthermore, we investigated mathemat-

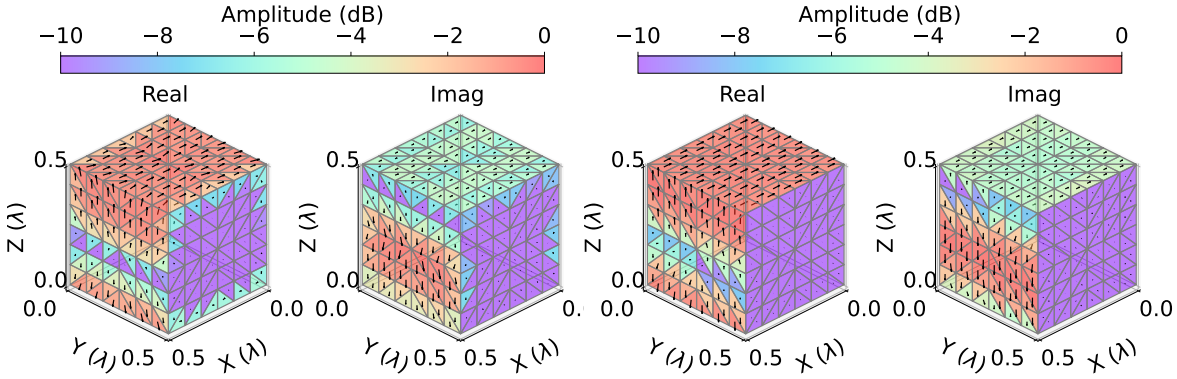

(a) BC Basis

(b) CBF

Figure 3.21: Electric current distributions on a cube of 0.5λ per side for $\epsilon_r = 1$.

ically the relationship between the distribution of singular values of a certain Gram matrix and the spacing of incident angles for plane waves for the generation of CBFs for disjoint scatterers.

Chapter 4

Conclusion

In this dissertation, we have documented two type of the CBFMs for the scattering analysis, one that produces the accurate results with a small number of unknowns, and the other that improves the convergence of iterative methods by using the Calderón preconditioner, respectively. We present below the conclusions of each method.

Chapter 2

We have proposed the CBFM with the use of IPCBF based on Krylov subspace algorithm to calculate angular characteristics of the scattering for electromagnetic incident waves from multiple directions rapidly and accurately. The results of this study can be divided into two main categories. The first is the clarification of the properties of IPCBF based on the Krylov subspace method through a parametric study. In particular, it was found that the accuracy of the analysis can be controlled by setting the residual norm and appropriate incidence interval during CBF generation. The second result is a hybrid method of the CBFM with the IPCBFs and the MoM. This method further improved the analysis accuracy of CBFM. These control of accuracy is very important from the viewpoint of practicality. The proposed methods enable it and also speeds up the analysis.

Chapter 3

We have proposed the CBFM for analyzing the scattering by dielectric objects based on the PMCHWT formulation. In this CBFM, we confirmed that the convergence can be greatly improved by using the RWG and BC basis, which take into account the orthogonality of the electromagnetic currents, and the KCP. The method can be applied to both continuous and discontinuous scatterers, but it has been shown to be particularly effective for discontinuous

scatterers.This means that it is effective for the analysis of devices such as metamaterials. In addition, the method does not require the scatterers to be periodically aligned. Therefore, it may be applicable to the design of the waveguides formed by vacating a part of the periodic structure, or to the scattering analysis of natural phenomena composed of non-periodic micro-dielectrics such as rain or hail.

Above the results indicate that we can rapidly solve the scattering problems with multiple incident waves by using the method shown in this dissertation. As indicated in the chapters, there are several ways to improve these methods to further speed up the analysis or make it more controllable. As a future plan, we plan to conduct the following studies.

Incident fields

We have focused on scattering problems with incident plane waves. We believe that the proposed method can be applied without difficulty to problems with other incident fields such as Hertzian dipoles, ring currents, or delta-gap excitations [6].

Various issues related to the formulation

We have analyzed scatterers with canonical geometry in order to understand the nature of the proposed method. Analysis of problems consisting of more complex geometry scatterers would provide a better understanding of the properties of the proposed method. In the chapter 3, we have restricted our attention to problems for dielectric scatterers. This may not be too restrictive in the optical band, where there exist many applications suitable for the proposed methods, e.g., finite and non-periodic non-metallic scatterers found in photonic crystal waveguides. In addition, one may use the proposed method to metallic scatterers since metals can be regarded as dielectrics with complex permittivity in the optical band, as seen in section 3.4.1. In the radio frequency band, however, it is necessary to further extend the formulation to cases of complex media that include perfect conductors and resonators in addition to simple dielectric scatterers. As regards issues in the low frequency range, our method is not exempt from low frequency breakdown and global loop problems. Existing solutions [53] may be used for such problems, but specific investigations remain issues for the future.

Further improvement of the computational efficiency

In this study, we have used standard algorithms for the CBF orthogonalization and FMM. For further acceleration, the combination of the proposed method with other algorithms such as the randomized SVD [54], the multilevel version

of the CBFM [39]– [41] and adaptive cross approximation [23,24] is worth considering in the future. Using stationary iterative solvers for linear equations in place of GMRES might also speedup the analysis.

Furthermore, since the main focus of this research was to investigate the characteristics of the proposed methods, no parallelization of central processing units or general-purpose computing on graphics processing units to accelerate the computation was performed. On the other hand, the proposed methods have parts that can be parallelized, such as CBF generation procedure and the SVD. These methods will enable further reduction of analysis time.

In the chapter 3, we remark that one may further accelerate the proposed method by modifying PMCHWT itself. For example, applying methods to make the PMCHWT suitable for KCP described in [55] appears to be worth the efforts.

Analysis for connected scatterers

When a single scatterer is divided into several cells, (3.24) for each cell corresponds to integral equations defined on a divided open surface, which is not a valid PMCHWT formulation, thus possibly leading to unsatisfactory results. For such cases, the use of IPCBF [36–38] is expected to improve the convergence because this approach is based on valid integral equations for the proposed method in chapter 3. See appendix A for a preliminary results of using IPCBFs with KCP.

Bibliography

[1] R. F. Harrington, *Field Computation by Moment Methods*. Piscataway, NJ: IEEE Press, 1993.

[2] J.-M. Jin, *The Finite Element Method in Electromagnetics*, 3rd ed. New York: Wiley-IEEE Press, 2014.

[3] A. Taflove and S. C. Hagness, *Computational Electrodynamics: The Finite-Difference Time-Domain Method*, 3rd ed. Boston: Artech House, 2005.

[4] Y. Saad, *Iterative Methods for Sparse Linear Systems*. PA, USA: SIAM, 2003.

[5] W. C. Chew, J. M. Jin, E. Michielssen, and J. Song, *Fast and Efficient Algorithms in Computational Electromagnetics*. Boston, USA: Altech House, 2001.

[6] O. Ergül and L. Gürel, *The Multilevel Fast Multipole Algorithm (MLFMA) for Solving Large-Scale Computational Electromagnetics Problems*. New York, USA: Wiley-IEEE Press, 2014.

[7] J. Song, C.-C. Lu, and W. C. Chew, "Multilevel fast multipole algorithm for electromagnetic scattering by large complex objects," *IEEE Trans. Antennas Propag.*, vol. 45, no. 10, pp. 1488–1493, Oct. 1997.

[8] L. Grasedyck and W. Hackbusch, "Construction and arithmetics of $\mathcal{H}$-matrices," *Computing*, vol. 70, pp. 295–334, Jul. 2003.

[9] A. Heldrig, J. M. Rius, J. M. Tamayo, J. Parrón, and E. Úbeda, "Fast direct solution of method of moments linear system," *IEEE Trans. Antennas Propag.*, vol. 55, no. 11, pp. 3220–3228, Nov. 2007.

[10] R. Gholami, J. Mojolagbe, A. Menshov, F. S. H. Lori, and V. Okhmatovski, "$\mathcal{H}$-matrix arithmetic for fast direct and iterative method of moment solution of surface-volume-surface EFIE for 3-D radiation problems," *Progress In Electromagnetics Research B*, vol. 82, pp. 189–210, Dec. 2018.

[11] F. P. Andriulli, K. Cools, H. Bağci, F. Olyslager, A. Buffa, S. Christiansen, and E. Michielssen, "A multiplicative Calderon preconditioner for the electric field integral equation," *IEEE Trans. Antennas Propag.*, vol. 56, no. 8, pp. 2398–2412, Aug. 2008.

[12] S. Rao, D. Wilton, and A. Glisson, "Electromagnetics scattering by surfaces of arbitrary shape," *IEEE Trans. Antennas Propag.*, vol. 30, no. 3, pp. 409–418, May 1982.

[13] A. Buffa and S. H. Christiansen, "A dual finite element complex on the barycentric refinement," *Mathematics of Computation*, vol. 76, no. 260, pp. 1743–1769, Oct. 2007.

[14] S. Yan, J. M. Jin, and Z. Nie, "A comparative study of Calderón preconditioners for PMCHWT equations," *IEEE Trans. Antennas Propag.*, vol. 58, no. 7, pp. 2375–2383, Oct. 2010.

[15] K. Cools, F. P. Andriulli, and E. Michielssen, "A Calderón multiplicative preconditioner for the PMCHWT integral equation," *IEEE Trans. Antennas Propag.*, vol. 59, no. 12, pp. 4579–4587, Dec. 2011.

[16] K. Niino and N. Nishimura, "Calderón preconditioning approaches for PMCHWT formulations for Maxwell's equations," *International Journal of Numerical Modelling: Electronic Networks, Devices and Fields*, vol. 25, no. 5–6, pp. 558–572, Mar. 2012.

[17] K. Niino and N. Nishimura, "Preconditioning based on Calderon's formulae for periodic fast multipole methods for Helmholtz' equation," *J. Comp. Phys.*, vol. 231, no. 1, pp. 66–81, Jan. 2012.

[18] P. Yla-Oijala, S. P. Kiminki, K. Cools, F. P. Andriulli, and S. Jarvenpaa, "Stable discretization of combined source integral equation for scattering by dielectric objects," *IEEE Trans. Antennas Propag.*, vol. 60, no. 5, pp. 2575–2578, May 2012.

[19] L. Matekovits, V. A. Laza, and G. Vecchi, "Analysis of large complex structures with the synthetic-functions approach," *IEEE Trans. Antennas Propag.*, vol. 55, no. 9, pp. 2509–2521, Sep. 2007.

[20] V. V. S. Prakash and R. Mittra, "Characteristic basis function method: a new technique for efficient solution of method of moments matrix equations," *Microw. Opt. Techn. Let.*, vol. 36, no. 2, pp. 95–100, Jan. 2003.

[21] E. Lucente, A. Monorchio, and R. Mittra, "An iteration-free MoM approach based on excitation independent characteristic basis functions for solving large multiscale electromagnetic scattering problems," *IEEE Trans. Antennas Propag.*, vol. 56, no. 4, pp. 999–1007, Apr. 2008.

[22] R. Mittra and K. Du, "Characteristic basis function method for iteration-free solution of large method of moments problems," *Progress In Electromagnetics Research B*, vol. 6, pp. 307–336, May 2008.

[23] R. Maaskant, R. Mittra, and A. G.Tijhuis, "Fast analysis of large antennas arrays using the characteristic basis function method and the adaptive cross approximation algorithm," *IEEE Trans. Antennas Propag.*, vol. 56, no. 11, pp. 3440–3451, Nov. 2008.

[24] X. Chen, C. Gu, J. Ding, Z. Li, and Z. Niu, "Multilevel fast adaptive cross-approximation algorithm with characteristic basis functions," *IEEE Trans. Antennas Propag.*, vol. 63, no. 9, pp. 3994–4002, Sep. 2015.

[25] K. Konno, Q. Chen, K. Sawaya, and T. Sezai, "Optimization of block size for CBFM in MoM," *IEEE Trans. Antennas Propag.*, vol. 60, no. 10, pp. 4719–4724, Oct. 2012.

[26] C.-S. Park, Y.-R. Jeong, I.-P. Hong, and J.-G. Yook, "Block size optimization of CBFM for scattering problems," *IEEE Trans. Antennas Propag.*, vol. 66, no. 10, pp. 5370–5377, Oct. 2018.

[27] G. H. Golub and C. F. V. Loan, *Matrix Computations*, 4th ed. Baltimore, MD: Johns Hopkins University Press, 2013.

[28] J. Yeo, V. V. S. Prakash, and R. Mittra, "Efficient analysis of a class of microstrip antennas using the characteristic basis function method (CBFM)," *Microw. Opt. Techn. Let.*, vol. 39, no. 6, pp. 456–464, Dec. 2003.

[29] G. B. Bianconi, C. Pelletti, R. Mittra, K. Du, and A. Monorchio, "An efficient technique for the evaluation of the reduced matrix in the context of the CBFM for layered media," *IEEE Antennas Wireless Propag. Lett.*, vol. 10, pp. 674–677, Jun. 2011.

[30] S. G. Hay, J. D. O'Sullivan, and R. Mittra, "Connected patch array analysis using the characteristic basis function method," *IEEE Trans. Antennas Propag.*, vol. 59, no. 6, pp. 1828–1837, Jun. 2011.

[31] K. Konno, Q. Chen, and R. J. Burkholder, "Numerical analysis of large-scale finite periodic arrays using a macro block-characteristic basis function method," *IEEE Trans. Antennas Propag.*, vol. 65, no. 10, pp. 5348–5355, Oct. 2017.

[32] T. Marinović, R. Maaskant, R. Mittra, and G. A. E. Vandenbosch, "Comparison of CBFM-enhanced iterative methods for MoM-based finite antenna array analysis," *IEEE Trans. Antennas Propag.*, vol. 70, no. 5, pp. 3538–3548, May 2022.

[33] J. Laviada, M. R. Pino, and F. Las-Heras, "Generation of excitation-independent characteristic basis functions for three-dimensional homogeneous dielectric bodies," *IEEE Trans. Antennas Propag.*, vol. 59, no. 9, pp. 3318–3327, Sep. 2011.

[34] I. Fenni, H. Roussel, M. Darces, and R. Mittra, "Fast analysis of large 3-D dielectric scattering problems arising in remote sensing of forest areas using the CBFM," *IEEE Trans. Antennas Propag.*, vol. 62, no. 8, pp. 4282–4291, Aug. 2014.

[35] F. Huang and Y. Sun, "Efficient solution of electromagnetic scattering from dielectric objects via characteristic basis function method based on large-size blocks with multilevel subdivision," *IEEE Access*, vol. 7, pp. 71 741–71 748, Jun. 2019.

[36] T. Tanaka, Y. Inasawa, Y. Nishioka, and H. Miyashita, "Improved primary characteristic basis function method for monostatic radar cross section of specific coordinate plane," *IEICE Trans. Electron.*, vol. E99-C, no. 1, pp. 28–35, Jan. 2016.

[37] T. Tanaka, Y. Inasawa, Y. Nishioka, and H. Miyashita, "Improved primary characteristic basis function method considering higher-order multiple scattering," *IEICE Trans. Electron.*, vol. E100-C, no. 1, pp. 45–51, Jan. 2017.

[38] T. Tanaka, K. Niino, N. Nishimura, M. Takikawa, and N. Yoneda, "A generation scheme of the characteristic basis functions by using block Krylov subspace algorithm (Japanese)," *Trans. Jpn. Soc. Comput. Methods Eng.*, vol. 19, pp. 99–102, Dec. 2019.

[39] R. Maaskant, R. Mittra, and A. Tijhuis, "Multilevel characteristic basis function method (MLCBFM) for the analysis of large antenna arrays," *URSI Radio Science Bulletin*, vol. 2011, no. 336, pp. 23–34, Mar. 2011.

[40] C.-S. Park, I.-P. Hong, Y.-J. Kim, and J.-G. Yook, "Acceleration of multilevel characteristic basis function method by multilevel multipole approach," *IEEE Trans. Antennas Propag.*, vol. 68, no. 10, pp. 7109–7120, Oct. 2020.

[41] C. Delgado, M. F. Catedra, and R. Mittra, "Efficient multilevel approach for the generation of characteristic basis functions for large scatters," *IEEE Trans. Antennas Propag.*, vol. 56, no. 7, pp. 2134–2137, Jul. 2008.

[42] E. Garcia, C. Delgado, I. G. Diego, and M. F. Catedra, "An iterative solution for electrically large problems combining the characteristic basis function method and the multilevel fast multipole algorithm," *IEEE Trans. Antennas Propag.*, vol. 56, no. 8, pp. 2363–2371, Aug. 2008.

[43] X. Chen, C. Gu, Z. Li, and Z. Niu, "Efficient iterative solution of electromagnetic scattering using adaptive cross approximation enhanced characteristic basis function method," *IET Microw. Antennas Propag.*, vol. 9, no. 3, pp. 217–223, Feb. 2015.

[44] T. Tanaka, K. Niino, N. Nishimura, and M. Takikawa, "Accuracy controllable characteristic basis function method by using Krylov subspace algorithm," *Trans. Jpn. Soc. Comput. Methods Eng.*, vol. 22, pp. 11–19, Dec. 2022.

[45] T. Tanaka, K. Niino, and N. Nishimura, "Characteristic basis function method combined with calderón preconditioner for PMCHWT formulation," *arXiv:2111.11058*, Nov. 2021.

[46] E. F. Knott, J. F. Shaeffer, and M. T. Tuley, *Radar Cross Section*, 2nd ed. Boston, USA: Artech House, 1993.

[47] R. F. Harrington, *Time-Harmonic Electromagnetic Fields*. New York, USA: Wiley-IEEE Press, 2001.

[48] J. Nédélec, *Acoustic and Electromagnetic Equations: Integral Representations for Harmonic Problems*. New York: Springer-Verlag, 2001.

[49] A. E. Guennouni, K. Jbilou, and H. Sadok, "A block version of BiCGSTAB for linear systems with multiple right-hand sides," *Elec. Trans. Numer. Anal.*, vol. 16, pp. 129–142, Jan. 2003.

[50] Y. Nakamura, K.-I. Ishikawa, Y. Kuramashi, T. Sakurai, and H. Tadano, "Modified block BiCGSTAB for lattice QCD," *Comput. Phys. Commun.*, vol. 183, pp. 34–37, Jan. 2012.

[51] A. C. Woo, H. T. G. Wang, M. J. Schuh, and M. L. Sanders, "EM programmer's notebook-benchmark radar targets for the validation of computational electromagnetics programs," *IEEE Trans. Antennas Propag.*, vol. 35, no. 1, pp. 84–89, Feb. 1993.

[52] P. B. Johnson and R. W. Christy, "Optical constants of the noble metals," *Physical Review B*, vol. 6, no. 12, pp. 4370–4379, Dec. 1972.

[53] Y. Beghein, R. Mitharwal, K. Cools, and F. P. Andriulli, "On a low-frequency and refinement stable PMCHWT integral equation leveraging the quasi-Helmholtz projectors," *IEEE Trans. Antennas Propag.*, vol. 65, no. 10, pp. 5365–5375, Oct. 2017.

[54] C. Li and R. Mittra, "Solution of electrically large scattering problems using the characteristic basis function method." Okinawa, Japan: 2016 International Symposium on Antennas and Propagation (ISAP), 2016, pp. 562–563.

[55] A. Kleanthous, T. Betcke, D. P. Hewett, P. Escapil-Inchauspé, C. Jerez-Hanckes, and A. J. Baran, "Accelerated calderón preconditioning for maxwell transmission problems," *IEEE Trans. Antennas Propag.*, Aug. 2020, [Online]. Available: https://arxiv.org/abs/2008.04772v1.

[56] K. Sewraj and M. M. Botha, "Generalized characteristic basis function definitions for efficient antenna array analysis in 2D." Verona, Italy: 2017 Int. Conf. Electromagn. Adv. Appl. (ICEAA), 2017, pp. 984–987.

Appendix A

CBFM with the use of KCP for connected scatterers

In the main body of the chapter 3, we have tested the CBFM with the use of KCP in problems for disconnected scatterers, each of whose components can be covered by a single cell. Application of the proposed method to connected scatterer is harder mainly because the standard primary CBF does not lead to valid integral equations with the PMCHWT formulation when one divides a connected scatterer into cells. This appendix briefly discusses our attempt to use IPCBFs in the proposed method in order to resolve difficulties associated with connected scatterers. Note that this approach does not suffer from problems associated with invalid integral equations because of the use of (3.11).

We analyze the cylinder shown in Fig. A.1 by using IPCBFs. The angle range and polarization to calculate the RCS pattern are $0^\circ \leq \theta \leq 45^\circ$, $\Delta\theta = 0.5^\circ$, $\phi = 0^\circ$ and $\hat{\theta}$ (91 directions). The mesh size of the scatterer is determined to be about 0.1λ. The number of unknowns in MoM is 52752. TABLE A.1 shows the conditions for the IPCBF generation. The propagation directions of the plane waves used for the IPCBF generation are taken on the coordinate plane ($\phi = 0^\circ$ plane) where the RCS is calculated. Therefore, the number of plane wave directions for IPCBF generation s is equal to $N_\theta (= 10)$ in all the conditions. We point out that this restricted choice of samples is possible with IPCBFs while the same choice does not lead to satisfactory results with primary CBFs, as noted in [36]. To perform the preconditioning in (3.36), we compute $\left(\mathbf{G}^{\mathrm{CBF}}\right)^{-1} \mathbf{y}^{\mathrm{CBF}}$ using the diagonally preconditioned GMRES with the empirically determined error tolerance of 1.0×10^{-5}. We have also carried out the same analysis using the primary CBFs generated using parameters in TABLE A.2, which are comparable to those in TABLE 3.1 and TABLE 3.2.

Fig. A.2 shows the convergence property of the outer GMRES when the $\hat{\theta}$ polarized incident field propagates in $-z$ direction. The CBFM with IPCBFs converges

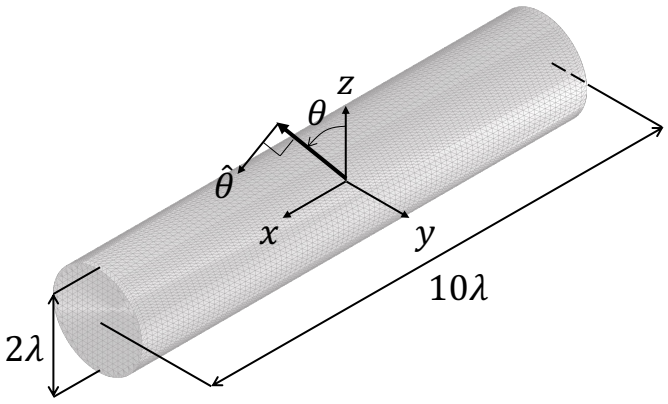

Figure A.1: Cylinder

Table A.1: Parameters for calculating IPCBFs

No.	δ_{r}	θ_{s}	$\Delta\theta$	N_θ	Pol.	Cell (λ)	δ_{SVD}
A.1-1	1.0×10^{-3}	0°	5°	10	$\hat{\theta}$	5/4	1.0×10^{-3}
A.1-2	1.0×10^{-2}	0°	5°	10	$\hat{\theta}$	5/4	1.0×10^{-3}
A.1-3	1.0×10^{-1}	0°	5°	10	$\hat{\theta}$	5/4	1.0×10^{-3}
A.1-4	1.0×10^{-3}	0°	5°	10	$\hat{\theta}$	5/4	1.0×10^{-7}

Table A.2: Parameters for calculating primary CBFs

θ_{s}	$\Delta\theta$	N_θ	ϕ_{s}	$\Delta\phi$	N_ϕ	Pol.	Cell (λ)	δ_{SVD}
0°	10°	36	0°	10°	18	$\hat{\theta}, \hat{\phi}$	5/4	1.0×10^{-3}

much faster than MoM. The CBFM with the primary CBFs shows even poorer convergence compared to that of the MoM. This is thought to be due to the effect of the fictitious open edges that occur when the scatterer is divided in the CBF generation process. It is noted that the average numbers of the inner iterations are only 8.3 with the IPCBF and 12.7 with primary CBFs per outer-iteration, respectively.

Fig. A.3 and Fig. A.4 show the RCS pattern, RMSE, number of CBFs N^{CBF}, and average number of final iterations N^{ITR} of the CBFM which uses IPCBFs. The number N^{ITR} gives the mean value of the numbers of iterations in the analyses for 91 incident directions. The number N^{CBF} does not change significantly with conditions and the average numbers N^{ITR} for conditions A.1-1 and A.1-2 are almost the same. The RCS obtained with the first condition agrees well with the MoM results down to low levels and RMSE is -26.49dB.

TABLE A.3 shows the relative computational time ratio, where "CBF Gen.", "Iter." and "Total" represent the relative computational time for CBF generation,

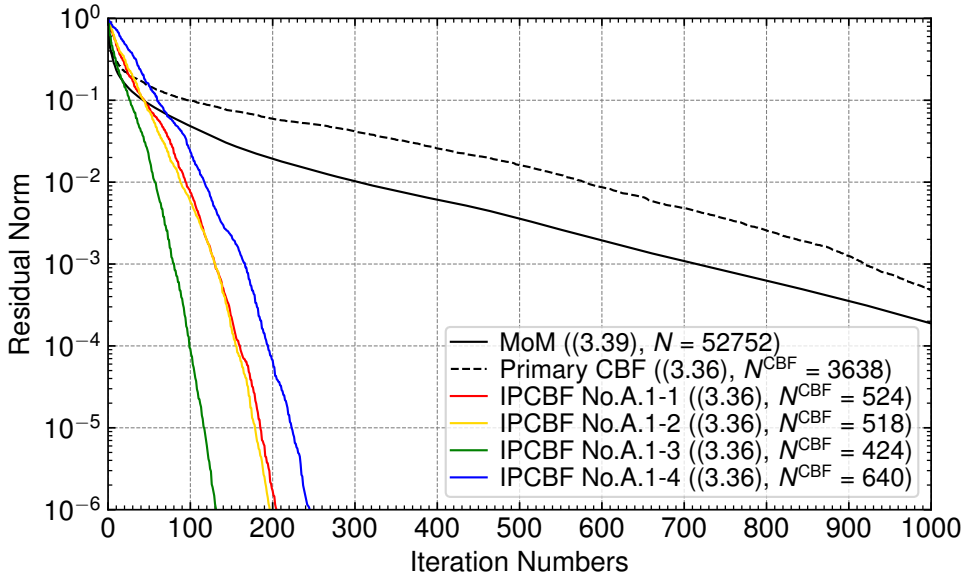

Figure A.2: Convergence of the outer GMRES for the $\hat{\theta}$ polarized incident field from $-z$ direction.

Table A.3: Relative computational time ratio

No.	CBF Gen.	Iter.	Total
1	0.06	0.12	0.18
2	0.02	0.12	0.14
3	< 0.01	0.08	< 0.09
4	0.06	0.16	0.22

iteration for RCS analysis, and their total relative to the total computational time to analyze cases for 91 incident directions with the MoM, respectively. For reference, the actual total computational time for the MoM is approximately 73.3 hours. In the first and second conditions, the solutions are obtained more than five times faster than in the conventional MoM. To obtain a accurate solution, the value of the residual norm δ_{r} should be around 1.0×10^{-3}, while this value should be around 1.0×10^{-2} for a rough and fast study of the overall trend. In the fourth condition, the threshold of singular value decomposition δ_{SVD} (see 3.3.2) is reduced while other parameters are kept the same as in the first condition. We see that the accuracy further improves so that the RMSE becomes -31.35dB. This result tells that we can further control the accuracy of the analysis by reducing δ_{SVD} when the the residual norm δ_{r} is less than 1.0×10^{-3}.

We note, however, that the parameters in TABLE A.1 are given just as examples.

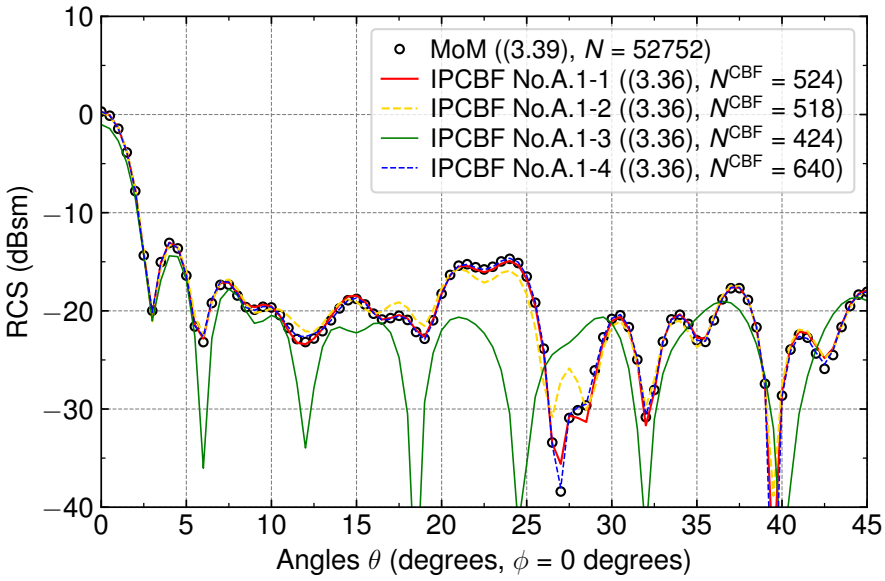

Figure A.3: RCS pattens

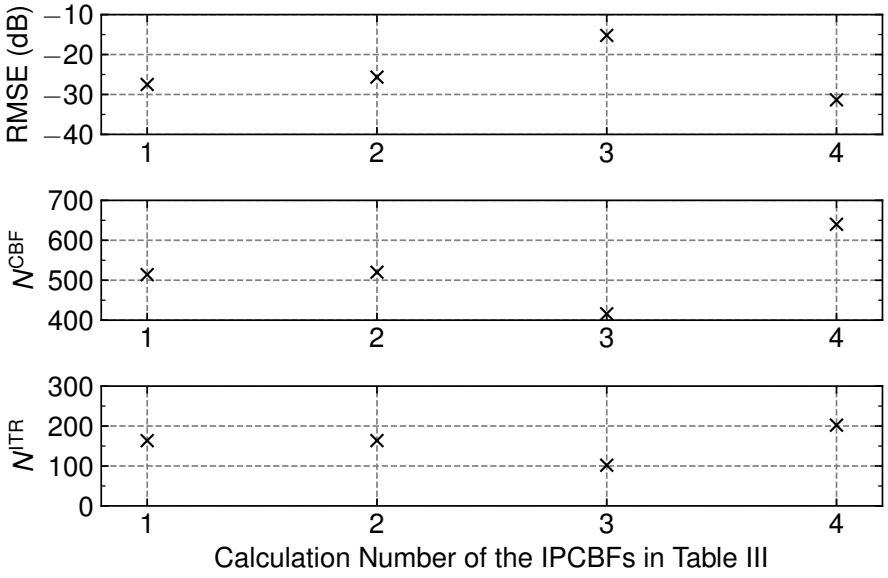

Figure A.4: RMSE, N^{CBF}, and N^{ITR}

Further parametric studies are needed to optimize these values. We also note that combining IPCBFs with methods that use locality, such as those in [56], may also speed up the analysis for large scatterers since IPCBFs consider only the global behaviors of currents.